Ph.D. thesis

Domonkos Attila Tasi

Ab initio characterization and dynamics of S_N2 reactions involving polyatomic nucleophiles

Supervisor:

Dr. Gábor Czakó

associate professor

Doctor of the Hungarian Academy of Sciences

University of Szeged
Faculty of Science and Informatics
Department of Physical Chemistry and Materials Science
Doctoral School of Chemistry

MTA-SZTE Lendület Computational Reaction Dynamics Research Group

Szeged
2023

Publications covered in the thesis

[1] **D. A. Tasi***, T. Michaelsen, R. Wester, G. Czakó*: *Quasi-classical trajectory study of the OH^- + CH_3I reaction: Theory meets experiment*. Phys. Chem. Chem. Phys., 25, 4005 (2023)

[2] **D. A. Tasi***, G. Czakó*: *Unconventional S_N2 retention pathways induced by complex formation: High-level dynamics investigation of the NH_2^- + CH_3I polyatomic reaction*. J. Chem. Phys., 156, 184306 (2022)

[3] Z. Kerekes, **D. A. Tasi**, G. Czakó*: *S_N2 reactions with an ambident nucleophile: A benchmark ab initio study of the CN^- + CH_3Y [Y = F, Cl, Br, I] systems*. J. Phys. Chem. A, 126, 889 (2022)

[4] **D. A. Tasi***, G. Czakó*: *Uncovering an oxide ion substitution for the OH^- + CH_3F reaction*. Chem. Sci., 12, 14369 (2021)

[5] **D. A. Tasi***, C. Tokaji, G. Czakó*: *A benchmark ab initio study of the complex potential energy surfaces of the OH^- + CH_3CH_2Y [Y = F, Cl, Br, I] reactions*. Phys. Chem. Chem. Phys., 23, 13526 (2021)

[6] G. Czakó***,** T. Győri, D. Papp, V. Tajti, **D. A. Tasi**: *First-principles reaction dynamics beyond six-atom systems*. J. Phys. Chem. A, 125, 2385 (2021)

[7] **D. A. Tasi,** T. Győri, G. Czakó*: *On the development of a gold-standard potential energy surface for the OH^- + CH_3I reaction*. Phys. Chem. Chem. Phys., 22, 3775 (2020)

[8] **D. A. Tasi**, Z. Fábián, G. Czakó*: *Rethinking the X^- + CH_3Y [X = OH, SH, CN, NH_2, PH_2; Y = F, Cl, Br, I] S_N2 reactions*. Phys. Chem. Chem. Phys., 21, 7921 (2019)

[9] **D. A. Tasi**, Z. Fábián, G. Czakó*: *Benchmark ab initio characterization of the inversion and retention pathways of the OH^- + CH_3Y [Y = F, Cl, Br, I] S_N2 reactions*. J. Phys. Chem. A, 122, 5773 (2018)

Publications related to the thesis

[10] G. Czakó***,** T. Győri, B. Olasz, D. Papp, I. Szabó, V. Tajti, **D. A. Tasi**: *Benchmark ab initio and dynamical characterization of the stationary points of reactive atom + alkane and S_N2 potential energy surfaces*. Phys. Chem. Chem. Phys., 22, 4298 (2020)

*** Corresponding author(s)**

In the dissertation, square brackets [1–10] are used to denote self-citations, while references closely related to the topic are marked with an upper index.

Contents

Glossary

ATcT	Active Thermochemical Tables
aug-cc-pV*n*Z	augmented correlation-consistent polarized-valence-*n*-ζ
b	impact parameter
BCCD	Brueckner coupled cluster doubles
BCCD(T)	Brueckner coupled cluster doubles with perturbative triples
CCSD(T)	coupled cluster singles, doubles, and perturbative triples
CCSD(T)-F12b	explicitly-correlated CCSD(T)
DF-MP2-F12	explicitly-correlated density-fitted MP2
DFT	density functional theory
E2	bimolecular elimination
E_{coll}	collision energy
ECP	effective core potential
GTO	Gauss-type orbitals
HF	Hartree–Fock
ICS	integral cross section
MP2	second-order Møller–Plesset perturbation theory
PES	potential energy surface
PIP	permutationally invariant polynomial
QCT	quasi-classical trajectory
S_N1	unimolecular nucleophilic substitution
S_N2	bimolecular nucleophilic substitution
STO	Slater-type orbitals
ZPE	zero-point energy

1 Introduction

The comprehensive characterization of chemical reactions and processes using experimental and theoretical methods is a fundamental objective in chemistry. Nucleophilic substitution (S_N) is a fundamental reaction, which plays an important role in organic chemistry. The S_N reactions have been described by Ingold and co-workers in the 1930s, classifying two distinct mechanisms: unimolecular and bimolecular nucleophilic substitution (S_N1 and S_N2).[1] While S_N1 occurs in two separate steps with a rate determining process of a unimolecular dissociation, S_N2 is a concerted, second-order reaction.

Chemical reactions can be studied both in solution phase and gas phase, but in order to eliminate the diffusion and solvation effects caused by the solvent medium, and to gain insight into the specific reaction mechanism, investigating reactions in the gas phase is essential. However, it should be noted that the acquired "gas-phase experiences" cannot be applied in solution phase directly, especially in case of ion–molecule reactions (such as S_N), wherein the ion-dipole interactions are stronger in gas phase.

A schematic S_N2 reaction is:

$$X^- + CH_3Y \rightarrow CH_3X + Y^-, \qquad \text{R.(1)}$$

where X^- and CH_3Y denote nucleophile and substrate, respectively. In gas phase, the traditional back-side attack Walden-inversion mechanism shows a double-well potential energy profile: In the entrance and product channels two ion-dipole minima can be found [$X^-\cdots CH_3Y$ (PreMIN) and $XCH_3\cdots Y^-$ (PostMIN), in order] in connection with a [$X\cdots CH_3\cdots Y]^-$ transition state, where the umbrella motion of the CH_3 group inverts the configuration of the CH_3Y reactant as shown in Figure 1.1.[2] If the nucleophile contains at least one hydrogen, then in some cases a $CH_3X(H)\cdots Y^-$ hydrogen-bonded minimum (PostHMIN) can be found in the exit channel instead of the traditional $XCH_3\cdots Y^-$. On the contrary, front-side attack mechanism comprises a high-energy $[XYCH_3]^-$ transition state and considering the CH_3Y configuration, a retention takes place. To determine the configuration of the CH_3X product, the Cahn-Ingold-Prelog priority conventions[3] can be applied. Note that, basically the carbon atom of the methyl halide is not a stereogenic centre, although in a simulation the hydrogen atoms can be distinguished from each other by labelling them. Competing with S_N2, proton abstraction is an alternative, thermodynamically less preferred pathway leading to the $HX + CH_2Y^-$ products.

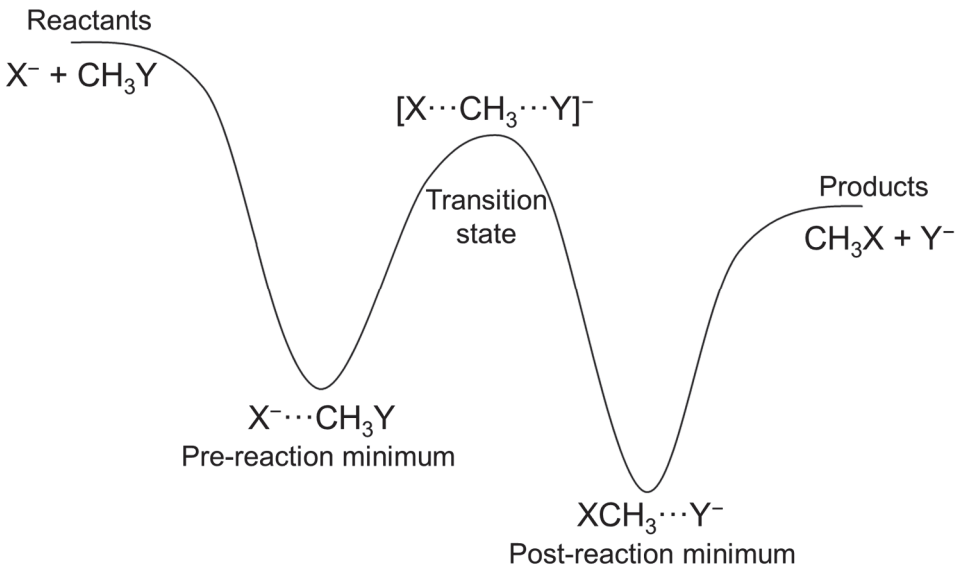

Figure 1.1 A schematic potential energy surface of a representative exothermic barrierless Walden-inversion pathway in case of a gas-phase $X^- + CH_3Y \rightarrow CH_3X + Y^-$ S_N2 reaction.

The investigations of S_N2 reactions occurring between halide ions and methyl halides [X, Y = F, Cl, Br, I] have been a hot topic since the 1950s, however these studies were only limited to the above-mentioned classical picture of the S_N2 reactions in the 20th century.[4–8] In the late 2000s and the early 2010s, a breakthrough took place revealing that the classical description of the elemental S_N2 reactions is much more complex, and a "rethinking" of the mechanisms is inevitable.[9–12] In 2016, Xie *et al.* summarized the possible direct and indirect mechanisms of the S_N2 reactions.[12] Figure 1.2 illustrates the case of the OH^- and methyl halide reaction, and it is apparent that the direct rebound and stripping, and the indirect ion-dipole complex formation, roundabout, hydrogen-bond complex formation and front-side complex formation mechanisms are different forms of the Walden-inversion pathway resulting an inverted CH_3X product. Besides the direct front-side attack, retention can also proceed through an indirect lower-energy route. This so-called double-inversion mechanism, uncovered by Szabó and Czakó,[13] starts with a proton-abstraction induced inversion *via* a $[XH\cdots CH_2Y]^-$ transition state following by a Walden inversion. Although, relying on the dynamical study on the $F^- + CH_3I$ reaction by Ma *et al.*,[14] that double-inversion mechanism through the $[XH\cdots CH_2Y]^-$ transition state appears to be a non-intrinsic reaction coordinate pathway.

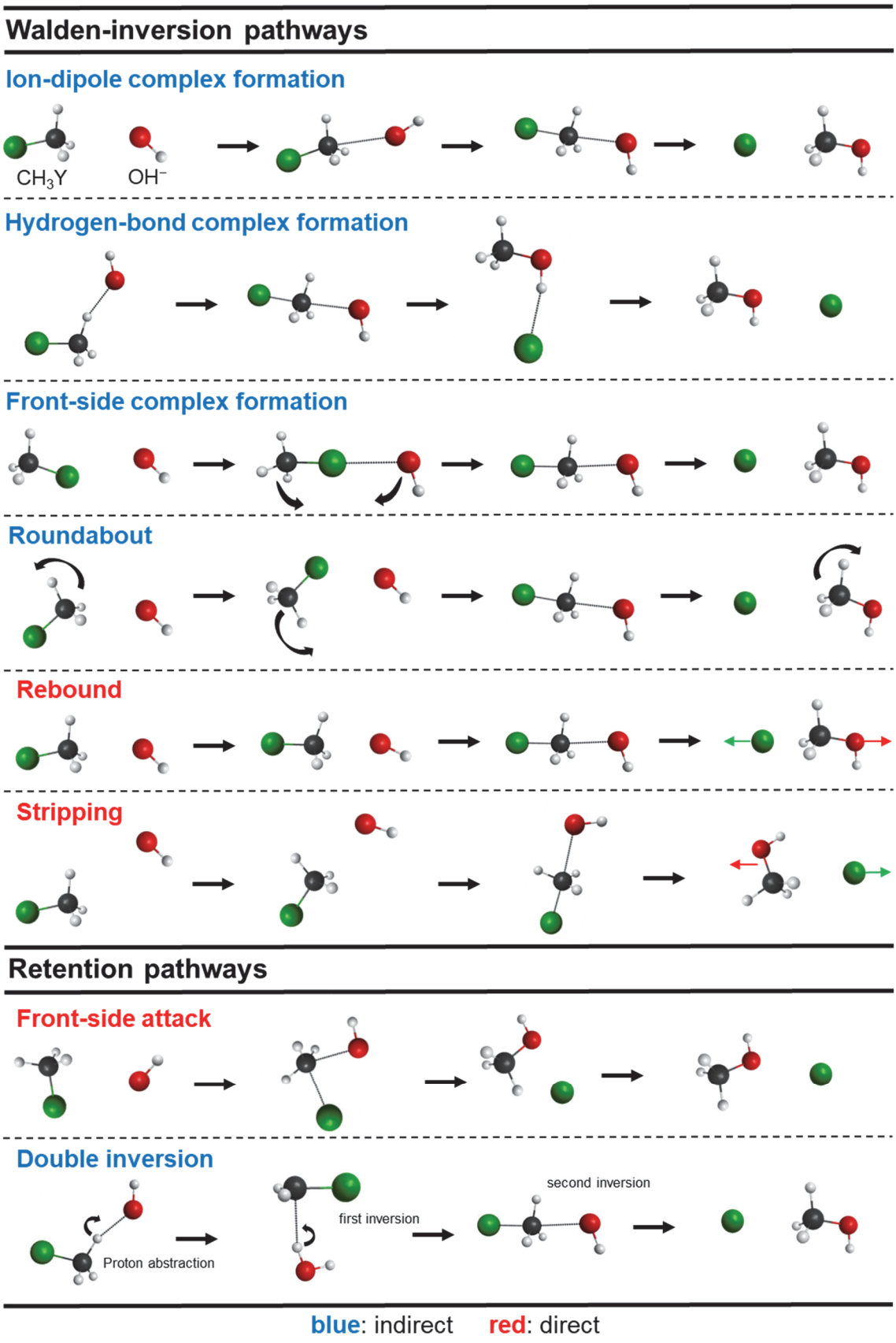

Figure 1.2 The possible mechanisms of the gas-phase $OH^- + CH_3Y \rightarrow CH_3OH + Y^-$ S_N2 reaction.[12]

To enhance our understanding of the S_N2 reactions, more intricate systems should be explored. Basically, there are two options to surpass the standard six-atomic S_N2 reactions: Substitute the halide ions with di- or polyatomic nucleophiles (such as: OH^-, SH^-, CN^-, NH_2^-, PH_2^-, *etc.*), or exchange methyl halides with different alkyl halides (such as: ethyl, propyl and butyl halides). For the $OH^- + CH_3Cl$ S_N2 reaction, an extensive study was carried out by Evanseck *et al*. utilizing second and third-order Møller–Plesset perturbation theory (MP2 and MP3),[15] and later direct *ab initio* molecular dynamics calculations were performed by Igarashi and co-workers.[16,17] In the early 2000s, Schaefer and co-workers carried out a stationary point characterization of the Walden-inversion pathway of the $F^- + CH_3Y$ [Y = F, Cl, OH, SH, CN, PH_2, NH_2] S_N2 reactions using the CCSD(T) method with the TZ2Pf+dif and aug-cc-pVTZ basis sets.[18] Subsequently, the energetics of the stationary points of the latter reactions were computed applying the focal-point analysis approach considering core and scalar relativistic corrections.[19] Moreover, some papers investigated the reactivity of several α-nucleophiles (nucleophiles with an adjacent lone pair, such as Cl^-, Br^-, OH^-, SH^-, CH_3O^-, HOO^-, NH_2O^-, BrO^-, ClO^-, *etc.*) with RF/RCl (R = CH_3, CH_3CH_2, $CH(CH_3)_2$, *etc.*) in gas phase and solution, as well.[20–23]

In the early of the 20th century, direct dynamics simulations of the $OH^- + CH_3F$ reaction fulfilled by Sun *et al.* revealed that the deep $CH_3OH\cdots F^-$ minimum of the exit channel is circumvented by ~90% of the trajectories as the F^- leaves preferably along the $O–C\cdots F^-$ axis.[24] Analogous outcomes were reported regarding the significance of the deep well of the latter reaction by Taketsugu *et al*.[25,26] and Carpenter and co-workers.[27] Furthermore, studies showed that the $HOCH_3\cdots F^-$ post-reaction ion−dipole complex does not exist on this latter path for this reaction.[28] In 2022, the reaction of $OH^- + CH_3Cl$ were investigated by Zhang and co-workers[29] with direct dynamics simulations at the level of B3LYP/aug-cc-pVDZ including a comparison of the $X^- + CH_3Y$ [X = F, OH, Y = Cl, I] systems. It is noteworthy that besides gas phase, the Walden-inversion mechanisms of the $OH^- + CH_3Y$ [Y = F, Cl, Br] and the $SH^-/PH_2^- + CH_3Y$ [Y = F, Cl, Br, I] S_N2 reactions were also studied in aqueous solution by the Wang group.[30–33] Experimental and theoretical studies have extensively examined the seven-atomic S_N2 reaction between OH^- and CH_3I.[34–36] Non-traditional H-bonded stationary points ($CH_2IH\cdots OH^-$ and $CH_3OH\cdots I^-$ minima and a $[CH_2IH\cdots OH]^-$ transition state) for the Walden-inversion pathway, and a front-side complex ($CH_3Y\cdots OH^-$) were characterized by the Hase group using density functional theory (DFT) calculations.[37–39] The exothermic

$OH^- + CH_3I \rightarrow CH_2I^- + H_2O$ proton-abstraction route was also studied revealing seven stationary points.[38] Direct dynamics simulations were carried out for the $OH^- + CH_3I$ reaction, as well, which opened the door for comparison with the experimental results performed by the groups of Wester and Viggiano employing crossed-beam imaging and selected ion flow tube techniques, respectively.[37,38,40,41] The dynamics simulations were run at 0.05, 0.5, 1.0 and 2.0 eV collision energies (E_{coll}), and five different product channels were identified: S_N2 ($CH_3OH + I^-$), proton abstraction ($CH_2I^- + H_2O$), proton abstraction with dissociation ($CH_2 + I^- + H_2O$), iodine abstraction ($IOH^- + CH_3$) and $[I\cdots CH_3\cdots OH]^-$ intermediate. Note that the trajectories were propagated until a 3 ps of lifetime, otherwise these latter $[I\cdots CH_3\cdots OH]^-$ intermediates would have dissociated to $CH_3OH + I^-$ or $CH_2I^- + H_2O$. At higher E_{coll}, for both S_N2 and proton abstraction, a direct character (rebound and stripping mechanisms) was determined, although, at $E_{coll} = 0.05$ eV, indirect pathways (hydrogen-bond complex and roundabout mechanisms) turned out to be more dominant, especially for proton abstraction. The product relative translation energy and the velocity scattering angle distributions were in good agreement with the experiment data, nonetheless, the simulations predicted a dominance of forward scattering for S_N2, while the experiment showed an isotropic nature. The influence of the water molecules on the dynamics were examined, as well, unveiling various reaction mechanisms for different degrees of solvation.[34,42,43] In 2021, for these latter $OH^-(H_2O)_{n=0,1,2} + CH_3I$ reactions, along with other nucleophiles (F^-, Cl^-, Br^-, I^-), Ji *et al.* characterized the potential energy surfaces (PESs) of the front-side complex mechanisms utilizing the B97-1/ECP/d method.[44]

In contrast to the OH^-, CN^- has two reactive centres due to the weak dipole, thus two distinct products can be formed in case of the $CN^- + CH_3Y$ S_N2 reactions: CH_3CN or CH_3NC. Several studies were reported, which did not examine the ambident character of the CN^- and the C–C bond formation was considered only.[4,45–48] For the reactions between CN^- and methyl, ethyl, isopropyl, and tert-butyl iodine, Garver *et al.* determined the rate constants and measured the kinetic isotope effects to assess the effects of various solvents.[49,50] Later, Wang and co-workers carried out quantum mechanics/molecular mechanics computations for the $CN^- + CH_3Cl/CH_3Br$ reactions in aqueous solution.[51,52] In 2015, the $CN^- + CH_3I$ S_N2 reaction was investigated experimentally and theoretically by Carrascosa *et al*,[53] which was the first study taking into account the C–C and C–N bond formation, as well. It was found that both reaction routes have the same submerged double-well potential energy profile, and the experimental velocity distributions showed

the usual dual dynamics feature: At low E_{coll}, indirect process dominates, but already at E_{coll} = 0.7 eV the direct traditional backward mechanism is more favoured. The applied experimental method could detect the I^- product only, thus the direct separation of the CH_3CN and CH_3NC products was unfeasible. However, from the translational energy of the I^-, it was possible to predict the branching ratio of the isomers.

For the $X^- + C_2H_5Y$ reactions, S_N2 can be superseded by bimolecular elimination (E2), resulting in the formation of the $Y + HX + C_2H_4$ products, as Figure 1.3 shows. Two mechanisms can be distinguished within E2: *syn*-E2 and *anti*-E2, depending on that the breaking C–Y and C–H bonds are in *syn* or *anti* arrangements.[54]

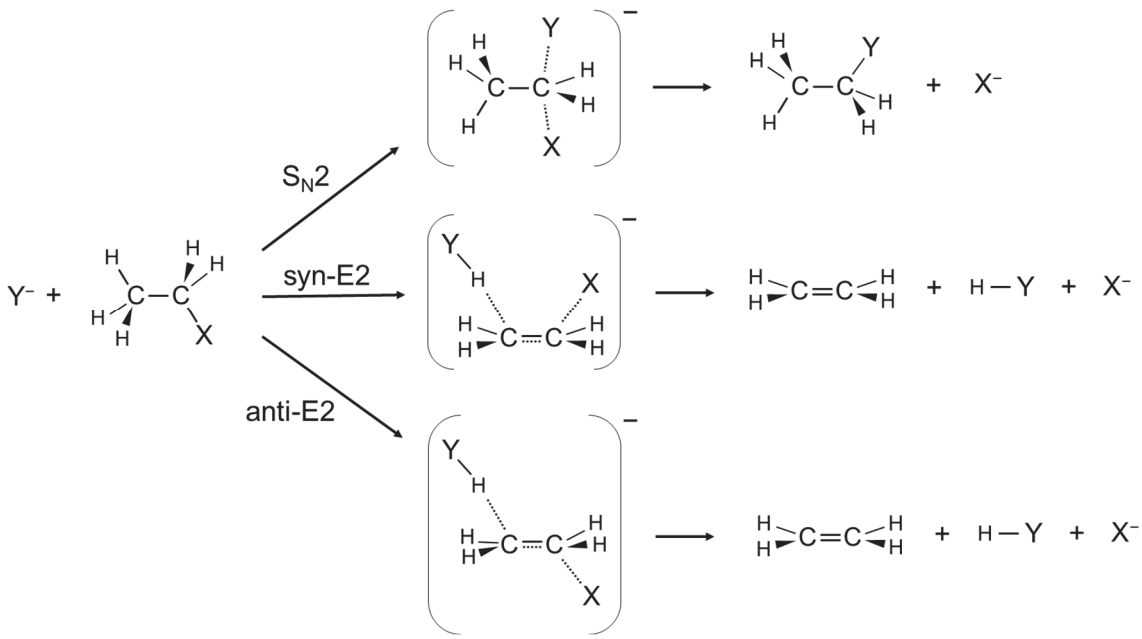

Figure 1.3 The schematic pathways of the S_N2, syn-E2 and anti-E2 channels for the $Y^- + CH_3CH_2X$ reaction.

From the 1980s, several studies have been focused on the competition between S_N2 and E2.[55–64] The identical $X^- + CH_3CH_2X$ (X = F, Cl) and $F^- + CH_3CH_2Cl$ S_N2 and E2 reactions were characterized by Minato *et al.* using Hartree–Fock (HF) and MP2 methods.[55,56] The reactions between F^-/PH_2^- and CH_3CH_2Cl were examined by Bierbaum and co-workers[59] verifying that the second-row nucleophiles are less-suited for E2 reactions than the first-row nucleophiles. For the $X^- + CH_3CH_2X$ (X = F, Cl), various investigations were carried out by Bickelhaupt *et al.*,[60,65–67], Merrill *et al.*,[68] Ensing *et al.*[69] and Truhlar *et al.*,[70] which allowed to probe the accuracy of the employed *ab initio*

methods and density functionals. Schettino *et al.* reported an *ab initio* molecular dynamics study on the $F^- + CH_3CH_2Cl$ reaction analysing the temperature dependence of the S_N2 and E2 mechanisms.[71] Ren and co-workers analysed the reactivity trends of numerous $X^- + CH_3CH_2Cl$ (X = F, Cl, Br, OH, SH, NH_2, PH_2, *etc.*) reactions with Gaussian-2 theory, and a strong agreement was brought to light between the electronegativity of X and the barrier heights of the corresponding S_N2 and E2.[72] In 2017, the characterization of the $F^- + CH_3CH_2I$ S_N2 and E2 channels was accomplished by the Hase group utilizing the MP2 and CCSD(T) methods.[73] Later, Hamlin and co-workers presented a description of the $X^- + CH_3CH_2Y$ [Y, X = F, Cl, Br, I, At] reactions to interpret the propensity of the nucleophilicity or protophilicity of the attacking X^-, which promotes the S_N2 or E2 reactions, respectively.[74] For the $F^- + CH_3CH_2Cl$ reaction, Tajti and Czakó computed the benchmark energies, geometries and frequencies of the stationary points, and compared the results of certain lower levels of theory.[75] Afterwards, in cooperation with Wester group, an experimental–theoretical study on the $F^- + CH_3CH_2Cl$ reaction presented the first global, accurate PES for a nine-atomic system, which described the dynamics of the possible S_N2, anti-E2, syn-E2 paths.[76] In 2020, Vermeeren *et al.*,[77] correcting the earlier study,[59] "revisited" the cases of $F^-/PH_2^- + CH_3CH_2Cl$. They showed that the higher proton affinity of the F^- is the reason why the reaction of $F^- + CH_3CH_2Cl$ promotes E2, while the less basic PH_2^- rather prefers the S_N2 pathway. For the $X^- + RY$ (X, Y = F, Cl, Br, I, *etc.*; R = CH_3CH_2, $(CH_3)_2CH$, $(CH_3)_3C$, *etc.*) reactions, the effects of the alkyl and the leaving groups on the competition between S_N2 and E2 were investigated by numerous papers.[21,47,50,57,78–84] Wester and co-workers, with respect to the reactions that belong to the type of $X^- + RI$ (X = Cl, CN; R = CH_3, C_2H_5, $^iC_3H_7$), revealed that the size of R does not have a significant effect on the S_N2 and E2 mechanism.[83] Recently, in the cases of $OH^- + RBr$, Pendás and co-workers investigated the steric hindrance suggesting that S_N2 is more sensitive to structural changes of the electrophile than E2.[78] The solvent effect on rivalry of the S_N2 and E2 pathways has been in the centre of the interest, as well.[49,85–89] The impacts of different solvents were examined for the reaction of $F^- + CH_3CH_2Br$ by Satpathy *et al.*, and the stationary points of the gas-phase reaction was also characterized at the CCSD(T)/aug-cc-pVDZ level of theory.[87] For the reaction of fluoride with ethyl chloride, in the solvent of water or dichloromethane, Hansen *et al.* reported that if the solvation is strong, like for the water, and not for the CH_2Cl_2, the preference is altered from E2 to S_N2.[89]

In the recent study of Wu and co-workers,[90] the $OH^-(H_2O)_{n=0-4} + CH_3CH_2Y$ [Y = Cl, Br, I] reactions were characterized by using the CCSD(T)/PP/t method at the MP2/ECP/d structures in order to describe the solvent effect on the competition between the S_N2 and E2 mechanisms, and without considering the ZPE effects, an obvious order for the barriers of the mechanisms were identified:

$$S_N2 \text{ inversion} < \text{anti-E2} < \text{syn-E2} < S_N2 \text{ retention.} \quad (2)$$

As the degree of hydration increases, the barrier heights of the mechanisms increase. Moreover, reliable correspondences were exposed between numerous thermodynamical, structural parameters and barrier heights of the mechanisms. Moreover, in case of bulk solvation, which was simulated by a polarizable continuum model of water, the shape of the double-well PES clearly vanishes converting into a single-peak profile.

2 Motivation and objectives

From the middle of the 20th century, the S_N2 reactions between halide ions and methyl/ethyl halides have been highly preferred for experimental and theoretical investigations. Over the last two decades, S_N2 reactions involving di- or triatomic nucleophiles have been in the centre of the interest, as well, however, our knowledge of these reactions is still insufficient indicating that more studies should be carried out using a wide range of methods. Thus, my doctoral work concentrates on non-typical gas-phase S_N2 reactions with the following primary objectives:

(i) Provide a benchmark *ab initio* comparative study for the $OH^- + CH_3Y/CH_3CH_2Y$ [Y = F, Cl, Br, I] S_N2 reactions determining the structures, energies and harmonic vibrational frequencies of the stationary points of the Walden-inversion, front-side attack and double-inversion pathways using the modern explicitly-correlated CCSD(T)-F12b method. For $OH^- + CH_3CH_2Y$, besides S_N2, E2 reaction is investigated, as well.

(ii) Characterize the stationary points of the $X^- + CH_3Y$ [X = CN, SH, NH_2, PH_2; Y = F, Cl, Br, I] S_N2 reactions utilizing the CCSD(T)-F12b method to examine the potential energy surfaces of the pathways.

(iii) Construct global analytical potential energy surfaces using the in-house ROBOSURFER program package for the selected three reactions: $OH^- + CH_3I$, $OH^- + CH_3F$ and $NH_2^- + CH_3I$. Implementing these potential energy surfaces, quasi-classical trajectory computations are carried out to present high-level dynamical characterizations and to reveal possible covert features of the above-mentioned reactions.

(iv) In case of the $OH^- + CH_3I$ reaction, supplement the dynamical results with the reanalysed crossed-beam imaging experiments obtained by the group of Roland Wester aiming to provide a theoretical–experimental comparison of the possible reaction channels.

3 Theoretical background

One of the main goals of the quantum chemical methods is to determine the geometries, electron structures, as well as, the physical-chemical properties of atoms and molecules at a quantum mechanical level.[91] The quantum chemical methods can be divided into two main categories: Wave function-based and density-based methods. The total energy (E_{tot}) and the wave function (Ψ) of a given system is determined by the non-relativistic, time-independent Schrödinger equation:

$$\widehat{H}_{\mathrm{tot}}\Psi = E_{\mathrm{tot}}\Psi, \tag{3.1}$$

where the $\widehat{H}_{\mathrm{tot}}$ is the Hamiltonian operator. $\widehat{H}_{\mathrm{tot}}$ is calculated as the sum of the kinetic energy operators of the electrons and nuclei, the potential energy operator of the electron–nucleus attractive interactions and the potential energy operators of the electron–electron and nucleus–nucleus repulsive interactions. Note that Eq. (3.1) is an eigenvalue equation, and excluding a few instances, the equation has no exact solution, hence approximations must be employed. The mainstay of the wave function-based methods is the Born–Oppenheimer approximation,[92] which enables us to separate the motion of nuclei and electrons from each other, because as a consequence of their considerable mass difference, the electrons immediately "respond" to the displacements of the nuclei. Therefore, within $\widehat{H}_{\mathrm{tot}}$, the nuclear kinetic energy is negligible and the nucleus-nucleus repulsion can be considered as a constant, and by solving the electronic Schrödinger equation, the nuclear configuration-dependent electronic energy and electron wave function can be obtained. Depending on the extent of the contribution of the nuclear kinetic energy to the total electronic energy, we can distinguish adiabatic, non-adiabatic and diagonal-corrected Born–Oppenheimer approximations. By solving the electronic Schrödinger equation at each nuclear configuration, the global PES of the system is provided.[93] On the PES of a chemical system, some "unique", so-called stationary points can be localized: At these points, for each coordinate, the first derivates of the potential energy function is zero. To identify the maxima, minima and saddle points of the PES, the solution of the eigenvalue problem of the Hessian matrix must be considered under the following conditions: Only positive eigenvalues (minimum) *or* only negative eigenvalues (maximum) *or* at least one eigenvalue is negative and all the others are positive (saddle point). In chemical systems, the first-order saddle points are important,

as these are the transition states, which connect two minima with the lowest energy barrier. In the course of the geometry optimization of the stationary points, usually, the quasi-Newton algorithms are utilized.[94,95] To characterize the stationary points (calculating the vibrational frequencies and ZPEs), the normal mode analysis procedure is applied, whereby the frequency (v_i) of a normal mode is determined as follows:

$$v_i = \frac{\sqrt{\lambda_i}}{2\pi}, \tag{3.2}$$

λ_i is the *i*th eigenvalue of the converted Hessian matrix, where $i = 1, \ldots, 3N-6$ ($3N-5$) in case of a non-linear (linear) *N*-atomic molecule. Consequently, a transition state (first-order saddle point) has a sole imaginary frequency, as a result of the negative eigenvalue.

3.1 *Ab initio* quantum chemical methods

In order to construct a representative PES of a chemical system describing the chemically important regions, a significant number of energy points must be calculated as accurately as possible. Hence, in the following sections, a brief overview of the employed *ab initio* methods is presented.[91]

3.1.1 Hartree–Fock theory

Considering the independent particle approximation and the antisymmetry principle, the eigenstates of the Hamiltonian operator can be described by using a Slater determinant in case of an independent electron system:

$$\Psi(\mathrm{x}_1, \mathrm{x}_2, \ldots, \mathrm{x}_N) = \frac{1}{\sqrt{N!}} \begin{vmatrix} \psi_1(\mathrm{x}_1) & \psi_1(\mathrm{x}_2) & \ldots & \psi_1(\mathrm{x}_N) \\ \psi_2(\mathrm{x}_1) & \psi_2(\mathrm{x}_2) & & \psi_2(\mathrm{x}_N) \\ \vdots & & \ddots & \vdots \\ \psi_N(\mathrm{x}_1) & \psi_N(\mathrm{x}_2) & & \psi_N(\mathrm{x}_N) \end{vmatrix}, \tag{3.3}$$

where ψ_i denotes the spin orbital (the product of a spatial orbital and a spin function), and *N* is the number of the electrons of the system. Applying the Slater-determinant form of the electronic wave function, the expectation value of the energy can be obtained from the electronic Schrödinger equations as:

$$E = \langle \Psi | \hat{H} | \Psi \rangle = \langle \Psi | \hat{H}_0 | \Psi \rangle + \langle \Psi | \hat{H}_1 | \Psi \rangle + \langle \Psi | \hat{H}_2 | \Psi \rangle, \tag{3.4}$$

where $\hat{H}_0$ is the zero-electron operator (nucleus–nucleus repulsive interaction), $\hat{H}_1$ is the one-electron operator (kinetic energy of the electrons and electron–nucleus attractive interactions) and $\hat{H}_2$ is the two-electron operator (electron–electron repulsive interactions). Regarding the latter interaction, each electron is described as interacting with the averaged nonlocal potential produced by the other electrons (mean field approximation). Using the Slater–Condon's rule, the follow equation can be obtained:

$$E = H_0 + \sum_i H_{ii} + \sum_{i>j} (J_{ij} - K_{ij}), \tag{3.5}$$

where H_0 is a constant, H_{ii} is the one-electron contribution, J_{ij} is the Coulomb integral and K_{ij} is the exchange integral. According to the variational principle, the electronic energy is always an upper bound to the exact energy. The goal is to determine the minimum of the $E[\Psi]$ functional taking into account the corresponding orthonormality condition, thus the Lagrange multiplier method must be considered. At extremum, the canonical Hartree–Fock (HF) equation is derived:

$$\hat{F}|\psi_i\rangle = \varepsilon_i|\psi_i\rangle, \qquad i = 1, \ldots, N, N+1, \ldots \tag{3.6}$$

where $\hat{F}$ is the Fock operator. As $\hat{F}$ is a one-particle operator, which depends on the occupied orbitals, thus Eq. (3.6) must be solved iteratively applying the self-consistent field (SCF) procedure. The atomic and molecular orbitals are expanded as a linear combination of basis functions, therefore, Eq. (3.6) leads to the Hartree–Fock–Roothaan equations:

$$\mathbf{FC} = \mathbf{SC}\boldsymbol{\varepsilon}, \tag{3.7}$$

where **F** is the Fock matrix, **C** is the coefficient matrix, **S** is the overlap matrix, and $\boldsymbol{\varepsilon}$ is the (diagonal) matrix of the orbital energies.

Owing to the above-mentioned independent particle and mean field approximations, the HF method provides inaccurate results for the most cases. To

improve the accuracy of the HF method, the correlated motion of the electrons must be considered. In other words, the difference between the HF limit energy ($E_{\mathrm{HF}}^{\mathrm{limit}}$) and the exact non-relativistic energy (E_{exact}) of the system must be determined:

$$E_{\mathrm{corr}} = E_{\mathrm{exact}} - E_{\mathrm{HF}}^{\mathrm{limit}}. \tag{3.8}$$

In the following, two of the most common post-HF *ab initio* methods (Møller–Plesset perturbation theory and coupled cluster theory) are presented in a summarized manner.

3.1.2 Møller–Plesset perturbation theory

Based on the Rayleigh–Schrödinger perturbation theory, we define a perturbation operator ($\widehat{W}$) as the deviation of the perturbed ($\widehat{H}$) and unperturbed ($\widehat{H}_0$) Hamiltonian operators:[96,97]

$$\widehat{W} = \widehat{H} - \widehat{H}_0, \tag{3.9}$$

where $\widehat{H}_0$ is the sum of the Fock operators:

$$\widehat{H}_0 = \sum_i \widehat{F}_i. \tag{3.10}$$

Thus, $\widehat{W}$ is the difference between the two-electron part of the electronic Hamiltonian and the averaged nonlocal potential, since the one-electron operators are the same in $\widehat{H}$ and $\widehat{H}_0$. The zeroth- and first-order corrections are:

$$E^{(0)} = \sum_i \varepsilon_i, \text{ and} \tag{3.11}$$

$$E^{(1)} = \langle \Psi_0 | \widehat{W} | \Psi_0 \rangle, \tag{3.12}$$

where Ψ_0 is the HF determinant, so the first-order Møller–Plesset (MP1) method provides the HF energy (the sum of $E^{(0)}$ and $E^{(1)}$). Applying the Brillouin's theorem and the Slater–Condon's rule, the second-order correction can be obtained as:

$$E^{(2)} = \sum_i \sum_{j>i} \sum_a \sum_{b>a} \frac{\left|\langle \Psi_0 | \widehat{W} | \Psi_{ij}^{ab} \rangle\right|^2}{E^{(0)} - E_{ij}^{ab}}, \tag{3.13}$$

hence, MP2 is the sum of the $E^{(0)}$, $E^{(1)}$ and $E^{(2)}$. Note that higher-order methods such as MP3 and MP4 exist, although they are not commonly used due to their extensive computational cost. Furthermore, while the MP*n* methods are size consistent, they are not variational methods, which means that the obtained energy can be lower than the E_{exact} of the system.

3.1.3 Coupled Cluster theory

In the course of the configuration interaction (CI) method,[91] the wave function is expanded as a linear combination of the HF determinant:

$$\Psi_{\text{CI}} = c_0 \Psi_0 + \sum_i \sum_a c_i^a \Psi_i^a + \sum_i \sum_{j>i} \sum_a \sum_{b>a} c_{ij}^{ab} \Psi_{ij}^{ab} + \cdots, \tag{3.14}$$

where singly, doubly *etc.* excited configurations of the HF Slater determinant ($\Psi_i^a, \Psi_{ij}^{ab}, ...$) are taken into account and the corresponding coefficients of the expansion ($c_0, c_i^a, c_{ij}^{ab}, ...$) are determined variationally. The full CI is achieved by considering every possible configuration, which provides the exact result serving as a reference for other quantum chemical methods. Although, the CI method is not commonly utilized, because in addition to its slow convergence, size consistency only fulfilled in the full CI case, which is greatly expensive.

In the coupled cluster (CC) method,[98–100] the wave function can be defined as:

$$\Psi_{\text{CC}} = e^{\hat{T}} \Psi, \tag{3.15}$$

solving the problem of size consistency. The Ψ is the Slater determinant of the HF orbitals and $\hat{T}$ is the excitation operator:

$$\hat{T} = \hat{T}_1 + \hat{T}_2 + \cdots + \hat{T}_N, \tag{3.16}$$

where

$$\hat{T}_1\Psi = \sum_i \sum_a t_i^a \, \Psi_i^a \,, \tag{3.17}$$

$$\hat{T}_2\Psi = \sum_{i<j} \sum_{a<b} t_{ij}^{ab} \, \Psi_{ij}^{ab} \,, \tag{3.18}$$

and the t expansion coefficients are called as amplitudes. Thus:

$$e^{\hat{T}} = 1 + \hat{T} + \frac{1}{2}\hat{T}^2 + \frac{1}{3!}\hat{T}^3 + \cdots, \tag{3.19}$$

and the energy is obtained as:

$$E_{\mathrm{CC}} = \left\langle \Psi \middle| \hat{H} e^{\hat{T}} \middle| \Psi \right\rangle. \tag{3.20}$$

The most common methods are the CC singles and doubles (CCSD) and the CC singles, doubles involving the triples contribution assessed by perturbation theory (CC singles, doubles and perturbative triples, CCSD(T)).[101–103] The CCSD(T) method is known as the gold-standard in quantum chemistry, and was developed to approximate the accuracy of the expensive CCSDT method.[104] The more accurate hybrid method utilized in the thesis is CCSDT(Q), where the quadruples contribution is determined by perturbation theory, however due to the extremely high computational cost, this method is used with reduced basis sets.[105] In some cases, the robust CCSD(T) method may not give tolerable results for systems with homolytic bond dissociation: A failure at the (T) computations befalls.[106] To address this problem, by employing the Brueckner-orbital-based BCCD and BCCD(T) methods, among others, we can get more accurate results in accordance with the CCSD and CCSDT methods. In the course of these BCCD and BCCD(T) methods, Brueckner orbitals are used instead of the HF orbitals, therefore in Eq. (3.17), the coefficients of the singly excited configurations are diminished to zero.[107]

To assess the multi-reference character of the wave function, a so-called T_1-diagnostic can be evaluated:[108]

$$T_1 = \sqrt{\frac{\sum_i \sum_a t_i^{a\,2}}{N}}. \tag{3.21}$$

Typically, T_1 value above 0.02–0.03 indicates the requirement of multi-reference methods because of the strong non-dynamic correlation effects.

Explicitly correlated (F12a/F12b) CC methods extend traditional CC theory by incorporating explicit treatment of electron correlation into the wave function.[109,110] That is achieved by adding additional terms to the wave function, which explicitly depend on the r_{12} electron-electron distances. In general, the basis set convergence of F12 methods is better than the traditional non-F12 methods, meaning that the calculated results obtained using F12 methods are less sensitive to the choice of the basis set and converge more rapidly with increasing basis set size. For instance, the result obtained at the CCSD(T)-F12b/aug-cc-pVDZ level of theory attains or even surpasses the accuracy of the more expensive CCSD(T)/aug-cc-pVTZ calculation.

3.1.4 Basis sets

As mentioned earlier, the atomic and molecular orbitals are expanded as a linear combination of basis functions. Initially, Slater-type orbitals (STO) were utilized, despite the fact that the calculation of the integrals can be obtained numerically:

$$\chi_{l,m,n}^{\mathrm{STO}}(r,\varsigma) = Rx^l y^m z^n e^{-r\varrho}\,, \tag{3.22}$$

where R is a normalization constant and l, m, n and ς are parameters. The Gauss-type orbitals (GTO) were first introduced by Boys and defined as:[111]

$$\phi_{l,m,n}^{\mathrm{GTO}}(r,\varsigma) = Rx^l y^m z^n e^{-r\varrho^2}\,, \tag{3.23}$$

which can be calculated analytically. STOs have similar properties to the hydrogen-like orbitals, however GTOs differ from them. In order to resolve this problem, contracted GTOs (CGTO, linear combination of several primitive GTOs) must be applied to resemble 1 STO:

$$\phi_i^{\mathrm{CGTO}} = \sum_{j=1}^{k} c_{ji}\,\phi_{ji}^{\mathrm{GTO}}\,, \tag{3.24}$$

where k is the contraction rate and c_{ji} is the corresponding contraction coefficient. The simplest basis set is STO-*n*G, in which each STO is approximated by a linear combination of n = 2–6 primitive Gaussian functions. The split-valence type basis sets (*n*-*abc*G) were

developed by Pople and co-workers,[112,113] where the core orbitals are represented as a linear combination of Gaussian functions as usual, but the valence shell orbitals are split into two, three, or more parts [double zeta (DZ), triple zeta (TZ), quadruple zeta (QZ), ...] and separate basis sets are assigned to each part. For example, in case of the 3-21G basis set for the carbon atom ($1s^2$, $2s^2$, $2p^2$): The 1s core orbital requires 3 GTOs and the 2s and 2p valence shell orbitals are split into two parts and each part is represented by 2 and 1 GTOs. Thus, 9 CGTOs (1s, 2s, 2s', $3p_x$, $3p_x$', $3p_y$, $3p_y$', $3p_z$, $3p_z$') and 15 primitive GTOs are applied for the carbon atom (3 GTOs for 1s, 2 GTOs for each of the unpunctuated orbitals of 2s, $3p_x$, $3p_y$, $3p_z$ and 1 GTO for each of the punctuated orbitals of 2s', $3p_x$', $3p_y$', $3p_z$'). The basis sets are often complemented with polarization functions, which add higher angular momentum functions to improve flexibility. Following the name of the basis set, the applied polarization functions are denoted by a * (heavy atoms) or ** (heavy and light atoms) or by the appropriate letters in brackets (d, p, …). The other complementary functions are the diffuse functions (GTOs with smaller exponents, denoted by + or ++), which describes the long-range interactions more accurately. The most widely used basis functions are the correlation-consistent basis sets (cc-pV*n*Z) designed by Dunning and co-workers,[114–116] where "p" denotes the applied polarization functions, and "*n*" is the cardinal number [DZ (double-zeta), TZ (triple-zeta), …]. The "aug" prefix (abbreviation for augmented) indicates the employment of the diffuse functions. It should be noted that for all-electron calculations, the aug-cc-pwCV*n*X basis sets are utilized,[117] which consider the correlation of electrons on the core orbitals, as well. In the matter of the scalar relativistic effects, effective core potentials (ECP) are used with the corresponding pseudopotential basis sets to represent the non-negligible effects of the core electrons for the elements with higher atomic number.[118,119]

3.2 Quasi-classical trajectory method

Kinetics and dynamics are two crucial aspects of the studies of chemical reactions (Figure 3.1). Kinetics focuses on the rate of the reaction: By following the time-dependent concentration [$c(t)$] of the chemical species, the rate constant [$k(t)$] can be determined as a function of temperature. In a chemical investigation, several factors that affect the reaction rate can be taken into account, such as temperature, concentration of the reactants, catalysts, *etc.* On the other hand, dynamics delves into the mechanisms of the reaction to gain a more profound understanding of how the reaction takes place at atomic

and molecular level. Dynamics is essential in understanding the energy changes that occur during the reaction, as well. The most important dynamical outcome of a reaction is the E_{coll}-dependent cross section [$\sigma(E)$], from which the rate constant can be calculated using a Boltzmann factor [$f(E,T)$] at a given temperature (see Figure 3.1).

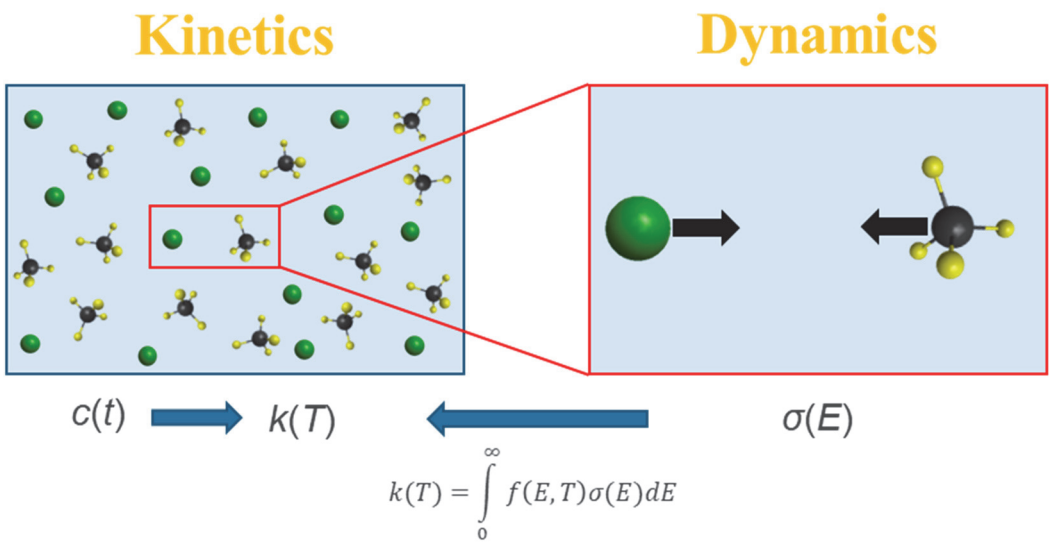

Figure 3.1 The kinetical and dynamical aspects of a representative chemical reaction.

Simulating chemical reactions is a complex process that involves two key stages. Firstly, we must solve the Schrödinger equation for the electrons at fixed nuclear configuration resulting in the PES of the reaction, which provides the potential energy of the system. The negative gradient of the PES at each point governs the motion of the atoms in a reaction. The movement of the nuclei on the PES can be determined using either quantum or classical mechanical methods. The solution of the time-dependent nuclear Schrödinger equation gives the exact theoretical description of the nuclei's movement, however it is practicable for only smaller systems (usually < 5–6 atoms) due to its substantial computational demands. Therefore, it is more advisable to simulate polyatomic chemical reactions using classical methods. One of the most widespread methods is the quasi-classical trajectory (QCT) method,[120] which can be distinguished into two types. In the course of the direct dynamics simulation,[121] the potential energy and the corresponding gradient is computed at each nuclear configuration ("on-the-fly"). However, for one trajectory, usually more than tens of thousands of potential energy points and gradients are needed, moreover, in case of a comprehensive dynamical investigation of a reaction, even more than 1 million trajectories are required. Thus, solely

the utilization of low theoretical levels (HF, MP2, DFT, …) is attainable, which can significantly degrade the accuracy of the results. To address this issue, the PES can be represented by an analytical function facilitating efficient calculations of the potential energies and gradients during a dynamical simulation. In general, a function representing a PES involves the computations of up to 50–100 thousand energy points opening the door for high-level *ab initio* methods. Three requirements must be fulfilled by the analytical function: Invariance with respect to translation, rotation, and permutation of identical atoms. The first and the second conditions can be satisfied by using an appropriate internal coordinate system, and the third condition can be fulfilled by the permutationally invariant polynomial (PIP) approach. The Morse-type variables are used, defined as:

$$y_{ij} = e^{\frac{r_{ij}}{a}}, \tag{3.25}$$

where r_{ij} is the atom-atom distance, and a is a parameter, which is usually 2 or 3 bohr. By using these y_{ij} variables, we can ensure the correct asymptotic behaviour of the PES. The PES is represented by the following function form:[122,123]

$$V = \sum_{n=0}^{N} C_n S({y_{12}}^{n_{12}} {y_{13}}^{n_{13}} \dots {y_{23}}^{n_{23}} {y_{24}}^{n_{24}} \dots), \tag{3.26}$$

where S is a symmetry operator, which generates all permutationally equivalent monomials, and C_n [$n = n_{12}, n_{13}, n_{23}, n_{24}, \dots$] refers to the coefficients obtained by performing a weighted linear least squares fitting. D is the order of the fit:

$$D = \sum_{i=1}^{N-1} \sum_{j=i+1}^{N} n_{ij}, \tag{3.27}$$

and the number of coefficients that need to be determined depends on the degree of the fit, the number of atoms, and the permutational symmetry. To enhance efficiency, the following form is utilized for PES representation:

$$V(\mathbf{y}) = \sum_{n=0}^{N} h_n[\boldsymbol{p}(\mathbf{y})] q_n(\mathbf{y}), \tag{3.28}$$

where the h_n is an arbitrary polynomial of the primary invariant polynomials $\boldsymbol{p}(\mathbf{y})$ and $q_n(\mathbf{y})$ signifies the secondary invariant polynomials. It should also be noted that by identical permutation symmetry, we refer to the systems that belong to the same molecular type. The reactions studied in the thesis (OH^- + CH_3F/CH_3I and NH_2^- + CH_3I) belong to the A_4BCD and A_5BCD molecular types. The theory of PES fitting is discussed in greater detail in ref. 122 and 123.

The following sections provide a concise overview of the QCT methodology, as well as, of the in-house ROBOSURFER program utilized for automated PES development.[124]

3.2.1 Initial conditions and trajectory propagation

The QCT method applies special quasi-classical initial conditions,[120] where the energies of the reactants are carefully selected to align with a quantum mechanical vibrational-rotational state. The initial quasi-classical vibrational state is defined using normal mode sampling. The normal coordinates and corresponding momenta for an *N*-atom reactant are derived using the following formulas:

$$Q_k = \frac{\sqrt{2E_k}}{\omega_k}\cos(2\pi R_k)\,, \qquad P_k = \sqrt{2E_k}\sin(2\pi R_k) \qquad , k = 1, 2, \dots, 3N-6, \tag{3.29}$$

where the R_k is a random number between 0 and 1, ω_k is the harmonic frequency of the kth normal mode. E_k is the harmonic mode-specific vibrational energy:

$$E_k = \omega_k(n_k + \frac{1}{2}), \tag{3.30}$$

where n_k is the vibrational quantum number. Noteworthy, that for each mode, the harmonic classical vibrational energy can be computed using the following formula:

$$E_k = \frac{P_k^2}{2} + \frac{\omega_k^2\, Q_k^2}{2}, \tag{3.31}$$

and Q_k and P_k defined according to the formulas of Eq. (3.29). The $\mathbf{Q}(Q_1, Q_2, \dots, Q_{3N-6})$ and $\mathbf{P}(P_1, P_2, \dots, P_{3N-6})$ vectors are transformed to the corresponding Cartesian coordinates, **p** and momenta, **q**:

$$\mathbf{q} = \mathbf{q}_e + \mathbf{M}^{-1/2}\mathbf{L}\mathbf{Q}, \tag{3.32}$$

$$\mathbf{p} = \mathbf{M}^{1/2}\mathbf{L}\mathbf{P}, \tag{3.33}$$

where $\mathbf{q}_e$ is the initial equilibrium geometry, **M** is the diagonal mass matrix, and **L** is a transformation matrix containing the normal mode eigenvectors.

The initial angular momentum can be calculated as:

$$\mathbf{j_0} = \sum_{i=1}^{N_{\text{atoms}}} \mathbf{q_i} \times \mathbf{p_i}, \tag{3.34}$$

where N_{atoms} is the number of atoms. The desired angular momentum is set by the modification of the velocity vectors:

$$\mathbf{v}_i = \mathbf{v}_i^0 + \boldsymbol{\Omega} \times \mathbf{q}_i, \text{ where} \tag{3.35}$$

$$\boldsymbol{\Omega} = \mathbf{I}^{-1}(\mathbf{j} - \mathbf{j}_0). \tag{3.36}$$

I is the moment of inertia tensor, which is constructed as:

$$I_{xx} = \sum_{i=1}^{N_{\text{atoms}}} m_i(y_i^2 + z_i^2), \qquad I_{yy} = \sum_{i=1}^{N_{\text{atoms}}} m_i(z_i^2 + x_i^2), \tag{3.37}$$

$$I_{zz} = \sum_{i=1}^{N_{\text{atoms}}} m_i(x_i^2 + y_i^2), \qquad I_{xy} = I_{yx} = -\sum_{i=1}^{N_{\text{atoms}}} m_i x_i y_i, \tag{3.38}$$

$$I_{xz} = I_{zx} = -\sum_{i=1}^{N_{\text{atoms}}} m_i x_i z_i, \qquad I_{yz} = I_{zy} = -\sum_{i=1}^{N_{\text{atoms}}} m_i y_i z_i, \tag{3.39}$$

where (x_i, y_i, z_i) are the center-of-mass Cartesian coordinates of the *i*th atom of the corresponding product.

The internal energy of the reactant molecule can be determined with the help of the PES:

$$E = \frac{1}{2}\sum_{i=1}^{N_{\text{atoms}}} m_i \mathbf{v}_i (\mathbf{v}_i)^{\mathrm{T}} + V(\mathbf{q}) - V(\mathbf{q_e}) . \tag{3.40}$$

Due to the anharmonicity of the PES, by an iterative procedure modifications are required to the internal energy obtained from the above-described normal mode and rotational sampling:

$$\mathbf{q}^i = \mathbf{q}^0 + (\mathbf{q}^{i-1} - \mathbf{q}^{\mathbf{0}})(E^0_{\text{int}}/E^{i-1}_{\text{int}})^{1/2} , \tag{3.41}$$

$$\mathbf{p}^i = \mathbf{p}^{i-1}(E^0_{\text{int}}/E^{i-1}_{\text{int}})^{1/2} , \tag{3.42}$$

where *i* is the *i*th step of the iteration procedure. It should be highlighted that the reactions are studied with the $\mathbf{j} = 0$ conditions in the thesis.

In the scenario of a bimolecular reaction, the ensuing step is to configure a random orientation of the colliding reactant molecules/ions. The Cartesian coordinates and the velocities of the polyatomic reactants are rotated by an Euler rotation matrix:

$$\mathbf{q} = \mathbf{R}(\theta, \phi, \psi)\mathbf{q} , \tag{3.43}$$

$$\mathbf{v} = \mathbf{R}(\theta, \phi, \psi)\mathbf{v} . \tag{3.44}$$

Random selection of the Euler angles is performed based on the following equations:

$$\cos(\theta) = 2R_1 - 1 \ , \quad \phi = 2\pi R_2 \ , \ \psi = 2\pi R_3 , \tag{3.45}$$

where R_1, R_2 and R_3 are different uniform random numbers between 0 and 1. After the random orientation of the two reactants, the center of mass of one molecule is set to the origin, while in case of the other molecule, its centre of mass is located at the following coordinates:

$$x = \sqrt{s^2 - b^2}, \quad y = b \ , \ z = 0 , \tag{3.46}$$

where *s* is the initial distance between the center of masses of the reactants and *b* is the impact parameter (see Figure 3.2).

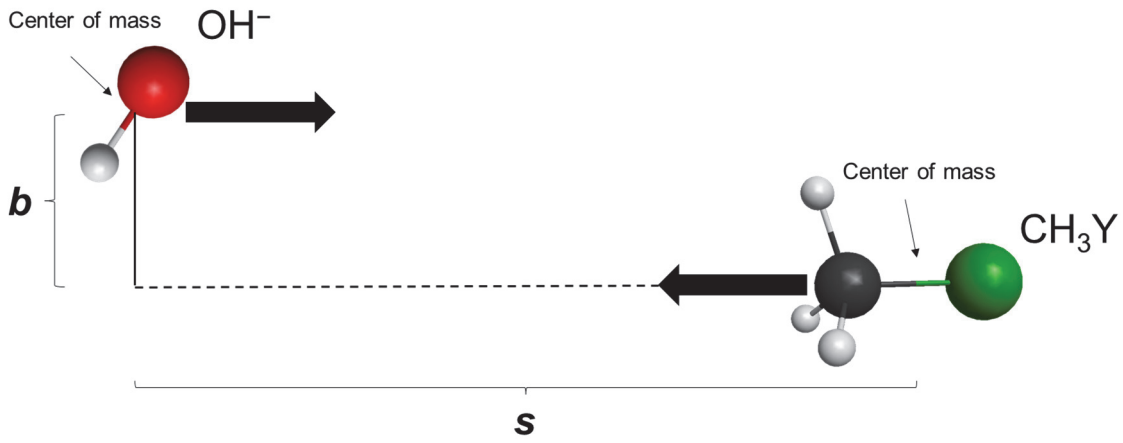

Figure 3.2 The initial arrangement of the OH^- and CH_3Y reactants showing the impact parameter (*b*) and the distance between the center of the masses (*s*).

The relative velocity of the reactants is determined by:

$$v_{rel} = [2E_{coll}(m_A + m_B)/(m_A m_B)]^{1/2}, \tag{3.47}$$

where E_{coll} is the collision energy, and m_A and m_B are the masses of the reactants. The velocity vectors of each atom of the reactants are:

$$v_A = (m_B/(m_A + m_B)v_{rel}, 0, 0), \text{ and} \tag{3.48}$$

$$v_B = (-m_A/(m_A + m_B)v_{rel}, 0, 0). \tag{3.49}$$

With the initial coordinates and velocities at hand, we propagate trajectories using well-known numerical methods (such as the Verlet algorithm). The basic concept is to numerically solve the Newton's equations of motion:

$$\mathbf{F} = m\mathbf{a}, \tag{3.50}$$

which can be defined as:

$$-\frac{\partial V(\mathbf{q})}{\partial \mathrm{q}}=\frac{\partial \mathbf{p}}{\partial t}. \tag{3.51}$$

Employing the Lagrangian formalism, the equation of motion is:

$$\frac{\mathrm{d}}{\mathrm{d}t}\frac{\partial L(\mathbf{q},\mathbf{p})}{\partial \dot{\mathbf{q}}}-\frac{\partial L(\mathbf{q},\mathbf{p})}{\partial \mathbf{q}}=0\,, \tag{3.52}$$

where the Lagrange function (L) is the difference between kinetic (T) and potential energy (V):

$$L(\mathbf{q},\mathbf{p})=T(\mathbf{q},\mathbf{p})-V(\mathbf{q})\,. \tag{3.53}$$

According to the Hamiltonian formalism, the equations of motion are given as:

$$\frac{\mathrm{d}\mathbf{q}}{\mathrm{d}t}=\frac{\partial H(\mathbf{q},\mathbf{p})}{\partial \mathbf{p}}, \text{ and} \tag{3.54}$$

$$\frac{\mathrm{d}\mathbf{p}}{\mathrm{d}t}=-\frac{\partial H(\mathbf{q},\mathbf{p})}{\partial \mathbf{q}}, \tag{3.55}$$

where the Hamiltonian function (H) is the sum of kinetic and potential energy:

$$H(\mathbf{q},\mathbf{p})=T(\mathbf{q},\mathbf{p})+V(\mathbf{q})\,. \tag{3.56}$$

Note that, Eq. (3.54) and (3.55), as well as, Eq. (3.52) are equivalent with the Newton's equations of motion [Eq. (3.50)], and these equations are often preferred for solving complex systems that have a large number of degrees of freedom. Although, in order to solve the Newton's equations in our studies, the Verlet algorithm is employed due to its time-reversible feature, which preserves the sum of the kinetic and potential energy of the system during the trajectory propagation. By considering the Taylor expansion of the positions, the Verlet formula can be derived as:

$$\mathbf{r}(t+\Delta t)=\mathbf{r}(t)+\mathbf{v}(t)\Delta t+\frac{1}{2}\mathbf{a}(t)\Delta t^2+\frac{1}{6}\dot{\mathbf{a}}(t)\Delta t^3+\mathcal{O}(\Delta t^4)\,, \tag{3.57}$$

$$\mathbf{r}(t-\Delta t)=\mathbf{r}(t)-\mathbf{v}(t)\Delta t+\frac{1}{2}\mathbf{a}(t)\Delta t^2-\frac{1}{6}\dot{\mathbf{a}}(t)\Delta t^3+\mathcal{O}(\Delta t^4)\,, \tag{3.58}$$

where **r**, **v** and **a** denote the position, velocity and acceleration, in order. By summing the two equations and substituting the acceleration from Eq. (3.50), it follows that:

$$\mathbf{r}(t+\Delta t) = 2\mathbf{r}(t) - \mathbf{r}(t-\Delta t) + \frac{1}{2}\left(-\frac{1}{m}\nabla V(r(t))\right)\Delta t^2 + \mathcal{O}(\Delta t^4)\,. \qquad (3.59)$$

However, the velocities cannot be provided directly, thus, in case of our QCT simulations, the velocity Verlet algorithm is utilized:[125,126]

$$\mathbf{r}(t+\Delta t) = \mathbf{r}(t) + \mathbf{v}(t)\Delta t + \frac{1}{2}\mathbf{a}(t)\Delta t^2 \qquad (3.60)$$

$$\mathbf{v}(t+\Delta t) = \mathbf{v}(t) + \frac{1}{2}\big(\mathbf{a}(t) + \mathbf{a}(t+\Delta t)\big)\Delta t^2\,. \qquad (3.61)$$

In addition, it is crucial to mention that the accuracy of the results improves as the value of Δt decreases, but it also increases the computational cost.

3.2.2 Final conditions

The final Cartesian coordinates obtained from QCT simulations allow us to differentiate reactive and non-reactive trajectories, and to identify the possible reaction channels, as well. Typically, in the case of bimolecular reaction, QCT calculations are performed with fixed collision energy, vibrational, and rotational quantum numbers. At a given b, the reaction probability (opacity function) of each channel can be determined as:

$$P(b, E_{\text{coll}}, \mathbf{n}_{1,2}, J_{1,2}, K_{1,2}) = \frac{N_{\text{r}}(b, E_{\text{coll}}, \mathbf{n}_{1,2}, J_{1,2}, K_{1,2})}{N_{\text{total}}(b, E_{\text{coll}}, \mathbf{n}_{1,2}, J_{1,2}, K_{1,2})}, \qquad (3.62)$$

where N_{r} is the number of the reactive trajectories of the channel, N_{total} is the total number of the trajectories at a given fixed b, E_{coll}, $\mathbf{n}_{1,2}$ (vibrational quantum numbers of the reactants) and $J_{1,2}$ and $K_{1,2}$ (rotational quantum numbers of the symmetric top reactants). The reaction cross-section is obtained as:

$$\sigma(E_{\text{coll}}, \mathbf{n}_{1,2}, J_{1,2}, K_{1,2}) = \int_0^{b_{\max}} 2\pi b P(b, E_{\text{coll}}, \mathbf{n}_{1,2}, J_{1,2}, K_{1,2}) db\,, \qquad (3.63)$$

where b_{max} is the largest impact parameter at which reactive event can occur. We run trajectories at equidistant b values (Δb = const.), and the reaction cross-section of each channel is calculated using numerical integration:

$$\sigma\left(E_{\text{coll}}, \mathbf{n}_{1,2}, J_{1,2}, K_{1,2}\right) = \pi \sum_{n=1}^{n_{\max}} [b_n - b_{n-1}][b_n P\left(b_n, E_{\text{coll}}, \mathbf{n}_{1,2}, J_{1,2}, K_{1,2}\right) + b_{n-1} P\left(b_{n-1}, E_{\text{coll}}, \mathbf{n}_{1,2}, J_{1,2}, K_{1,2}\right)] , \tag{3.64}$$

where $b_n = n \cdot d$ $[n = 0, 1, 2, \ldots, n_{\max}]$ and d is usually 0.5 bohr.

The product relative translational energy can be calculated as:

$$E_{\text{trans}} = \frac{\mu \mathbf{v}_{\text{rel,products}}^2}{2}, \tag{3.65}$$

where:

$$\mathbf{v}_{\text{rel,products}} = \mathbf{v}_{\text{product,1}} - \mathbf{v}_{\text{product,2}}, \tag{3.66}$$

and $\mathbf{v}_{\text{product,1}}$ and $\mathbf{v}_{\text{product,2}}$ are the velocities of the center of masses of the products.

The velocity scattering angle, θ is the angle between the relative velocity of the center of masses of the reactants and the products (Figure 3.3) obtained as:

$$\theta = \cos^{-1}\left(\frac{\mathbf{v}_{\text{rel,reactants}} \cdot \mathbf{v}_{\text{rel,products}}}{\left|\mathbf{v}_{\text{rel,reactants}}\right| \cdot \left|\mathbf{v}_{\text{rel,products}}\right|}\right) . \tag{3.67}$$

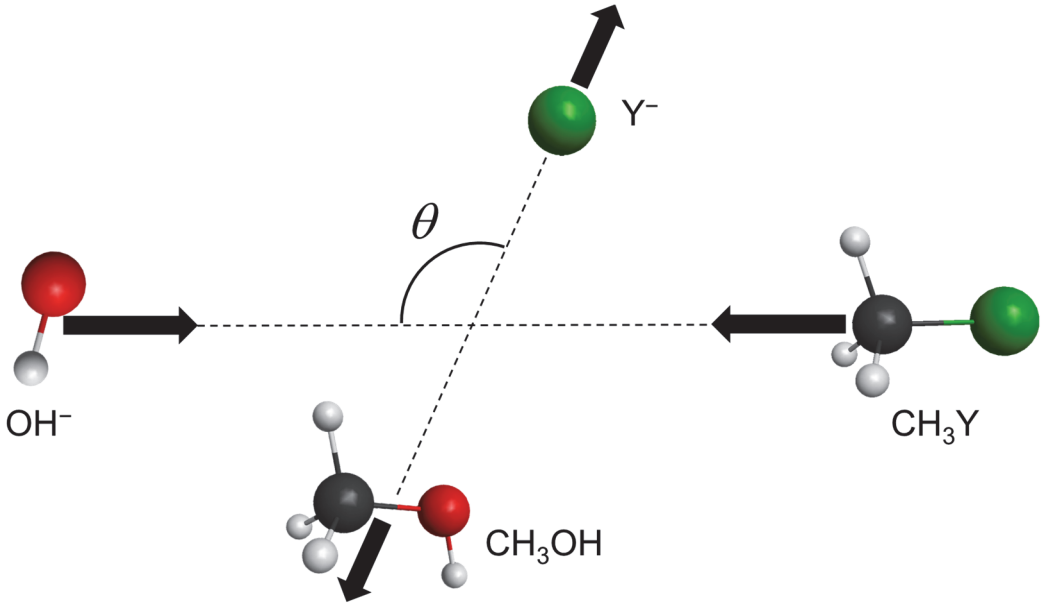

Figure 3.3 The scattering angle (θ) in case of the $OH^- + CH_3Y \rightarrow CH_3OH + Y^-$ S_N2 reaction.

The internal vibrational energy of the polyatomic products is defined as:

$$E_{\text{int}} = T + V\,, \tag{3.68}$$

where T is the kinetic energy and V is the potential energy. V is obtained from the analytical PES as a deviation between the energy of the product configuration and that of the equilibrium structure. T is the sum of kinetic energies of every atom:

$$T = \sum_{i=1}^{N_{\text{atoms}}} \frac{m_i \mathbf{v}_i^2}{2}, \tag{3.69}$$

where N_{atoms} is the number of atoms, m_i is the mass of the ith atom and $\mathbf{v}_i$ is the center of mass velocities of the ith atom.

Diagonalizing the moment of inertia tensor, $\mathbf{I}$, with the principal moments of inertia (I_a, I_b and I_c) we can calculate the angular velocity vector ($\boldsymbol{\omega} = \mathbf{I}^{-1} \cdot \mathbf{j}$). The rotational energy of the products is calculated as:

$$E_{\text{rot}} = \frac{1}{2}\boldsymbol{\omega} \cdot \mathbf{j}\,. \tag{3.70}$$

3.2.3 Configuration of the product: inversion or retention

Besides the Eckart-transformation-based method,[127,128] another more practical approach is utilized to define the configuration of the reactant and product molecules.[129] For a CH_3Y reactant in a traditional $X^- + CH_3Y \rightarrow CH_3X + Y^-$ S_N2 reaction, labelling the H atoms with 1–3, the following vectors are determined:

$$\mathbf{r}_{CY} = \mathbf{r}_Y - \mathbf{r}_C \qquad \mathbf{r}_1 = \mathbf{r}_{H_1} - \mathbf{r}_C \tag{3.71}$$

$$\mathbf{r}_2 = \mathbf{r}_{H_2} - \mathbf{r}_C \qquad \mathbf{r}_3 = \mathbf{r}_{H_3} - \mathbf{r}_C \quad , \tag{3.72}$$

where $\mathbf{r}_C, \mathbf{r}_Y, \mathbf{r}_{H_1}, \mathbf{r}_{H_2}$ and $\mathbf{r}_{H_3}$ are the Cartesian coordinates of the corresponding atoms. The **n** normal vector of the H_3CY plane and the s_1 and s_2 projections can be obtained as:

$$\mathbf{n} = \mathbf{r}_3 \times \mathbf{r}_{CY}, \tag{3.73}$$

$$s_1 = \mathbf{r}_1 \cdot \mathbf{n}, \tag{3.74}$$

$$s_2 = \mathbf{r}_2 \cdot \mathbf{n}. \tag{3.75}$$

If the sign of the $s_1 - s_2$ is opposite to the corresponding case of the CH_3X product, an inversion takes place in the course of the reaction. If the signs of the $s_1 - s_2$ deviations are same, a retention occurs. Although, in the thesis, due to the complexity of the examined systems, the possible S_N2 retention pathways are manually separated.

3.3 Automatized development of reactive potential energy surface: The ROBOSURFER program

Earlier studies utilized a manual four-step strategy to select the appropriate geometries (10^4–10^5) that cover the chemically significant regions on the PES.[124] In order to supplant this circumstantial method, Győri and Czakó developed the ROBOSURFER program

system,[124] which enables fully automated PES development. In Figure 3.4, the basic workflow diagram of the ROBOSURFER program is presented.

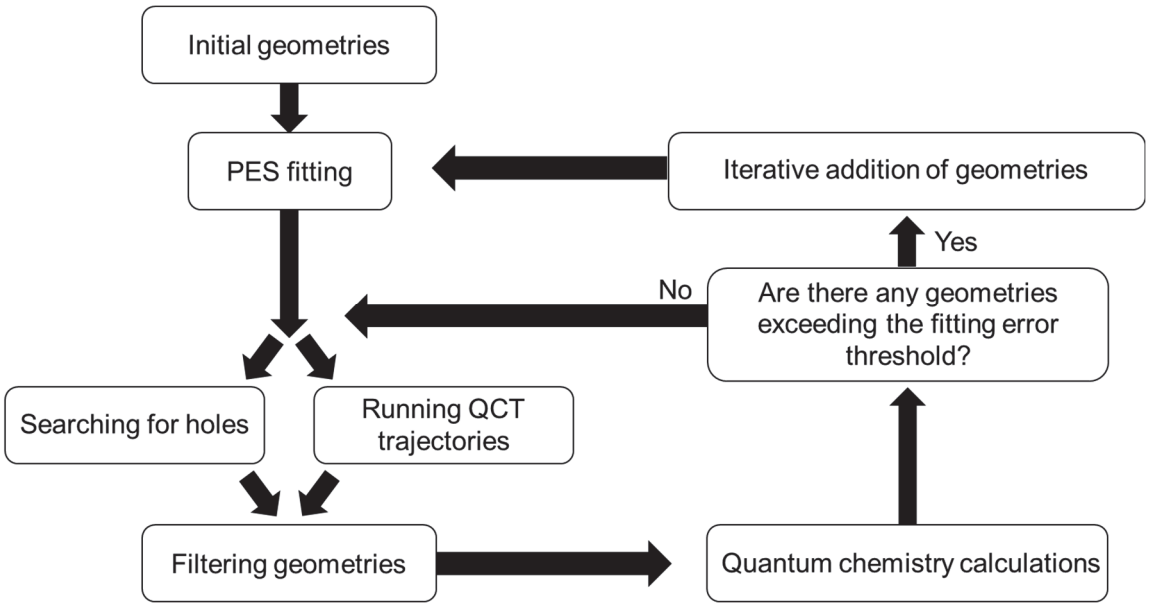

Figure 3.4 The basic operation flow diagram of the in-house developed ROBOSURFER program package.[124]

As a first step, an initial PES is constructed based on a preliminary set of geometries prepared from the known possible channels and stationary points of the reaction. Then, by running QCT simulations, new geometries are generated with the current PES. Subsequently, the most favourable geometries (where the probability of the highest fitting error is the greatest) are selected, and the energies of these structures are determined at the desired level of theory. Finally, the new geometries with significant fitting errors are added to the previous set, and the fit is redone. The entire loop is repeated, until the probability of unphysical trajectories (which generate energetically unobtainable products) decreases to an acceptable threshold (usually < 1 %). Note that it is also possible during an iteration to search for deep unreal minima on the current PES instead of running QCT simulations. These so-called "holes" can be explored by the HOLEBUSTER subprogram. For a more detailed description of the ROBOSURFER program, see ref. 124.

4 Results and discussion

4.1 Description of the potential energy surfaces

In order to build up a comprehensive picture of the chemical reaction of interest, the stationary points on the PES must be characterized at first.[130] For all reactions considered in the thesis ($X^- + CH_3Y$ [X = OH, SH, CN, NH_2, PH_2; Y = F, Cl, Br, I] S_N2 and $OH^- + CH_3CH_2Y$ [Y = F, Cl, Br, I] S_N2 and E2), the minima and transition states are searched at the MP2/aug-cc-pVDZ level of theory[96] based on previous studies and our chemical intuition. [3, 5, 8, 9] Then the structures, energies and harmonic vibration frequencies of the stationary points are computed using the explicitly-correlated CCSD(T)-F12b method[99,109,110] with the aug-cc-pVDZ and aug-cc-pVTZ basis sets.[114,131] For the open-shell systems, the corresponding restricted open-shell Hartree–Fock (ROHF) orbital-based restricted second-order Møller–Plesset perturbation theory (RMP2)[132] and the unrestricted explicitly-correlated UCCSD-F12b methods are utilized. For Br and I, small-core relativistic effective core potentials (ECPs) are used and the aug-cc-pV*n*Z-PP [*n* = 2 – 4] basis sets are applied to replace the inner-core $1s^22s^22p^6$ (Br) and $1s^22s^22p^63s^23p^63d^{10}$ (I) electrons.[133] For the $X^- + CH_3Y$ [X = SH, NH_2, PH_2; Y = F, Cl, Br, I] and the $OH^- + CH_3CH_2Y$ [Y = F, Cl, Br, I] systems the benchmark classical (adiabatic) energies of the stationary points at the CCSD(T)-F12b/aug-cc-pVTZ geometries, relative to the corresponding equilibrium reactants, are calculated as:

$$\Delta E\text{[CCSD(T)-F12b/aug-cc-pVQZ]} (+ \Delta\text{ZPE[CCSD(T)-F12b/aug-cc-pVTZ]}) \quad (4.1)$$

where ΔE is the classical relative energy and ΔZPE is the harmonic zero-point energy correction.

In the cases of $OH^- + CH_3Y$ and $CN^- + CH_3Y$ [Y = F, Cl, Br, I], other corrections are considered as well, to achieve more accurate relative energies,

1) Post-CCSD(T) correlations,[104,134] defined as:

$$\delta\text{[CCSDT]} = \Delta E\text{[CCSDT/aug-cc-pVDZ]} - \Delta E\text{[CCSD(T)/aug-cc-pVDZ]} \quad (4.2)$$

$$\delta\text{[CCSDT(Q)]} = \Delta E\text{[CCSDT(Q)/aug-cc-pVDZ]} - \Delta E\text{[CCSDT/aug-cc-pVDZ]}, \quad (4.3)$$

2) Core correlations, determined as:

$$\Delta\text{core} = \Delta E[\text{AE-CCSD(T)/aug-cc-pwCVTZ}] - \Delta E[\text{FC-CCSD(T)/aug-cc-pwCVTZ}], \quad (4.4)$$

where FC and AE refer to frozen-core and all-electron calculations.[135] The frozen-core approach correlates the valence electrons only, while the all-electron approach correlates the following electrons on the main shell below the valence shell: $1s^2$ (C, N, O, F), $2s^22p^6$ (P, S, Cl), $3s^23p^63d^{10}$ (Br) and $4s^24p^64d^{10}$ (I).

Thus, for the $OH^- + CH_3Y$ [Y = F, Cl, Br, I] S_N2 reactions, the benchmark classical relative energies at the CCSD(T)-F12b/aug-cc-pVTZ structures are computed as:

$$\Delta E[\text{CCSD(T)-F12b/aug-cc-pVQZ}] + \delta[\text{CCSDT}] + \delta[\text{CCSDT(Q)}] + \Delta\text{core}. \quad (4.5)$$

Considering the ZPE effects at the CCSD(T)-F12b/aug-cc-pVTZ level of theory, the benchmark adiabatic relative energies are obtained.

For the $CN^- + CH_3Y$ [Y = F and Cl] reactions, the scalar relativistic effects are assessed with Douglas−Kroll (DK)[136] AE-CCSD(T) calculations using the DK-optimized aug-cc-pwCVTZ-DK basis set:[137]

$$\Delta\text{rel} = \Delta E[\text{DK-AE-CCSD(T)/aug-cc-pwCVTZ-DK}] - \Delta E[\text{AE-CCSD(T)/aug-cc-pwCVTZ}]. \quad (4.6)$$

For Y = Br and I, the scalar relativistic effect cannot be evaluated, because ECP is applied with the pseudopotential-based aug-cc-pV*n*Z-PP [$n = 2 – 4$] basis sets for the non-DK computations, which involve scalar relativistic effects already. In the cases of these reactions, the DK-AE-CCSD(T)/aug-cc-pwCVTZ-DK (without ECP) and AE-CCSD(T)/aug-cc-pwCVTZ-PP (with ECP) energies are compared with a focus on the uncertainty of the ECP calculations, although these values are not considered in the final benchmark relative energies.

Hence, for the $CN^- + CH_3Y$ [Y = F and Cl] systems, the final benchmark classical (adiabatic) relative energies at the CCSD(T)-F12b/aug-cc-pVTZ structures are determined as:

$$\Delta E[\text{CCSD(T)-F12b/aug-cc-pVQZ}] + \delta[\text{CCSDT}] + \delta[\text{CCSDT(Q)}] + \Delta\text{core} + \Delta\text{rel} (+ \Delta\text{ZPE}), \quad (4.7)$$

and for $CN^- + CH_3Y$ [Y = Br and I]:

$$\Delta E[\text{CCSD(T)-F12b/aug-cc-pVQZ}] + \delta[\text{CCSDT}] + \delta[\text{CCSDT(Q)}] + \Delta\text{core} (+ \Delta\text{ZPE}), \quad (4.8)$$

where the ZPE effects are taken into account at the CCSD(T)-F12b/aug-cc-pVTZ level of theory. All electronic structure computations are performed with the MOLPRO program package,[138] except for CCSDT and CCSDT(Q), which are carried out with the MRCC program,[139,140] interfaced to MOLPRO.

4.1.1 The $OH^- + CH_3Y$ and the $OH^- + CH_3CH_2Y$ [Y = F, Cl, Br, I] reactions

The schematic representations of the PESs for the $OH^- + CH_3Y/CH_3CH_2Y$ [Y = F, Cl, Br, I] S_N2 reactions and for the $OH^- + CH_3CH_2Y$ [Y = F, Cl, Br, I] E2 reactions are shown in Figures 4.1 and 4.2, respectively, depicting the benchmark classical (adiabatic) relative energies of the stationary points on the different pathways (back-side attack, front-side attack, double inversion, syn-E2 and anti-E2). The structures of the stationary points along with the relevant bond lengths and angles can be found in Figure 4.3 for $OH^- + CH_3Y$, and in Figures 4.4 and 4.5 for $OH^- + CH_3CH_2Y$. [5, 9]

As the atomic weight of the halogen increases, all reactions become more and more exothermic: The reaction enthalpy of $OH^- + CH_3F$ is deeper by 0.8 kcal mol^{-1}, than that of $OH^- + CH_3CH_2F$, while in the cases of Y = Cl, Br and I, the $OH^- + CH_3CH_2Y$ S_N2 reactions are more exothermic [with reaction enthalpies of −50.4 (Cl), −58.5 (Br) and −66.0 (I) kcal mol^{-1}] than the S_N2 reactions of $OH^- + CH_3Y$ [−49.1 (Cl), −56.6 (Br) and 62.7 (I) kcal mol^{-1}]. The E2 pathways of $OH^- + CH_3CH_2Y$ are always less exothermic (−7.4, −40.8, −48.8 and −56.3 kcal mol^{-1}, for Y = F, Cl, Br and I, in order) than the corresponding S_N2 routes (−17.0, −50.4, −58.5 and −66.0 kcal mol^{-1}, respectively). The global minimum of each pathway is located in the exit channel (PostHMIN, $PostHMIN_{ethyl}$, anti-E2 PostMIN and syn-E2 PostMIN1). Note that in the cases of the $OH^- + CH_3CH_2Y$ S_N2 and syn-E2 routes, additional product-like minima can be determined: $PostMIN_{ethyl}$ and syn-E2 PostMIN2, which are above the corresponding global minimum by 18.9 (F), 8.8 (Cl), 7.3 (Br) and 5.8 (I) kcal mol^{-1} and by 0.2 (F), 0.2 (Cl), 0.2 (Br) and 0.3 (I) kcal mol^{-1}, respectively, without ZPE corrections. However, including ZPE, the global minimum is syn-E2 PostMIN2 for Y = Br. It should be also

noted that, in the exit channel of $OH^- + CH_3F$, a distinct H-bonded $F^-\cdots HCH_2OH$ minimum is positioned above PostHMIN by an energy of~21 kcal mol^{-1}.

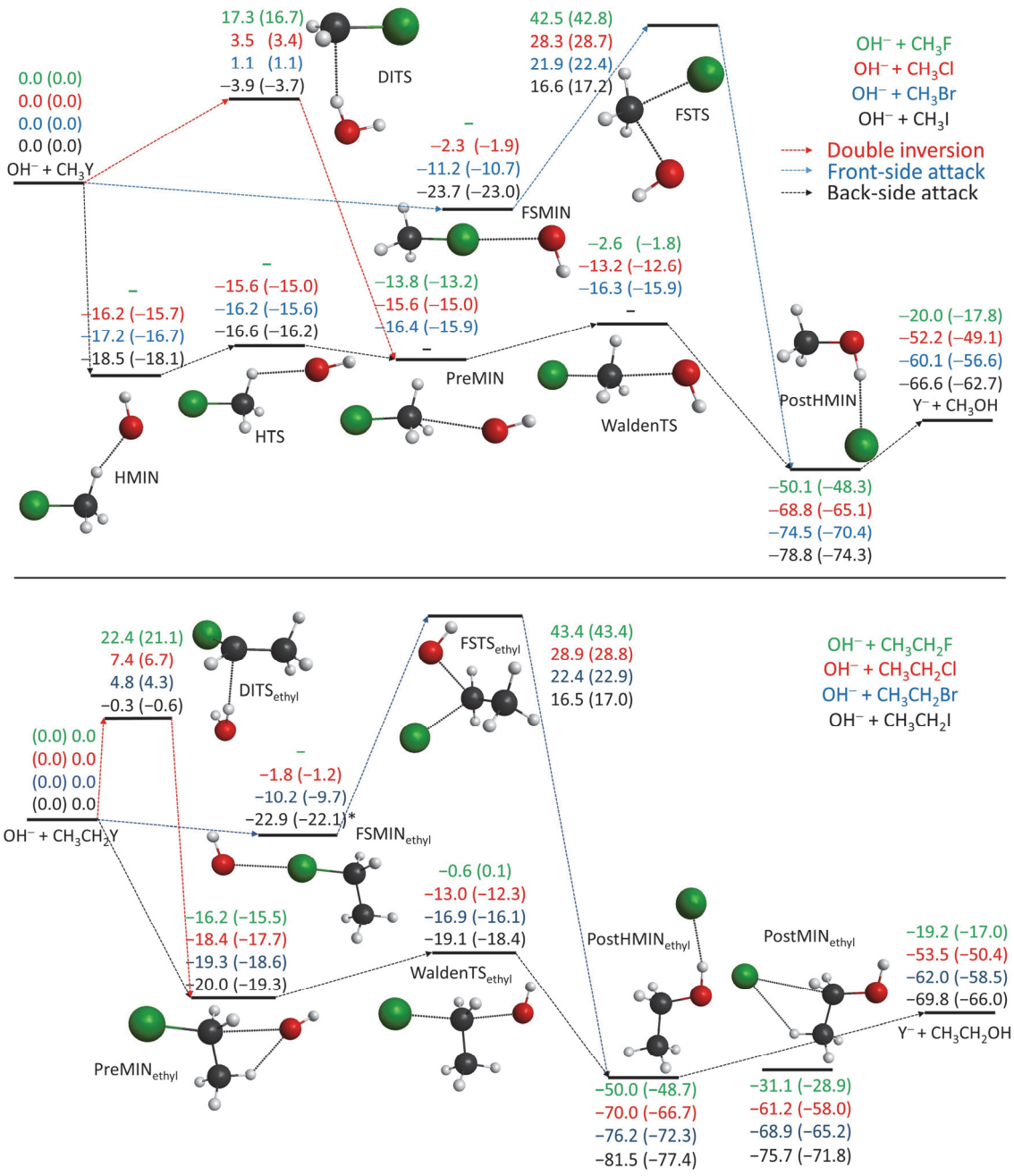

Figure 4.1 The schematic representation of the potential energy surfaces of the $OH^- + CH_3Y/CH_3CH_2Y$ [Y = F, Cl, Br, I] S_N2 reactions presenting the benchmark classical (adiabatic) relative energies (kcal mol^{-1}) of the stationary points obtained from Eq. (4.5)/Eq. (4.1) along the possible pathways. Results denoted by * correspond to the CCSD(T)-F12b/aug-cc-pVDZ geometries. (Taken from ref. [5, 9].)

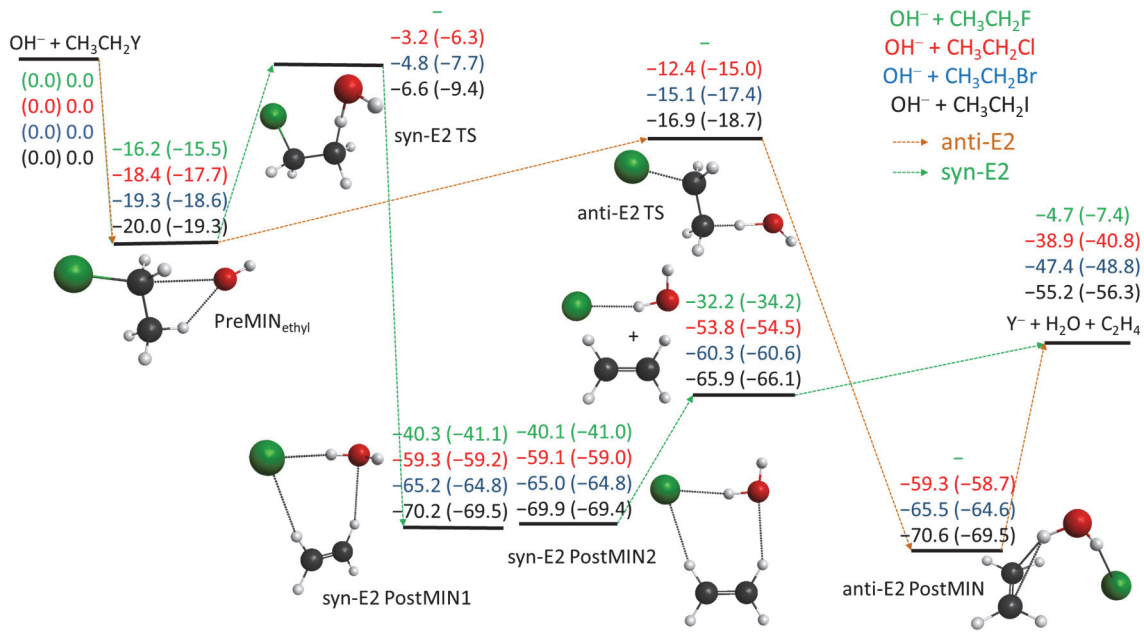

Figure 4.2 The schematic representation of the potential energy surfaces of the $OH^- + CH_3CH_2Y$ [Y = F, Cl, Br, I] anti/syn-E2 reactions presenting the benchmark classical (adiabatic) relative energies (kcal mol^{-1}) of the stationary points obtained from Eq. (4.1). (Taken from ref. [5].)

For $OH^- + CH_3Y$, the back-side attack Walden-inversion is barrierless (each stationary point is below the reactant asymptote), and in cases of Y = Cl and Br, the reaction occurs *via* the HMIN → HTS → PreMIN → WaldenTS → PostHMIN pathway, while for Y = F, the pre-reaction H-bonded minimum (HMIN) and transition state (HTS) cannot be found. In addition, for the $OH^- + CH_3I$ reaction, the traditional PreMIN and WaldenTS does not exist. The classical barrier heights of WaldenTS increase from Y = Br (0.1 kcal mol^{-1}) to F (11.2 kcal mol^{-1}), and the classical barrier heights of HTS increase from Y = Cl (0.6 kcal mol^{-1}) to I (1.9 kcal mol^{-1}). At PostHMIN, the largest D_e (D_0) dissociation energy of the leaving Y^- occurs for Y = F with a value of 30.1 (30.5) kcal mol^{-1}. Note that, in case of $OH^- + CH_3I$, the front-side complex (FSMIN) is below HMIN by 5.2 (4.9) kcal mol^{-1} suggesting a probable front-side complex formation in the entrance channel. For all reactions, the transition states of double inversion (DITS) and front-side attack (FSTS) are found, and DITS is always below FSTS by 25.2 (26.1), 24.8 (25.3), 20.8 (21.3), 20.5 (20.9) kcal mol^{-1} resulting a notably submerged DITS for Y = I with relative energy of −3.9 (−3.7) kcal mol^{-1}.

For $OH^- + CH_3CH_2Y$, the back-side attack Walden inversion is also below the asymptote of the reactants, except for Y = F, where a barrier height of 0.1 kcal mol^{-1} is revealed, if the ZPE effect is considered. In contrast to $OH^- + CH_3I$, Walden-inversion can go through the usual $PreMIN_{ethyl} \rightarrow WaldenTS_{ethyl} \rightarrow PostMIN_{ethyl}/PostHMIN_{ethyl}$ pathway, and the H-bonded reactant-like minimum and transition state cannot be located in the entrance channel. Apart from these, many similarities can be observed with the reactions of methyl halides. The tendencies of D_e (D_0) of the leaving Y^- at $PostHMIN_{ethyl}$ and $PostMIN_{ethyl}$ follow the same trend as for the PostHMIN: As the atomic number of the Y increases, D_e (D_0) decreases. For Y = F, $FSMIN_{ethyl}$ cannot be found; for Y = I, $FSMIN_{ethyl}$ is below $PreMIN_{ethyl}$ by 2.9 (2.8) kcal mol^{-1}. The barrier of double inversion is lower than that of front-side attack by 21.0 (22.3), 21.5 (22.1), 17.6 (18.6),16.8 (17.6) kcal mol^{-1}, for Y = F, Cl, Br and I, respectively. For Y = F, syn-E2 TS and anti-E2 TS cannot be identified, and anti-E2 TS is below syn-E2 TS by 9.2 (Cl), 10.3 (Br) and 10.3 (I) kcal mol^{-1}. It should be noted that with ZPE corrections, $WaldenTS_{ethyl}$ is above anti-E2 TS by 2.7 (Cl), 1.3 (Br) and 0.3 (I) kcal mol^{-1}, signifying that while the S_N2 back-side attack mechanism is thermodynamically more favoured, the pathway of anti-E2 is kinetically more preferred.

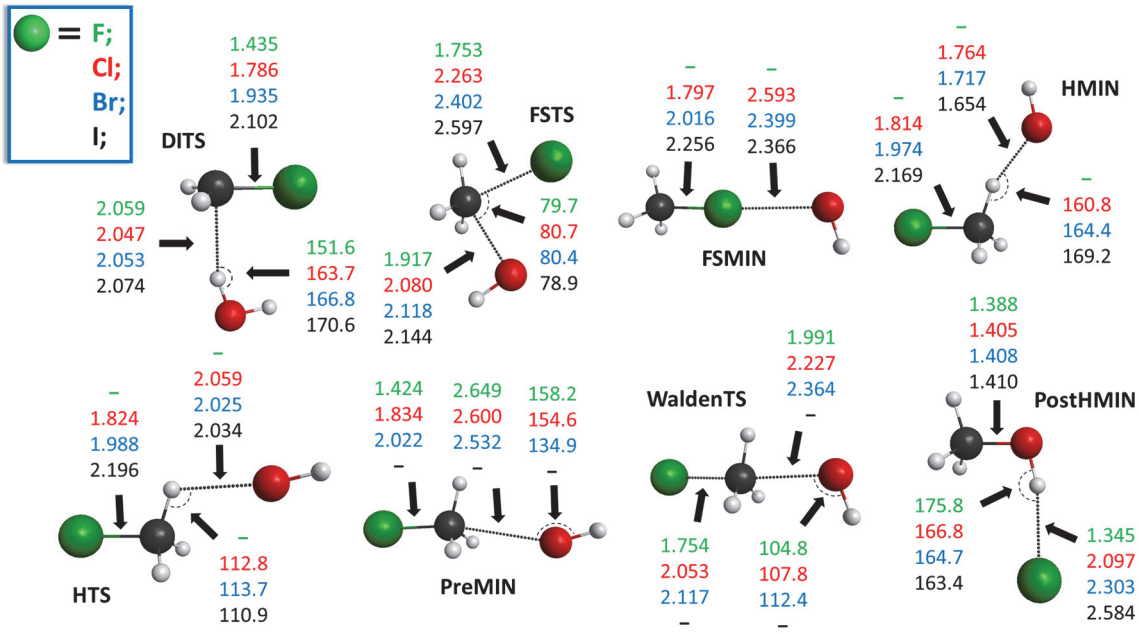

Figure 4.3 The most relevant bond lengths (Å) and angles (°) of the stationary points determined at the CCSD(T)-F12b/aug-cc-pVTZ level of theory corresponding to the $OH^- + CH_3Y$ [Y = F, Cl, Br, I] S_N2 reactions. (Taken from ref. [9].)

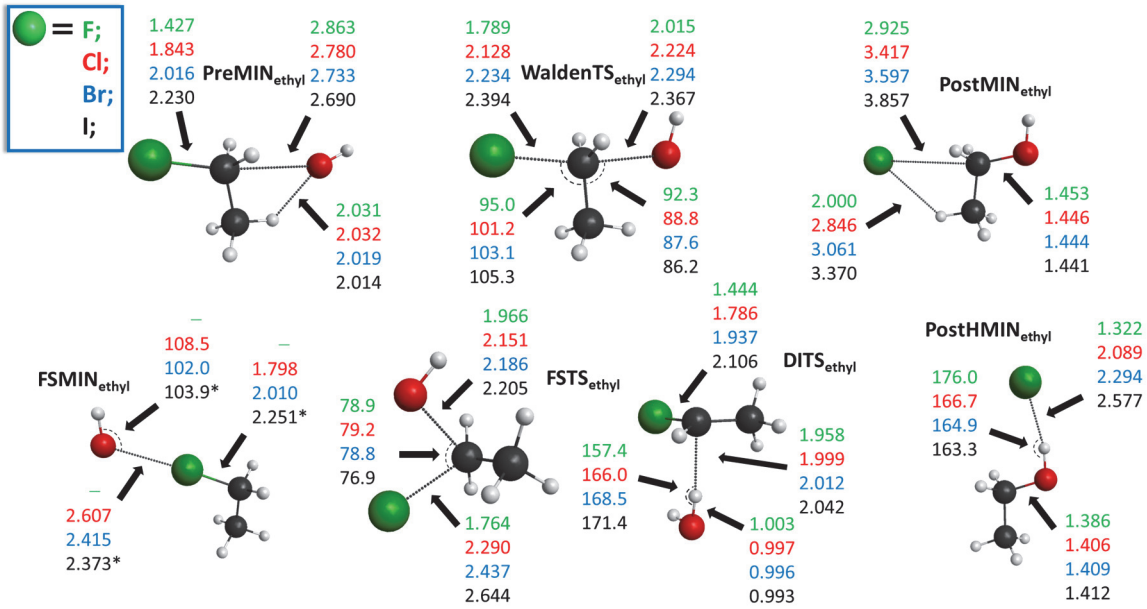

Figure 4.4 The most relevant bond lengths (Å) and angles (°) of the stationary points determined at the CCSD(T)-F12b/aug-cc-pVTZ level of theory corresponding to the $OH^- + CH_3CH_2Y$ [Y = F, Cl, Br, I] S_N2 reactions. Results denoted by * correspond to the CCSD(T)-F12b/aug-cc-pVDZ geometries. (Taken from ref. [5].)

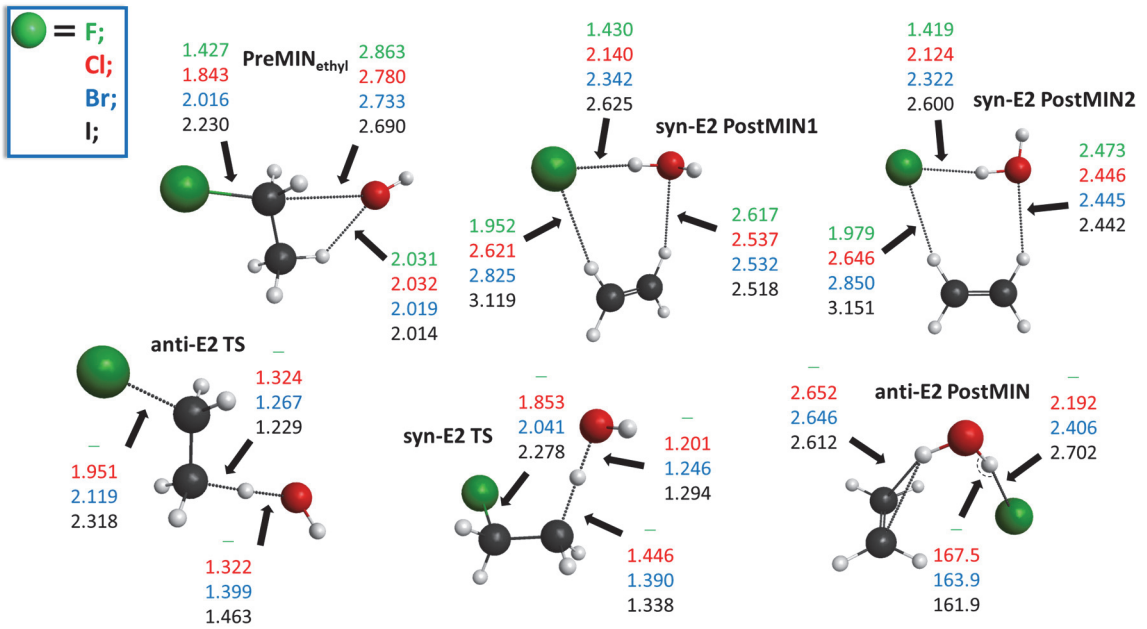

Figure 4.5 The most relevant bond lengths (Å) and angles (°) of the stationary points determined at the CCSD(T)-F12b/aug-cc-pVTZ level of theory corresponding to the $OH^- + CH_3CH_2Y$ [Y = F, Cl, Br, I] E2 reactions. (Taken from ref. [5].)

Beside the energetics, we discuss the structural features of the stationary points as well, which also give a deeper insight into the dynamical profile of the title reactions. Regarding FSMIN of the $OH^- + CH_3Y$ S_N2 reactions, the C···Y···O is almost collinear, and as the Y···O distance decreases (2.593, 2.399, and 2.366 Å for Y = Cl, Br, and I, respectively), the stability of the complex increases (Figure 4.3). While for PostHMIN, with decreasing dissociation energy, the bond length of H···Y increases (1.345, 2.097, 2.303, and 2.584 Å for Y = F, Cl, Br, and I, respectively). In all cases, similar leaving-group dependence can be identified, except for HTS, DITS and PostHMIN, in which the corresponding O···H, C···H and C···O distances, in order, remain almost the same. In some instances, at HTS [Y = Br and I] and FSTS [Y = F], no symmetry plane can be found as seen in Figure 4.6, whereas all the other structures belong to the C_s point-group. In case of the reactions of ethyl halides (Figures 4.4 and 4.5), $PreMIN_{ethyl}$, $WaldenTS_{ethyl}$, $PostMIN_{ethyl}$, $PostHMIN_{ethyl}$ have C_s symmetry, in case of $FSMIN_{ethyl}$ for Y = Cl, a symmetry plane can be detected, however for Y = Br and I, due to the rotation of the OH group, no symmetry is identified. The structures of syn-E2 PostMIN2 complexes have C_s symmetry, whilst anti-E2 TS, syn-E2 TS, syn-E2 PostMIN1 and anti-E2 PostMIN have C_1 symmetry.

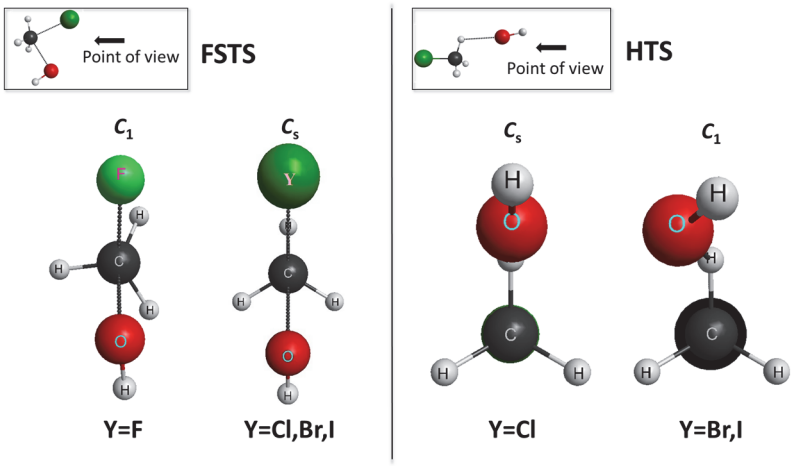

Figure 4.6 The structures of the FSTS and HTS from a point of view representing the change of the point-group symmetries, in case of the $OH^- + CH_3Y$ S_N2 reactions. (Taken from ref. [9].)

In Table 1, the relative CCSD(T)-F12b energies of the stationary points of the $OH^- + CH_3Y$ S_N2 reactions are summarized according to the applied basis sets of aug-cc-pVDZ and aug-cc-pVTZ. The benchmark classical and adiabatic energies relative

to the reactants are also presented in Table 1, together with the ZPE effects and the post-CCSD(T) and core corrections. In case of $OH^- + CH_3I$, the DFT classical energies provided by Xie *et al.* are in accord with our benchmark classical energies:[38] At HMIN (−20.07 kcal mol^{-1}), HTS (−18.73 kcal mol^{-1}), PostHMIN (−80.12 kcal mol^{-1}) and FSMIN (−26.10 kcal mol^{-1}), a difference of 1.58, 2.08, 1.34, and 2.41 kcal mol^{-1} can be observed, respectively. Their DFT S_N2 reaction enthalpy is more exothermic as well, deeper by 2.16 kcal mol^{-1}, however it should be noted that our reaction enthalpies for all the four $OH^- + CH_3Y$ [Y = F, Cl, Br, I] S_N2 reactions (−17.78, −49.08, −56.55 and −62.67 kcal mol^{-1}, in order) are in an excellent agreement with the "experimental" 0 K gas-phase enthalpies of formation data obtained from the Active Thermochemical Tables (ATcT)[141,142] (−17.66 ± 0.07, −49.10 ± 0.07, −56.64 ± 0.08, and −62.91 ± 0.06 kcal mol^{-1}, in the same order). For $OH^- + CH_3F$, the energies of the PreMIN (−13.02 kcal mol^{-1}), WaldenTS (−1.81 kcal mol^{-1}) and PostHMIN (−48.48 kcal mol^{-1}) stationary points, as well as the reaction enthalpies (−17.87 kcal mol^{-1}) determined by Gonzales *et al.*[19] are in accord with our values as well (−13.16, −1.79, −48.31 and −17.78 kcal mol^{-1}, respectively).

The *ab initio* energies of the stationary points of the $OH^- + CH_3CH_2Y$ S_N2 and E2 reactions are presented in Table 2. The reaction enthalpies are determined for several other pathways: H_2O+H_3C–CHY^-, $H^- + H_3C$–CHYOH, $H^- + HOH_2C$–CH_2Y, $OHY^- + CH_3CH_2$, and $HOY + CH_3CH_2^-$, as seen in Table 3. The classical energies of the transition states of Walden inversion assessed by Wu *et al.*[90] are −15.5, −18.5 and −20.7 kcal mol^{-1}, for Y = Cl, Br and I, respectively, which are below by 2.5, 1.6 and 1.6 kcal mol^{-1} compared to our benchmark *ab initio* results. It should be noted that at $FSTS_{ethyl}$, anti-E2 TS, syn-E2 TS and $PostHMIN_{ethyl}$ different conformers were identified by Wu and co-workers emphasizing that a supplementation is needed for both *ab initio* studies. Moreover, the characterization of Wu and co-workers is slightly incomplete, because they did not consider the syn-E2 PostMIN1 and syn-E2 PostMIN2 complexes and $DITS_{ethyl}$. In case of PreMIN, their classical energies are deeper than our benchmark data by 2.0 kcal mol^{-1} for all Y, and the energies of anti-E2 PostMIN (−60.6, −65.2 and −69.3 kcal mol^{-1}, for Y = Cl, Br and I) are in good agreement with our energies (−59.3, −65.5 and −70.6 kcal mol^{-1}, respectively). Concerning the reaction enthalpies, the exothermicity is increasing from Y = F to I, except for the most endothermic reaction ($HOY + CH_3CH_2^-$), where the order is reversed. The most exothermic reaction is $HOH\cdots Y^- + C_2H_4$, although

it can dissociate to the final products of E2 ($Y^- + H_2O + C_2H_4$). For Y = Cl, Br and I, the endothermicity of the reaction enthalpies of $OHY^- + CH_3CH_2$, $H^- + H_3C–CHYOH$, $H^- + HOH_2C–CH_2Y$, $HOY + CH_3CH_2^-$ is increasing, while for Y = F, the channel of $OHY^- + CH_3CH_2$ is above $H^- + H_3C–CHYOH$ and $H^- + HOH_2C–CH_2Y$ by 22.8 and 8.7 kcal mol^{-1}, in order. Same trends can be noticed for the available ATcT reaction enthalpies, except for $H^- + HOH_2C–CH_2Y$, where the corresponding declining tendency of the enthalpies changes at Y = I. Furthermore, in every case, the deviations between our benchmark data and the experimental reaction enthalpies are within chemical accuracy (< 1 kcal mol^{-1}), excluding $H^- + HOH_2C–CH_2Y$, which signifies the uncertainty of the "experimental" data or the *ab initio* calculations. In cases of the $OH^- + CH_3CH_2Y$ [Y = Br and I] S_N2 and E2 channels, between the reaction enthalpies of Wu and co-workers and our benchmark enthalpies, large differences can be found: 2.5 (Cl), 2.9 (Br) and 4.4 (I) kcal mol^{-1} for S_N2 and 2.1 (Cl), 4.6 (Br) and 5.7 (I) kcal mol^{-1} for E2.[90] These deviations underline the importance of the high-level *ab initio* methods, especially if our goal is to achieve accurate relative energies (within chemical accuracy) of a given system. The CCSD(T)-F12b/aug-cc-pVTZ structures of the stationary points are presented in Figure S1 in the Appendix section. It is noteworthy that the geometries of OHY^- products are not evident, in cases of Y = F, Cl and Br, a H···Y hydrogen bond is formed, whereas at Y = I, a O···Y bond is arranged.

Table 1 The obtained *ab initio* energies along with the post-CCSD(T) and core correlation effects (kcal mol^{-1}) of the stationary points relative to the reactants for the $OH^- + CH_3Y$ [Y = F, Cl, Br, I] S_N2 reactions. The results are adopted from ref. [9].*

OH^-+CH_3F	**CCSD(T)-F12b**		**δT**[c]	**δ(Q)**[d]	**Δcore**[e]	**Classical**[f]	**ΔZPE**[g]	**Adiabatic**[h]
	TZ[a]	**QZ**[b]						
PreMIN	–13.87	–13.74	–0.03	0.00	0.01	–13.76	0.60	–13.16
WaldenTS	–2.71	–2.59	–0.10	–0.18	0.27	–2.60	0.81	–1.79
PostHMIN	–50.19	–50.05	0.08	0.08	–0.16	–50.05	1.75	–48.31
FSTS	42.44	42.74	–0.13	–0.43	0.32	42.49	0.36	42.85
DITS	17.23	17.45	–0.04	–0.02	–0.10	17.29	–0.55	16.73
F^-+CH_3OH	–19.82	–19.95	0.01	0.11	–0.15	–19.97	2.19	–17.78
OH^-+CH_3Cl	**TZ**[a]	**QZ**[b]	**δT**[c]	**δ(Q)**[d]	**Δcore**[e]	**Classical**[f]	**ΔZPE**[g]	**Adiabatic**[h]
HMIN	–16.33	–16.20	–0.02	0.01	0.01	–16.20	0.55	–15.66
HTS	–15.64	–15.55	–0.03	–0.01	0.03	–15.56	0.58	–14.98
PreMIN	–15.71	–15.62	–0.04	–0.01	0.05	–15.61	0.61	–15.00
WaldenTS	–13.26	–13.21	–0.11	–0.17	0.28	–13.21	0.62	–12.59
PostHMIN	–68.91	–69.04	0.07	0.21	–0.01	–68.77	3.68	–65.09
FSMIN	–2.38	–2.24	–0.03	–0.09	0.01	–2.35	0.43	–1.92
FSTS	28.64	28.81	–0.19	–0.66	0.35	28.31	0.39	28.70
DITS	3.51	3.60	0.04	0.00	–0.10	3.54	–0.13	3.42
Cl^-+CH_3OH	–52.37	–52.65	0.06	0.26	0.08	–52.25	3.17	–49.08
OH^-+CH_3Br	**TZ**[a]	**QZ**[b]	**δT**[c]	**δ(Q)**[d]	**Δcore**[e]	**Classical**[f]	**ΔZPE**[g]	**Adiabatic**[h]
HMIN	–17.33	–17.17	–0.02	0.01	0.04	–17.15	0.48	–16.68
HTS	–16.28	–16.17	–0.04	–0.01	0.04	–16.18	0.57	–15.60
PreMIN	–16.53	–16.41	–0.05	–0.04	0.08	–16.43	0.50	–15.93
WaldenTS	–16.33	–16.24	–0.09	–0.14	0.19	–16.28	0.39	–15.89
PostHMIN	–74.75	–74.95	0.07	0.24	0.10	–74.54	4.12	–70.42
FSMIN	–11.33	–11.21	0.02	–0.23	0.18	–11.24	0.54	–10.70
FSTS	22.30	22.44	–0.16	–0.71	0.37	21.93	0.44	22.36
DITS	0.89	1.01	0.05	–0.01	0.06	1.11	0.01	1.11
Br^-+CH_3OH	–60.41	–60.80	0.07	0.29	0.32	–60.13	3.58	–56.55
OH^-+CH_3I	**TZ**[a]	**QZ**[b]	**δT**[c]	**δ(Q)**[d]	**Δcore**[e]	**Classical**[f]	**ΔZPE**[g]	**Adiabatic**[h]
HMIN	–18.64	–18.48	–0.02	0.00	0.02	–18.49	0.42	–18.07
HTS	–16.69	–16.57	–0.04	–0.04	0.01	–16.65	0.50	–16.15
PostHMIN	–79.08	–79.43	0.09	0.27	0.29	–78.78	4.49	–74.29
FSMIN	–24.10	–24.05	0.07	–0.23	0.51	–23.69	0.68	–23.01
FSTS	17.03	17.10	–0.11	–0.79	0.42	16.62	0.58	17.20
DITS	–4.13	–4.05	0.07	–0.01	0.15	–3.85	0.18	–3.67
I^-+CH_3OH	–67.08	–67.71	0.08	0.31	0.67	–66.64	3.98	–62.67

[a] CCSD(T)-F12b/aug-cc-pVTZ. [b] Eq. (4.1). [c] Eq. (4.2). [d] Eq. (4.3). [e] Eq. (4.4). [f] Eq. (4.5)
[g] ΔZPE(CCSD(T)-F12b/aug-cc-pVTZ). [h] Eq. (4.5) + ΔZPE.

* The structures and harmonic vibrational frequencies of all the stationary points are given in the Supporting Information of ref. [9].

Table 2 Relative classical and adiabatic *ab initio* energies (kcal mol^{-1}) of the stationary points for the $OH^- + CH_3CH_2Y$ [Y = F, Cl, Br, I] S_N2/E2 reactions, adopted from ref. [5].

$OH^-+CH_3CH_2F$	**CCSD(T)-F12b**			**ΔZPE[d]**	**Adiabatic[e]**
	DZ[a]	**TZ[b]**	**QZ[c]**		
PreMIN	−16.54	−16.41	−16.21	0.73	−15.48
syn-E2 PostMIN1	−40.60	−40.40	−40.29	−0.79	−41.09
syn-E2 PostMIN2	−40.29	−40.14	−40.08	−0.96	−41.04
$PostMIN_{ethyl}$	−31.39	−31.21	−31.09	2.24	−28.86
$PostHMIN_{ethyl}$	−50.31	−50.19	−50.02	1.34	−48.68
WaldenTS	−0.66	-0.83	−0.59	0.64	0.05
FSTS	43.05	42.93	43.41	−0.05	43.36
DITS	21.93	22.18	22.43	−1.30	21.13
$OH^-+ CH_3CH_2Cl$	**DZ[a]**	**TZ[b]**	**QZ[c]**	**ΔZPE[d]**	**Adiabatic[e]**
PreMIN	−18.59	−18.54	−18.38	0.68	−17.69
anti-E2 PostMIN	−59.16	−59.14	−59.31	0.57	−58.74
syn-E2 PostMIN1	−59.10	−59.13	−59.32	0.14	−59.17
syn-E2 PostMIN2	−58.79	−58.84	−59.06	0.03	−59.02
$PostMIN_{ethyl}$	−60.93	−61.01	−61.18	3.14	−58.04
$PostHMIN_{ethyl}$	−69.73	−69.94	−70.02	3.35	−66.68
FSMIN	−2.58	−1.96	−1.79	0.56	−1.23
anti-E2 TS	−12.58	−12.55	−12.36	−2.68	−15.04
syn-E2 TS	−3.71	−3.45	−3.17	−3.08	−6.25
WaldenTS	−12.84	−13.11	−12.98	0.71	−12.28
FSTS	28.64	28.61	28.87	−0.08	28.79
DITS	6.96	7.24	7.40	−0.68	6.71
$OH^-+ CH_3CH_2Br$	**DZ[a]**	**TZ[b]**	**QZ[c]**	**ΔZPE[d]**	**Adiabatic[e]**
PreMIN	−19.61	−19.49	−19.31	0.68	−18.64
anti-E2 PostMIN	−65.45	−65.24	−65.50	0.88	−64.62
syn-E2 PostMIN1	−65.10	−64.96	−65.23	0.47	−64.76
syn-E2 PostMIN2	−64.78	−64.66	−64.95	0.19	−64.77
$PostMIN_{ethyl}$	−68.75	−68.59	−68.89	3.66	−65.22
$PostHMIN_{ethyl}$	−76.15	−76.07	−76.24	3.98	−72.27
FSMIN	−10.47	−10.38	−10.23	0.55	−9.68
anti-E2 TS	−15.54	−15.32	−15.14	−2.22	−17.36
syn-E2 TS	−5.45	−5.09	−4.83	−2.90	−7.73
WaldenTS	−16.89	−17.00	−16.86	0.80	−16.05
FSTS	22.35	22.18	22.40	0.55	22.94
DITS	4.30	4.60	4.79	−0.52	4.27
$OH^-+ CH_3CH_2I$	**DZ[a]**	**TZ[b]**	**QZ[c]**	**ΔZPE[d]**	**Adiabatic[e]**
PreMIN	−20.33	−20.21	−20.04	0.78	−19.26
anti-E2 PostMIN	−70.33	−70.19	−70.65	1.10	−69.55
syn-E2 PostMIN1	−69.79	−69.71	−70.18	0.69	−69.49
syn-E2 PostMIN2	−69.45	−69.40	−69.88	0.45	−69.43
$PostMIN_{ethyl}$	−75.19	−75.20	−75.74	3.97	−71.77
$PostHMIN_{ethyl}$	−81.20	−81.19	−81.54	4.11	−77.43
FSMIN	−22.99	–[f]	−22.87[g]	0.81	−22.06
anti-E2 TS	−17.25	−17.01	−16.88	−1.82	−18.69
syn-E2 TS	−7.11	−6.78	−6.57	−2.81	−9.38
WaldenTS	−19.19	−19.21	−19.09	0.67	−18.41
FSTS	16.57	16.38	16.52	0.45	16.97
DITS	−0.54	−0.41	−0.28	−0.32	−0.60

[a] CCSD(T)-F12b/aug-cc-pVDZ. [b] CCSD(T)-F12b/aug-cc-pVTZ. [c] Eq. (4.1). [d] ΔZPE(CCSD(T)-F12b/aug-cc-pVDZ). [e] Eq. (4.1). [f] CCSD(T)-F12b/aug-cc-pVTZ geometry optimization does not converge, hence the CCSD(T)-F12b/aug-cc-pVQZ energy is obtained at the CCSD(T)-F12b/aug-cc-pVDZ structure.

Table 3 Experimental and our benchmark *ab initio* 0 K reaction enthalpies (kcal mol^{-1}) of various product channels for the $OH^- + CH_3CH_2Y$ [Y = F, Cl, Br, I] reactions. The results are taken from ref. [5]

$OH^-+CH_3CH_2F$	**CCSD(T)-F12b**			**ΔZPE[d]**	**Adiabatic[e]**	**Exp[f]**
	DZ[a]	**TZ[b]**	**QZ[c]**			
$F^- + C_2H_5OH$	−19.00	−19.07	−19.22	2.19	−17.03	−17.19 ± 0.10
$HOH\cdots F^- + C_2H_4$	−31.81	−32.02	−32.20	−2.00	−34.19	–
$F^- + H_2O + C_2H_4$	−4.04	−4.29	−4.67	−2.74	−7.40	−7.81 ± 0.09
$H_2O + H_3C–CHF^-$	21.94	22.13	22.22	−2.37	19.85	–
$H^- + H_3C–CHFOH$	20.17	21.41	21.83	−2.13	19.71	–
$H^- + HOH_2C–CH_2F$	34.24	35.53	35.93	−2.13	33.80	31.98 ± 0.25
$OHF^- + CH_3CH_2$	47.08	46.89	46.98	−4.48	42.50	–
$HOF + CH_3CH_2^-$	114.54	114.39	114.51	−3.18	111.33	111.66 ± 0.23
$OH^-+CH_3CH_2Cl$	**DZ[a]**	**TZ[b]**	**QZ[c]**	**ΔZPE[d]**	**Adiabatic[e]**	**Exp[f]**
$Cl^- + C_2H_5OH$	−52.84	−53.20	−53.46	3.03	−50.43	−50.26 ± 0.08
$HOH\cdots Cl^- + C_2H_4$	−52.96	−53.47	−53.83	−0.69	−54.52	–
$Cl^- + H_2O + C_2H_4$	−37.89	−38.42	−38.91	−1.89	−40.80	−40.88 ± 0.07
$H_2O + H_3C–CHCl^-$	9.49	9.42	9.43	−1.99	7.44	–
$H^- + H_3C–CHClOH$	26.19	27.55	28.00	−2.43	25.56	–
$H^- + HOH_2C–CH_2Cl$	33.10	34.46	34.86	−2.19	32.68	30.93 ± 0.15
$OHCl^- + CH_3CH_2$	28.58	28.13	28.07	−3.23	24.84	–
$HOCl + CH_3CH_2^-$	77.47	77.95	78.12	−2.73	75.39	75.86 ± 0.22
$OH^-+CH_3CH_2Br$	**DZ[a]**	**TZ[b]**	**QZ[c]**	**ΔZPE[d]**	**Adiabatic[e]**	**Exp[f]**
$Br^- + C_2H_5OH$	−61.59	−61.57	−61.97	3.51	−58.46	−58.19 ± 0.08
$HOH\cdots Br^- + C_2H_4$	−59.67	−59.87	−60.33	−0.30	−60.63	–
$Br^- + H_2O + C_2H_4$	−46.63	−46.80	−47.42	−1.42	−48.83	−48.81 ± 0.07
$H_2O + H_3C–CHBr^-$	5.16	5.15	5.15	−1.66	3.49	–
$H^- + H_3C–CHBrOH$	26.98	28.40	28.83	−2.41	26.42	–
$H^- + HOH_2C–CH_2Br$	32.98	34.31	34.71	−2.16	32.55	30.43 ± 0.14
$OHBr^- + CH_3CH_2$	22.38	22.24	–	−2.85	19.38[h]	–
$HOBr + CH_3CH_2^-$	69.22	69.30	69.41	−2.51	66.89	67.91 ± 0.25
$OH^-+CH_3CH_2I$	**DZ[a]**	**TZ[b]**	**QZ[c]**	**ΔZPE[d]**	**Adiabatic[e]**	**Exp[f]**
$I^- + C_2H_5OH$	−68.93	−69.08	−69.75	3.79	−65.96	−65.71 ± 0.13
$HOH\cdots I^- + C_2H_4$	−64.97	−65.27	−65.94	−0.13	−66.07	–
$I^- + H_2O + C_2H_4$	−53.97	−54.31	−55.20	−1.14	−56.34	−56.33 ± 0.12
$H_2O + H_3C–CHI^-$	0.64	0.51	0.42	−1.57	−1.14	–
$H^- + H_3C–CHIOH$	28.63	30.11	30.55	−2.31	28.25	–
$H^- + HOH_2C–CH_2I$	32.55	33.91	34.32	−2.22	32.10	33.86 ± 0.61
$OHI^- + CH_3CH_2$	16.58	16.34	16.16	−2.52	13.64	–
$HOI + CH_3CH_2^-$	57.12	56.76	56.82	−2.42	54.40	55.32 ± 0.78

[a] CCSD(T)-F12b/aug-cc-pVDZ. [b] CCSD(T)-F12b/aug-cc-pVTZ. [c] Eq. (4.1). [d] ΔZPE(CCSD(T)-F12b/aug-cc-pVDZ). [e] Eq. (4.1). [g] Obtained from the 1.122p version of the Active Thermochemical Tables (ATcT).[141,142] The uncertainties are derived using the Gaussian error-propagation law on the uncertainties of each 0 K enthalpy of formation provided in ATcT. [h] TZ + ΔZPE, because ROHF/QZ does not converge.

In Figures 4.7 and 4.8, the basis-set convergences of the utilized explicitly-correlated CCSD(T)-F12b method are shown for the $OH^- + CH_3Y$ S_N2 and $OH^- + CH_3CH_2Y$ S_N2 and E2 reactions, as well as, for the reaction enthalpies of the investigated pathways of $OH^- + CH_3CH_2Y$. The post-CCSD(T) and the core correlations, acquired from Eq. (4.2)–(4.4), are depicted for the stationary points of the $OH^- + CH_3Y$ [Y = F, Cl, Br, I] S_N2 reactions in Figure 4.9.

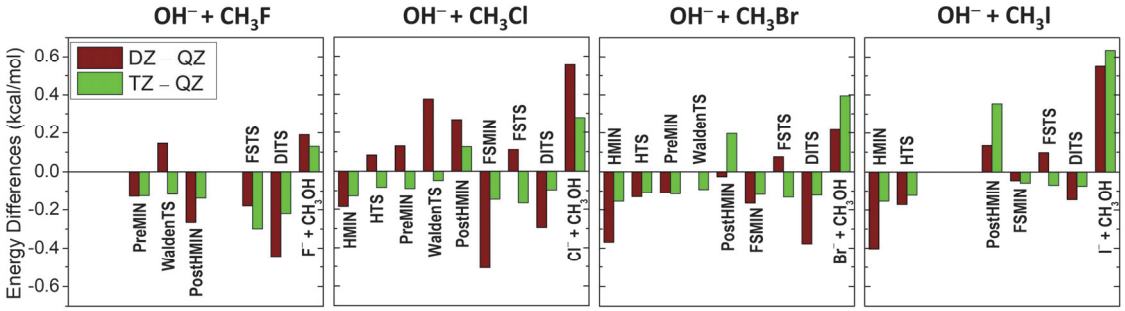

Figure 4.7 The basis-set convergence of the CCSD(T)-F12b method for the stationary points of the $OH^- + CH_3Y$ [Y = F, Cl, Br, I] S_N2 reactions. (Taken from ref. [9].)

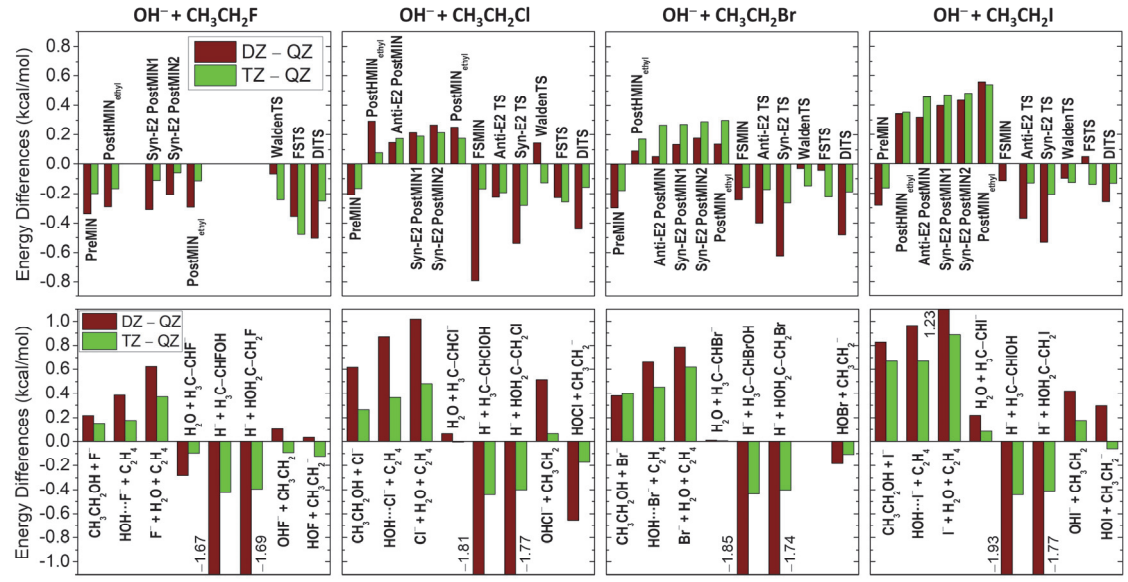

Figure 4.8 The basis-set convergence of the CCSD(T)-F12b method for the stationary points of the $OH^- + CH_3CH_2Y$ [Y = F, Cl, Br, I] S_N2 and E2 reactions, as well as, for several other reaction products. (Taken from ref. [5].)

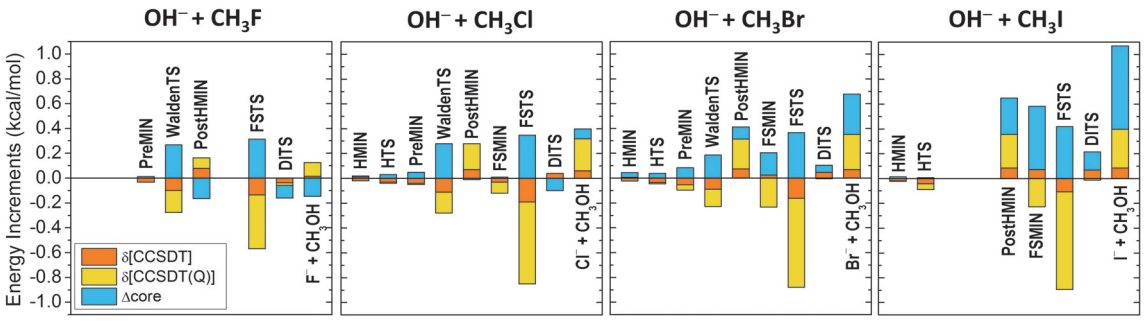

Figure 4.9 Post-CCSD(T) (δ[CCSDT] and δ[CCSDT(Q)]) and core correlation effects (Δcore) obtained from Eq. (4.2)–(4.4) for the stationary points of the $OH^- + CH_3Y$ [Y = F, Cl, Br, I] S_N2 reactions. (Taken from ref. [9, 10].)

As it can be expected, the modern CCSD(T)-F12b method shows a fast basis-set convergence: Concerning $OH^- + CH_3Y$, the corresponding DZ – QZ (CCSD(T)-F12b/aug-cc-pVDZ – CCSD(T)-F12b/aug-cc-pVQZ) deviations are within ± 0.45 kcal mol^{-1}, except FSMIN at Y = Cl (–0.51 kcal mol^{-1}) and $Y^- + CH_3OH$ at Y = Cl and I (0.56 and 0.55 kcal mol^{-1}). The TZ – QZ (CCSD(T)-F12b/aug-cc-pVTZ – CCSD(T)-F12b/aug-cc-pVQZ) differences are between ± 0.30 kcal mol^{-1}, not including the $Br^-/I^- + CH_3OH$ reaction energies (0.40/0.63 kcal mol^{-1}). In respect of the $OH^- + CH_3CH_2Y$ S_N2 reactions, slightly larger differences can be seen: DZ – QZ deviations are in the range of ± 0.62 kcal mol^{-1}, excluding FSMIN at Y = Cl (–0.79 kcal mol^{-1}) and the $CH_3CH_2OH + I^-$ product (0.83 kcal mol^{-1}), while TZ – QZ is within ± 0.50 kcal mol^{-1} at each stationary point, except $PostMIN_{ethyl}$ at Y = I (0.54 kcal mol^{-1}). In the matter of $OH^- + CH_3CH_2Y$ E2 reactions, the differences for the stationary points are smaller, howbeit, as regard to the reaction energies of E2, more significant basis-set dependence can be obtained with DZ – QZ of 0.62 (F), 1.02 (Cl), 0.79 (Br), 1.23 (I) kcal mol^{-1}, and with TZ – QZ of 0.37 (F), 0.48 (Cl), 0.62 (Br) and 0.89 (I) kcal mol^{-1}. On the top of that, in cases of $H^- + H_3C–CHYOH$ and $H^- + HOH_2C–CH_2Y$, substantial DZ – QZ values eventuate with a nearly 2 kcal mol^{-1} of deviation for $H^- + H_3C–CHIOH$.

Regarding on a previous study of $Cl^- + CH_3I$,[143] the post-CCSD(T) and core corrections regularly cancel each other. This is also the case for the present $OH^- + CH_3Y$ reactions, barring the $Y^- + CH_3OH$ [Y = Cl, Br, I] products, where all the three effects are positive with a collective energy of 0.40, 068 and 1.07 kcal mol^{-1}, as seen in Figure 4.9. The largest post-CCSD(T) corrections are observed for FSTS (–0.43 (F), –0.66 (Cl),

–0.71 (Br) and –0.79 (I) kcal mol^{-1}), otherwise these values are usually small (between ± 0.30 kcal mol^{-1}). Moreover, for the majority of the stationary points, these post-CCSD(T) corrections are larger than the core correlation effects. These findings underline the fact that these energy corrections should not be neglected for energy determination if sub-chemical accuracy must be achieved.

The ZPE effects of the stationary points of $OH^- + CH_3Y$ are positive, except for FSTS [Y = F, Cl], and generally less than 0.80 kcal mol^{-1}. For PostHMIN and S_N2 products, the ZPE values are more significant: The corrections are within 1.7–4.5 kcal mol^{-1} for PostHMIN and 2.1–4.0 kcal mol^{-1} for the corresponding products. In case of $OH^- + CH_3CH_2Y$, almost every transition state has negative ZPE effect, excluding WaldenTS and FSTS [Y = Br and I]. The most notable ZPE contributions occur at the complexes of the S_N2 exit channel ($PostMIN_{ethyl}$ and $PostHMIN_{ethyl}$) and at the products of the possible reaction channels. In each reaction, the $C_2H_5OH + Y^-$ S_N2 products have positive ZPEs, whilst for the other products negative ZPEs can be found.

4.1.2 The $CN^- + CH_3Y$ [Y = F, Cl, Br, I] S_N2 reactions

Beside OH^-, four other S_N2 reactions of methyl halides and two/three-atomic nucleophiles (CN^-, SH^-, NH_2^- and PH_2^-) are investigated, as well. [3, 8] As it is known, CN^- is an ambident nucleophile, therefore two separate S_N2 pathways must be considered for the reaction between CN^- and CH_3Y, leading to $Y^- + CH_3CN$ and $Y^- + CH_3NC$. The representation of the two PESs of the $NC^-/CN^- + CH_3Y$ [Y = F, Cl, Br, I] reactions featuring the relative classical (adiabatic) energies of the possible stationary points for each path is shown in Figure 4.10. Each stationary point of the C–C-bond-forming S_N2 reaction is submerged compared to the C–N case, signifying that the S_N2 resulting C–C bond is kinetically more preferred. Regarding the reaction enthalpies of the S_N2 reactions, enormous differences of ~24–25 kcal mol^{-1} can be seen. In the entrance channel, the energies of the two different HMIN2 complexes are similar, a maximum difference of 0.1 kcal mol^{-1} occurs. For the reactions of $NC^- + CH_3Br/CH_3I$, additional H-bonded HMIN1 (Br and I) and HTS2 (I) are located in the reactant channel. Note, the structure of that latter H-bonded transition state (HTS2) is dissimilar to HTS of the $OH^- + CH_3Y$ systems. In case of C–C-bond-forming S_N2, the barrier heights of the back-side attack Walden inversion are lowered by 5.8 (5.8), 4.2 (4.3), 4.0 (4.0) and 3.9 (3.9) kcal mol^{-1} for Y = F,

Cl, Br and I, respectively. Analogously, the barriers of front-side attack and double inversion of the C–C-bond-forming S_N2 reactions are submerged by an energy of more than ~5.0 and ~6.5 kcal mol^{-1} in each case.

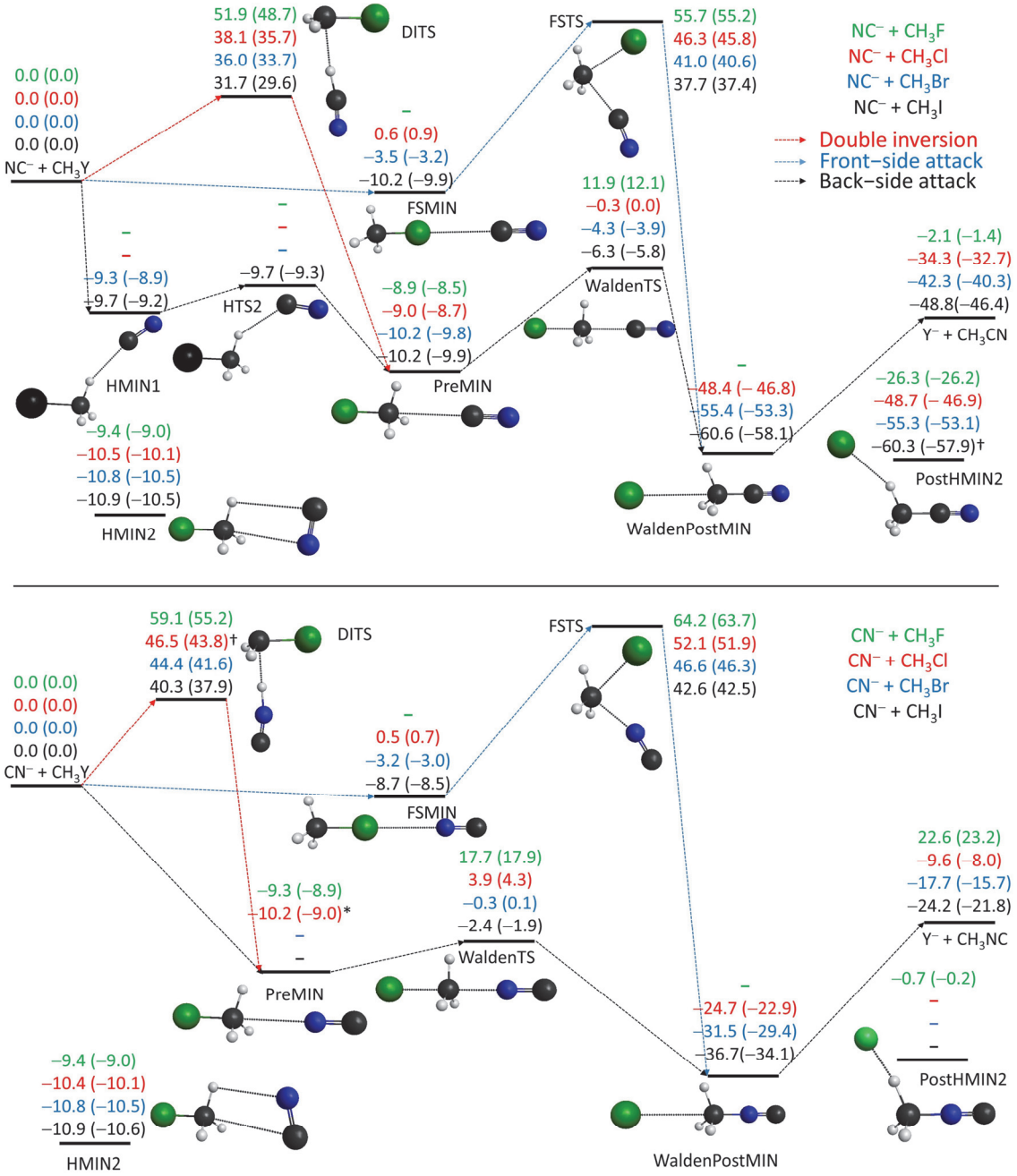

Figure 4.10 The schematic potential energy diagrams of the NC^-/CN^- + CH_3Y [Y = F, Cl, Br, I] S_N2 reactions showing the benchmark classical (adiabatic) relative energies (kcal mol^{-1}) of the stationary points of the possible pathways obtained from Eq. (4.7) and Eq. (4.8). Results denoted by † and * correspond to the MP2/aug-cc-pVDZ and CCSD(T)-F12b/aug-cc-pVDZ geometries. (Taken from ref. [3, 8].)

For the NC^-/CN^- + CH_3F S_N2 reactions, FSMIN and WaldenPostMIN cannot be determined. NC^- + CH_3Br/CH_3I reactions have a more stable front-side complex, as their FSMIN complexes are lowered by 0.3 (0.2) and 1.5 (1.4) kcal mol^{-1}, in order, compared to the corresponding C–N-bond-forming S_N2 reaction. Regarding CN^- + CH_3Y, PostHMIN2 is only found along the route of Y = F. In the matter of both S_N2 reaction-types, the global minimum is located in the exit channel (WaldenPostMIN and PostHMIN2) and ~24 kcal mol^{-1} energy deviations can be recognized between the two types of WaldenPostMINs for each reaction. It is noteworthy that since the cyanide ion has no hydrogen, PostHMIN1 structure does not exists. The benchmark CCSD(T)-F12b/aug-cc-pVTZ structures of the stationary points of the NC^-/CN^- + CH_3Y reactions are shown in Figures 4.11 and 4.12.

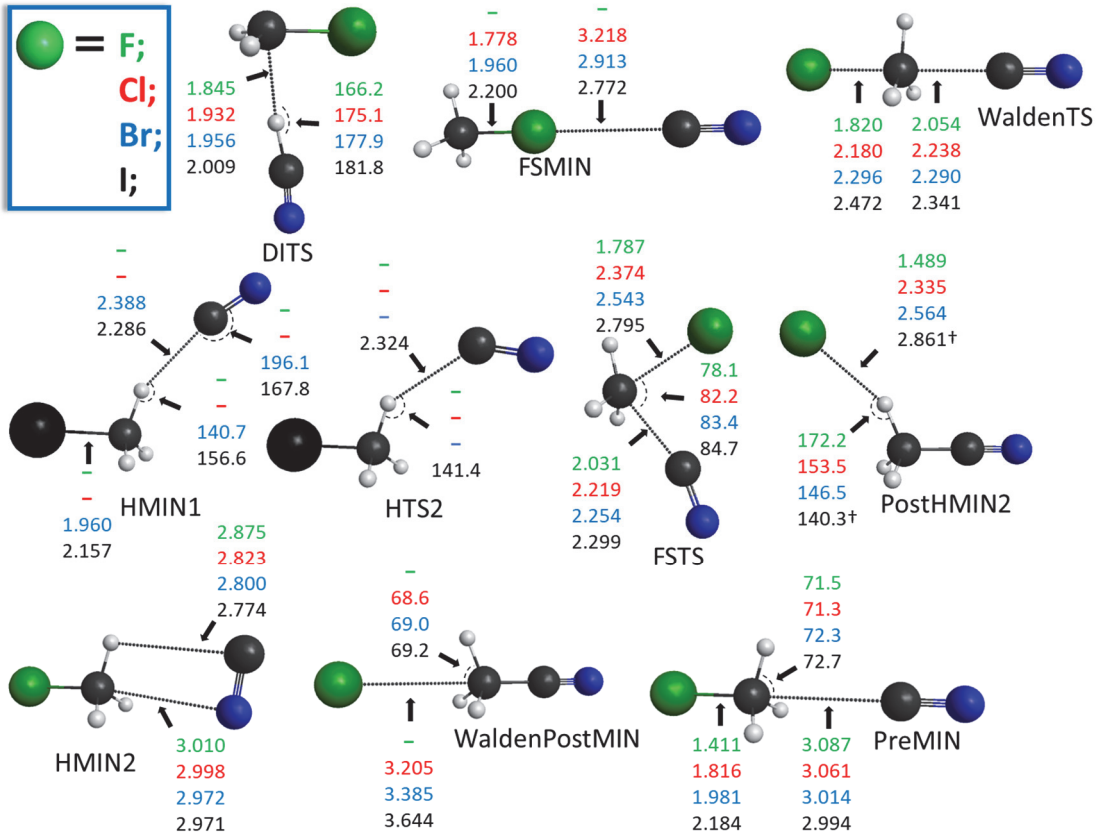

Figure 4.11 The most relevant bond lengths (Å) and angles (°) of the stationary points determined at the CCSD(T)-F12b/aug-cc-pVTZ level of theory corresponding to the NC^- + CH_3Y [Y = F, Cl, Br, I] S_N2 reactions. Results denoted by † correspond to the MP2/aug-cc-pVDZ geometries. (Taken from ref. [3].) The structures and harmonic vibrational frequencies of all the stationary points are given in the supplementary information of ref. [8].

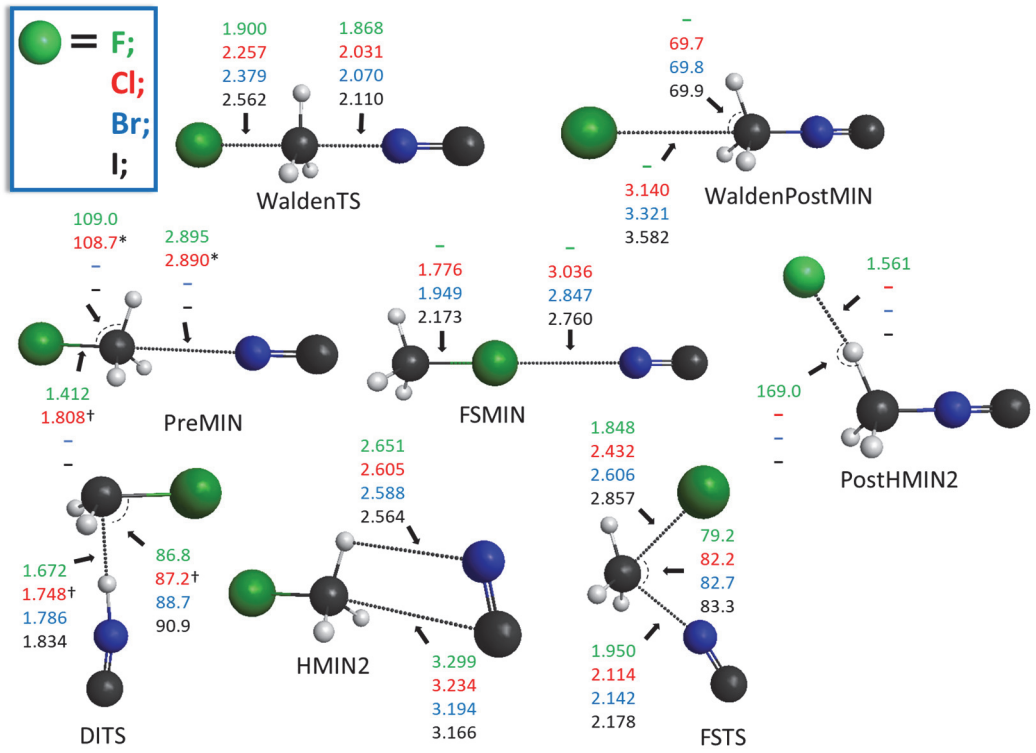

Figure 4.12 The most relevant bond lengths (Å) and angles (°) of the stationary points determined at the CCSD(T)-F12b/aug-cc-pVTZ level of theory corresponding to the $CN^- + CH_3Y$ [Y = F, Cl, Br, I] S_N2 reactions. Results denoted by † and * correspond to the MP2/aug-cc-pVDZ and CCSD(T)-F12b/aug-cc-pVDZ geometries. (Taken from ref. [3].)

For both S_N2 reactions, several stationary points belong to the C_{3v} symmetry group: PreMIN, WaldenTS, WaldenPostMIN, FSMIN, although HMIN1, HMIN2, HTS2, PostHMIN2, FSTS and DITS have C_s symmetry. In each case, the forming C–C bond is longer than to the corresponding C–N bond. For instance, in WaldenTS, the forming C–C bond is lengthened by 0.186, 0.207, 0.220 and 0.231 Å, for Y = F, Cl, Br and I, in order, relative to the corresponding C–N distances of the competitive C–N-bond-forming S_N2 reaction. The breaking C–Y bonds of $NC^- + CH_3Y$ are shorter than that of the $CN^- + CH_3Y$, except at FSMIN. Regarding the transition states of retention pathways, the Y–C–N bond angles of FSTS are nearly similar for each reaction, and the breaking C–HCN bonds of DITS of $NC^- + CH_3Y$ are lengthened by ~0.2 Å than the corresponding C–HNC distances. Similar to the post-reaction complexes of the $OH^- + CH_3Y/CH_3CH_2Y$ reactions discussed earlier, the dissociation energy of the halogen varies inversely with the C–Y bond distance at PostHMIN2 and WaldenPostMIN; smaller the distance is, larger the corresponding dissociation energy becomes.

The benchmark *ab initio* energies of the stationary points and several pathways for $NC^-/CN^- + CH_3Y$ including the post-CCSD(T) correlations, relativistic effects, core correlation and ZPE contributions are shown in Tables S1 and S2 in Appendix. The classical and adiabatic energies of WaldenTS and products of the $NC^-/CN^- + CH_3I$ reactions determined by Carrascosa and co-workers[53] at the MP2/aug-cc-pVDZ and CCSD(T)/aug-cc-pVTZ levels of theory are presented in Table 4 compared with the corresponding benchmark values and with the "experimental" 0 K gas-phase enthalpies obtained from the ATcT.[142] Our high-level *ab initio* reaction enthalpies are in splendid agreement with the experimental values, within ± 0.65 kcal mol^{-1}. In contrast, in case of the reaction enthalpy of $NC^- + CH_3I$ computed by Carrascosa *et al.*, enormous difference of 4.23 kcal mol^{-1} can be seen, while for $CN^- + CH_3I$ only 0.82 kcal mol^{-1} is found. Regarding WaldenTS, the deviations of the classical (adiabatic) energies are less than ~2 kcal mol^{-1}: 1.87 (0.95) and 2.10 (1.47) kcal mol^{-1} for $NC^-/CN^- + CH_3I$, respectively.

Table 4. Experimental and our benchmark *ab initio* 0 K reaction enthalpies and relative energies of the transition states (WaldenTS) of the Walden-inversion pathways (kcal mol^{-1}) for the $NC^-/CN^- + CH_3I$ S_N2 reactions.

$NC^- + CH_3I$ reaction	**Carrascosa *et al.*[53]**		**Benchmark [3]**		**Experimental[e]**
	classical[a]	**adiabatic[b]**	**classical[c]**	**adiabatic[d]**	
WaldenTS	−4.38	−4.84	−6.25	−5.79	−
$I^- + CH_3CN$	−45.89	−42.43	−48.79	−46.37	−46.66 ± 0.08
$CN^- + CH_3I$ reaction					
WaldenTS	−0.23	−0.69	−2.33	−1.82	−
$I^- + CH_3NC$	−21.68	−20.29	−24.18	−21.76	−21.11 ± 0.12

[a] CCSD(T)/aug-cc-pVDZ single-point calculations at the MP2/aug-cc-pVDZ geometries. [b] MP2/aug-cc-pVDZ. [c] Benchmark classical relative energies obtained from Eq. (4.7). [d] Benchmark adiabatic relative energies are defined in Eq. (4.8). [e] Data obtained from the 1.122p version of the Active Thermochemical Tables (ATcT).[141,142]

The basis-set convergence of the CCSD(T)-F12b relative energies is depicted in Figure 4.13. Besides S_N2, other product channels are investigated, as well: HCN/HNC + CH_2Y^-, $H^- + YH_2CCN$/ YH_2CNC, $YCN^-/YNC^- + CH_3$, FCN/FNC + CH_3^- and $YHCN^- + CH_2$, and their *ab initio* energies are detailed in Tables S1 and S2 in Appendix. The CCSD(T)-F12b/aug-cc-pVTZ structures of the studied products of the $NC^-/CN^- + CH_3Y$ reactions are shown in Figure S2 in Appendix.

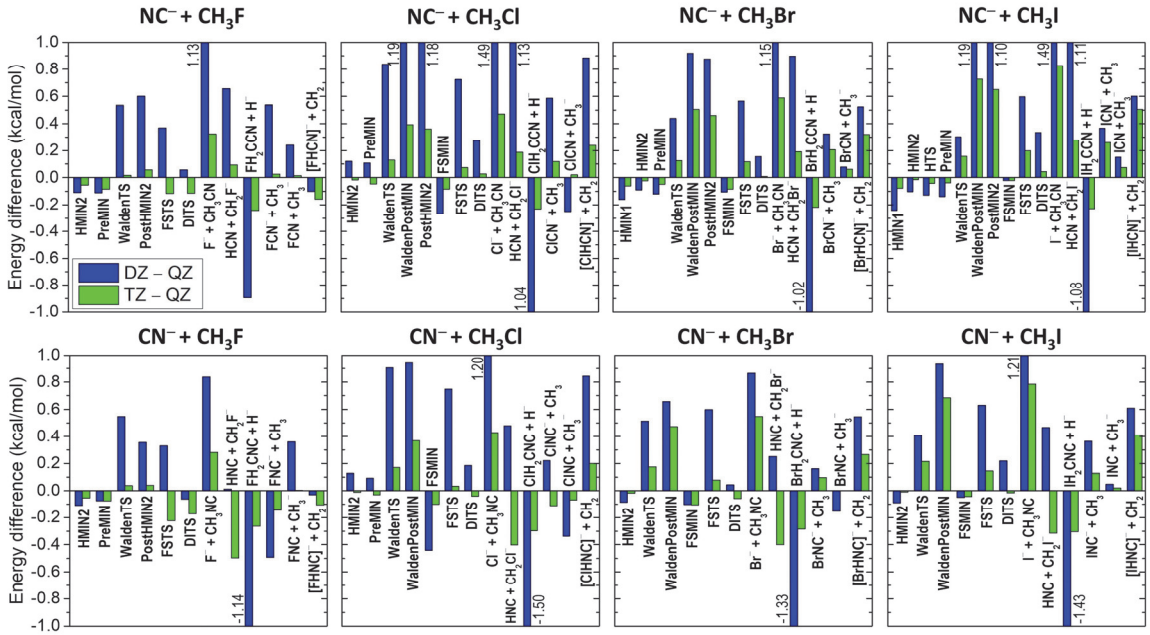

Figure 4.13 Basis-set convergence of the CCSD(T)-F12b relative energies of the stationary points and studied products for the $NC^-/CN^- + CH_3Y$ [Y = F, Cl, Br, I] reactions. (Taken from ref. [3].)

For the stationary points in the entrance channels (HMIN1, HMIN2, PreMIN, HTS2 and FSMIN), small differences of the relative energies are revealed. In most cases, the DZ−QZ and TZ−QZ values of WaldenTS and FSTS are more notable than that of DITS. WaldenPostMIN, PostHMIN2 and the product channels of S_N2, proton abstraction and hydride ion substitution ($H^- + YH_2CCN/YH_2CNC$) have the most significant basis-set impact on the relative energies: DZ−QZ deviations of ~1.5 kcal mol^{-1} take place at $Cl^- + CH_3CN$, $I^- + CH_3CN$ and $HNC + CH_2Cl^-$. The largest TZ−QZ differences are exposed for the $NC^-/CN^- + CH_3I$ reactions, reaching the value of 0.7–0.8 kcal mol^{-1} at the S_N2 products and WaldenPostMIN. Generally, as it is expected, |DZ−QZ| values are smaller than the corresponding |TZ−QZ|, except for some cases, in particular for the product of $HNC + CH_2F^-$, outstanding difference can be assigned, where DZ−QZ is only 0.01 kcal mol^{-1}, while TZ−QZ is 0.50 kcal mol^{-1}.

The auxiliary energy contributions of the stationary points and the investigated product channels are presented in Figure 4.14. The smallest corrections can be identified at the reactant channel (PreMIN, HMIN1, HMIN2, HTS2 and FSMIN), each value is between ±0.13 kcal mol^{-1}, excluding PreMIN for $NC^- + CH_3Cl$, where $\delta T = 0.76$ kcal mol^{-1}. Among the transition states, FSTS has the largest contributions, although in every case, core correlation always reduces the cumulative effect.

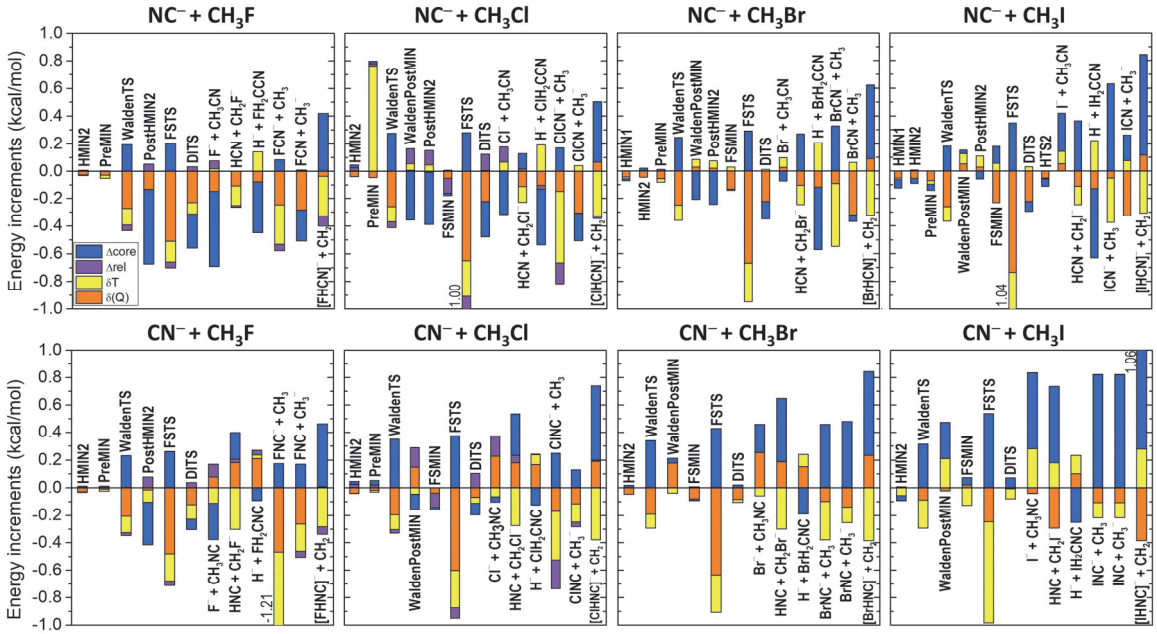

Figure 4.14 Auxiliary energy contributions (core correlation corrections (Δcore), scalar relativistic effects (Δrel) and the post-CCSD(T) correlation corrections (δT and δ(Q)) obtained from Eq. (4.2)–(4.4) and Eq. (4.6)) for the stationary points and products of the $NC^-/CN^- + CH_3Y$ [Y = F, Cl, Br, I] reactions. In case of Y = Br and I, Δrel is not presented as discussed in Section 4.1. (Taken from ref. [3].)

Besides FSTS, substantial contributions appear for the products, especially for the reactions of CH_3I. For instance, at $[IHCN]^- + CH_2$ and $INC + CH_3^-$, a Δcore of 0.78 and of 0.82 kcal mol^{-1} occurs. However, concerning post-CCSD(T), the largest contribution is found for the products of $FNC^- + CH_3$ (−1.21 kcal mol^{-1}). The relativistic effects are usually small (< 0.1 kcal mol^{-1}), but analogously, for the reaction enthalpies more significant values emerge (−0.21 kcal mol^{-1} for $ClNC^- + CH_3$). Altogether, the auxiliary energies commonly cancel each other, nevertheless, these contributions must be considered in order to reach sub-chemical accuracy as the cumulative effects are more than 0.5 kcal mol^{-1} in some cases. The ZPE effects are between ±0.65 kcal mol^{-1} for the most stationary points, however sometimes, notably at DITS, higher effects take place. Similarly, products have larger ΔZPEs (mostly negative) with a maximum effect of −6.61 kcal mol^{-1} at $FHCN^- + CH_2$.

4.1.3 The $X^- + CH_3Y$ [X = SH, NH_2, PH_2, Y = F, Cl, Br, I] S_N2 reactions

The stationary points of the S_N2 reactions between SH^-, NH_2^- and PH_2^- with methyl halides are displayed in Figures 4.15–4.17. [8] In Table 5, the high-level *ab initio* energies of several featured stationary points of the $X^- + CH_3Y$ (X = SH, NH_2, PH_2, Y = F, Cl, Br, I) systems are summarized. The structures and harmonic vibrational frequencies of all the stationary points are given in the supplementary information of ref. [8]. The only endothermic route is $SH^- + CH_3F$ with a reaction enthalpy of 11.1 kcal mol^{-1}, the most exothermic is $NH_2^- + CH_3I$ (−80.4 kcal mol^{-1}). As foreseen based on the previous systems of $OH^- + CH_3Y/CH_3CH_2Y$ and $CN^-/NC^- + CH_3Y$, the classical (adiabatic) energies of the minima, transition states and reaction enthalpies decrease with increasing atomic weight of the halogen.

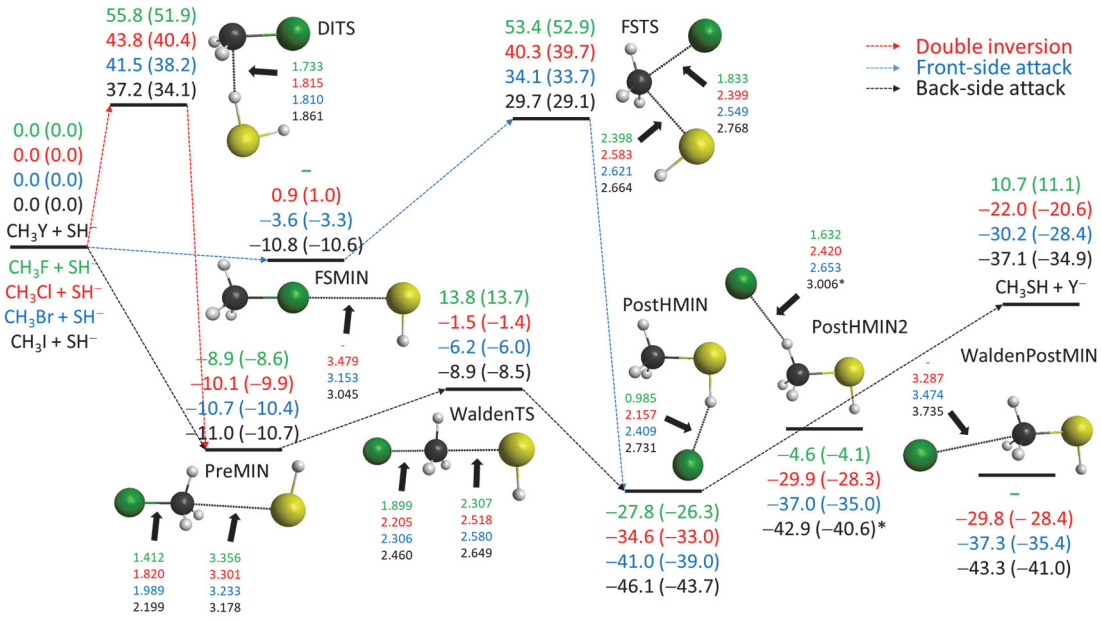

Figure 4.15 Schematic representation of the potential energy surfaces of the $SH^- + CH_3Y$ [Y = F, Cl, Br, I] S_N2 reactions showing the benchmark classical (adiabatic) relative energies (kcal mol^{-1}) obtained from Eq. (4.1) and the relevant CCSD(T)-F12b/aug-cc-pVTZ bond lengths (Å) of the stationary points along the possible paths. Results denoted by * correspond to the CCSD(T)-F12b/aug-cc-pVDZ structures. (Taken from ref. [8].)

In case of SH^-, three complexes (two H-bonded and one ion-dipole) are situated in the product channel, and in each reaction the global minimum is at PostHMIN above by 22.3 (22.0), 34.4 (32.4), 34.0 (31.8) and 33.3 (31.2) kcal mol^{-1} compared to the

reactions of $OH^- + CH_3Y$, Y = F, Cl, Br and I, in order, at the same level of theory (see Table 1). The order of the adiabatic energies of the product-like complexes is PostHMIN < WaldenPostMIN < PostHMIN2, whilst in respect of the classical energies, the trend breaks at Y = Cl: PostHMIN < PostHMIN2 < WaldenPostMIN. In the entrance channel, H-bonded complex cannot be identified (except for Y = I), moreover, PreMIN is below FSMIN by 0.2 (0.1), 7.1 (7.1) and 9.2 (8.9) kcal mol^{-1} suggesting a minor front-side complex formation mechanism. As typically, the barrier height of the Walden-inversion pathway is decreasing with increasing atomic weight of Y: 22.7 (22.3), 8.6 (8.5), 4.5 (4.4) and 2.1 (2.2) kcal mol^{-1}, for Y = F, Cl, Br, I, respectively. Similarly to $NC^-/CN^- + CH_3F$, WaldenTS has a positive classical (adiabatic) relative energy at Y = F. In case of $SH^- + CH_3F$, WaldenPostMIN and FSMIN cannot be characterized. In the matter of the retention pathways, FSTS is energetically more preferred than DITS, except at Y = F, if ZPEs are considered. Even so, both routes may occur at higher E_{coll}, because the barrier heights of the transition states are above ~30 kcal mol^{-1} in all reactions.

Concerning the reactant channel of $NH_2^- + CH_3Y$, besides the traditional ion-dipole complex (PreMIN), a H-bonded complex (HMIN) is also exposed and for Y = I, an additional PreTS is determined. The structure of PreTS differs from the conventional WaldenTS, the NH_2 group is rotated around the Y–C–N axis, withal, WaldenTS cannot be determined for Y = Br and I. Since the relative classical (adiabatic) energy of WaldenTS is −3.0 (−1.9) kcal mol^{-1} for Y = F, each stationary point of Walden inversion is submerged. Only one complex is observed in the exit channel (PostHMIN), in which the leaving Y connects to one of the hydrogens of the NH_2 group. As it is seen in Figure 4.16, PostHMIN is the global minimum of the PES, and the energy drop is huge between WaldenTS and PostHMIN: a difference of 53.5 (50.5) and 68.2 (63.6) kcal mol^{-1} is revealed for Y =F and Cl. Nonetheless, the D_e (D_0) dissociation energies of PostHMIN of the $OH^- + CH_3Y$ reactions [30.1 (30.5), 16.4 (15.9), 14.2 (13.6) and 11.7 (11.2) kcal mol^{-1}, for Y = F, Cl, Br and I, at the same level of theory (Table 1)] are more significant than those of NH_2^- [18.2 (17.9), 10.0 (9.5), 8.7 (8.3) and 7.3 (7.0) kcal mol^{-1}, for Y =F, Cl, Br and I, respectively]. As usual, in case of Y = F, FSMIN does not exist, and the energy depth of the front-side complex is increasing with Y. This indicates that, FSMIN is the most stable complex in the reactant region of the $NH_2^- + CH_3I$ S_N2 reaction, lowered by a classical (adiabatic) energy of 9.5 (8.7) kcal mol^{-1} relative to HMIN. Conventionally, based on the previous systems of $X^- + CH_3Y$ [X = OH, CN, SH; Y = Cl,

Br, I], the Y–X bond in FSMIN decreases as the atomic weight of Y increases; in case of NH_2^-, this tendency breaks as the I–NH_2 bond length is longer than the Br–NH_2 distance.

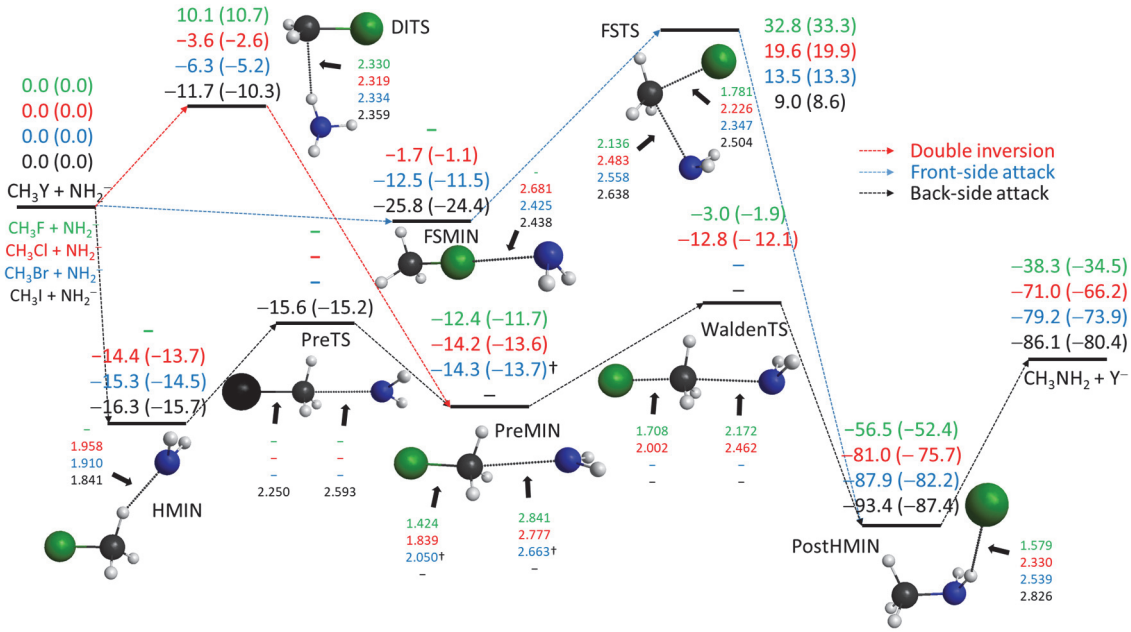

Figure 4.16 Schematic representation of the potential energy surfaces of the NH_2^- + CH_3Y [Y = F, Cl, Br, I] S_N2 reactions showing the benchmark classical (adiabatic) relative energies (kcal mol^{-1}) obtained from Eq. (4.1) and the relevant CCSD(T)-F12b/aug-cc-pVTZ bond lengths (Å) of the stationary points along the possible paths. Results denoted by † correspond to MP2/aug-cc-pVDZ. (Taken from ref. [8].)

In contrast to SH^- + CH_3Y [Y = F, Cl, Br, I], DITS is below FSTS, and the energy differences between the transition states [22.7 (22.6), 23.2 (22.5), 19.8 (18.5) and 20.7 (18.6) kcal mol^{-1}, for Y = F, Cl, Br and I, respectively] are in accordance with the cases of OH^- + CH_3Y [25.3 (26.2), 25.2 (25.7), 21.4 (21.9), 21.2 (21.6) kcal mol^{-1}, in the same order]. However, as opposed to OH^- + CH_3Y, DITS is submerged not only for Y =I [−11.7 (−10.3) kcal mol^{-1}], but also for Y = Cl and Br with an energy of −3.6 (−2.6) and −6.3 (−5.2) kcal mol^{-1}.

The Walden inversion of PH_2^- + CH_3Y can proceed *via* PreTS [Y = Cl, Br, I] → PreMIN [Y = F, Cl, Br] → WaldenTS [Y = F, Cl, Br] → PostHMIN2 [Y = F, Cl, Br, I] / PostHMIN [Y = F] / WaldenPostMIN [Y =Br]. WaldenTS of PH_2^- + CH_3F emerges with an energy of 9.7 (9.8) kcal mol^{-1}, whereas for Y = Cl, Br and I, Walden inversion is submerged. The global minimum of PH_2^- + CH_3Y [Y = Cl, Br and I] is at PostHMIN2 [−52.0 (−49.6), −59.3 (−56.5) and −65.2 (−61.9) kcal mol^{-1}, respectively], where the

leaving Y forms a bond with an H of the methyl group, whilst for Y = F, the global minimum of the PES is located at PostHMIN [−32.8 (−31.2) kcal mol^{-1}]. In case of Y = Br, WaldenPostMIN is unveiled above PostHMIN2 by only 1.6 (1.4) kcal mol^{-1}. In the entrance channel, no H-bonded complex is found, in spite of that PreTS, PreMIN and FSMIN is characterized. The $D_e(D_0)$ dissociation energies of FSMIN are less substantial compared to the $NH_2^- + CH_3Y$ systems, moreover, in case of CH_3Cl, the classical (adiabatic) energy of FSMIN is positive [1.1 (1.3) kcal mol^{-1}]. The barrier heights of Walden inversion of Y = F and Cl are higher [17.7 (17.3) and 4.9 (4.9) kcal mol^{-1}] than those of $NH_2^- + CH_3Y$ [9.4 (9.8) and 1.4 (1.5) kcal mol^{-1}], whereas for $SH^- + CH_3Y$ [Y = F and Cl], more significant barrier hights are seen: 22.7 (22.3) and 11.6 (11.3) kcal mol^{-1}.

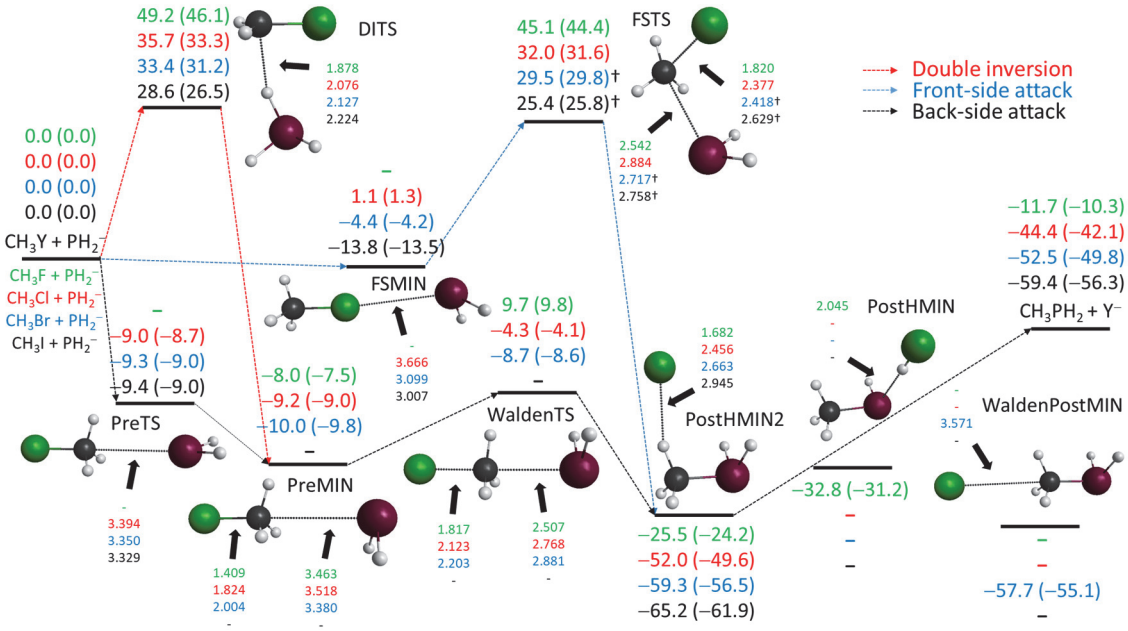

Figure 4.17 Schematic representation of the potential energy surfaces of the $PH_2^- + CH_3Y$ [Y = F, Cl, Br, I] S_N2 reactions showing the benchmark classical (adiabatic) relative energies (kcal mol^{-1}) obtained from Eq. (4.1) and the relevant CCSD(T)-F12b/aug-cc-pVTZ bond lengths (Å) of the stationary points along the possible paths. Results denoted by † correspond to MP2/aug-cc-pVDZ. (Taken from ref. [8].)

The PreTS of $PH_2^- + CH_3I$ is less stable than in case of $NH_2^- + CH_3I$, a deviation of ~6.2 kcal mol^{-1} is obtained. Similar to $SH^- + CH_3Y$, DITS is above FSTS, although the classical energy differences of the corresponding transition states are not increasing with the atomic weight of Y (4.1, 3.7, 3.9 and 3.2 kcal mol^{-1}, for Y = F, Cl, Br and I, in order).

Table 5. The benchmark *ab initio* classical and adiabatic energies (kcal mol^{-1}) of numerous stationary points obtained from Eq. (4.1) relative to the reactants for the $X^- + CH_3Y$ [X = SH, NH_2, PH_2; Y = F, Cl, Br, I] S_N2 reactions.

Stationary points of $X^- + CH_3Y$	X = SH		X = NH_2		X = PH_2	
Y = F	Classical[a]	Adiabatic[a]	Classical[a]	Adiabatic[a]	Classical[a]	Adiabatic[a]
PreMIN	−8.88	−8.56	−12.41	−11.75	−7.98	−7.52
WaldenTS	13.84	13.74	−3.03	−1.89	9.75	9.84
global minimum	PostHMIN		PostHMIN		PostHMIN	
	−27.76	−26.33	−56.45	−52.40	−32.79	−31.21
FSTS	53.41	52.92	32.78	33.35	45.10	44.44
DITS	55.82	51.89	10.14	10.69	49.16	46.06
Y^-+CH_3X	10.71	11.12	−38.32	−34.46	−11.67	−10.34
Y = Cl	Classical[a]	Adiabatic[a]	Classical[a]	Adiabatic[a]	Classical[a]	Adiabatic[a]
PreMIN	−10.12	−9.86	−14.20	−13.62	−9.16	−9.02
WaldenTS	−1.53	−1.36	−12.82	−12.14	−4.30	−4.11
global minimum	PostHMIN		PostHMIN		PostHMIN2	
	−34.57	−33.03	−81.01	−75.69	−52.03	−49.62
FSMIN	0.86	1.02	−1.70	−1.12	1.12	1.35
FSTS	40.29	39.67	19.56	19.93	31.99	31.60
DITS	43.76	40.42	−3.59	−2.60	35.66	33.30
Y^-+CH_3X	−22.00	−20.61	−71.03	−66.18	−44.38	−42.06
Y = Br	Classical[a]	Adiabatic[a]	Classical[a]	Adiabatic[a]	Classical[a]	Adiabatic[a]
PreMIN	−10.69	−10.43	−14.27	−13.70	−10.03	−9.76
WaldenTS	−6.20	−5.95	–	–	−8.75	−8.55
global minimum	PostHMIN		PostHMIN		PostHMIN2	
	−41.01	−39.03	−87.87	−82.21	−59.27	−56.53
FSMIN	−3.55	−3.33	−12.52	−11.52	−4.43	−4.16
FSTS	34.10	33.67	13.50	13.32	29.52	29.77
DITS	41.47	38.20	−6.29	−5.19	33.39	31.21
Y^-+CH_3X	−30.15	−28.35	−79.18	−73.92	−52.53	−49.81
Y = I	Classical[a]	Adiabatic[b]	Classical[a]	Adiabatic[b]	Classical[a]	Adiabatic[b]
PreMIN	−11.03	−10.75	–	–	–	–
WaldenTS	−8.85	−8.51	–	–	–	–
global minimum	PostHMIN		PostHMIN		PostHMIN2	
	−46.10	−43.67	−93.40	−87.38	−65.17	−61.95
FSMIN	−10.81	−10.59	−25.78	−24.45	−13.84	−13.46
FSTS	29.67	29.11	9.03	8.64	25.37	25.81
DITS	37.20	34.12	−11.70	−10.33	28.56	26.50
Y^-+CH_3X	−37.06	−34.86	−86.09	−80.43	−59.44	−56.32

[a] The results are taken from ref. [8], and obtained as Eq. (4.1).

4.2 Development of the potential energy surfaces of the $OH^- + CH_3Y$ [Y = F, I] and $NH_2^- + CH_3I$ reactions

4.2.1 Computational details

In the thesis, three global, analytical PESs ($OH^- + CH_3I$, $OH^- + CH_3F$ and $NH_2^- + CH_3I$) are developed utilizing the in-house ROBOSURFER program package.[124] [2, 4, 7] The process of the development is invented for the $OH^- + CH_3I$ reaction, and nearly the same strategy is used for the other two, $OH^- + CH_3F$ and $NH_2^- + CH_3I$ PES developments.

Firstly, an initial set of geometries is constructed by (1) changing the Cartesian coordinates of the stationary points and (2) randomly positioning the products around each other in the 2.0–10.0 Å range. The energies of the structures are calculated at the MP2/aug-cc-pVDZ(-PP) level of theory. For I, a relativistic effective core potential and the corresponding pseudo-potential (PP) basis set are applied. Then, this initial dataset is utilized by ROBOSURFER, in order to improve the corresponding PES iteratively at the same level of theory. At each iteration, 24 trajectories are carried out at b of 0.0, 0.5, 1.0, 1.5, 2.0, 2.5, 4.0, 9.0 bohr (3 iterations at every b). The fitting of the energy points is completed using the PIP approach[122,144,145] with a fifth-order expansion of polynomials of Morse-like variables, $y_{ij} = \exp(-r_{ij}/a)$; for more details, see Section 3.2. A weighted linear least-squares fit is employed with a function of $E_0/(E + E_0)\times E_1/(E + E_1)$, where E is the energy relative to the global minimum, $E_0 = 0.15$ hartree (= 94 kcal mol^{-1}) and $E_1 = 0.5$ hartree (= 314 kcal mol^{-1}). The most important parameters for the three PES developments are listed in Table 6. The targeted PES accuracy is set to 0.5 kcal mol^{-1}, the full accuracy limit is determined by considering the ZPEs of the reactants and the maximum E_{coll} of interest reduced by a value of ~14 kcal mol^{-1} (for $OH^- + CH_3I/CH_3F$) or 20 kcal mol^{-1} (for $NH_2^- + CH_3I$) based on previous study of the $F^- + CH_3Br$ system. In course of each case, the HOLEBUSTER subprogram is not used. The development of the PES is carried out at several E_{coll} within the proposed range of E_{coll}, meanwhile separate QCT simulations are performed to test the reliability of the PES. If the occurrence of the unphysical trajectories is negligible at each E_{coll}, the development of the PES is considered finished at the MP2/aug-cc-pVDZ level of theory. Afterwards, the energy points are recalculated at a higher level of theory (usually at CCSD(T)-F12b/aug-cc-pVTZ), moreover, when it is required (for the $NH_2^- + CH_3I$ reaction), the ROBOSURFER

is utilized with the unaltered conditions in order to improve the PES. In case of $OH^- + CH_3I$, the development contains 380 iterations (86, 89, 65, 41, 50 and 49) at E_{coll} of 5, 10, 20, 30, 40 and 50 kcal mol^{-1}, and for $OH^- + CH_3F$, 655 iterations (11, 85, 114, 85, 80, 55, 50, 50, 55 and 70) are performed at E_{coll} = 1, 5, 10, 20, 30, 40, 50, 60, 70 and 80 kcal mol^{-1}. In the matter of $NH_2^- + CH_3I$, at MP2/aug-cc-pVDZ, 262 iterations (90, 90, 64 and 18) are run at the E_{coll} of 5, 10, 20 and 30 kcal mol^{-1}, respectively.

Table 6. Important details about the potential energy surface developments of the $OH^- + CH_3I$/ CH_3F and $NH_2^- + CH_3I$ reactions utilized by the ROBOSURFER program. The details are summarized from ref. [2, 4, 7].

	$OH^- + CH_3I$	$OH^- + CH_3F$	$NH_2^- + CH_3I$
Number of the structures			
Initial dataset	13308	14702	13441
Final dataset	36514[a]	50434[a] + 999[b]	26918[a] + 4922[c]
Number of coefficients	4693	4693	5419
Number of iterations completed by ROBOSURFER at MP2/aVDZ	380	655	262
E_{coll} range of the PES development (kcal mol^{-1})	5 – 50	1 – 80	1 – 30
Full accuracy limit relative to free reactants (kcal mol^{-1})	64	95.2	65
Hard upper limit relative to the global minimum (kcal mol^{-1})	200	220	232

[a] The added new geometries are selected by the ROBOSURFER program at the MP2/aug-cc-pVDZ level of theory.
[b] The geometries are adjoined manually to the dataset.
[c] To refine the accuracy of the PES, at the composite level of theory defined in Eq. (4.9), additional iterations (47, 98 and 50) are performed with the ROBOSURFER program at E_{coll} = 5, 10 and 20 kcal mol^{-1}, respectively.

For the QCT simulations, the vibrational ground states of the reactants (OH^-, NH_2^-, CH_3F and CH_3I) are prepared by standard normal-mode sampling,[120] and the rotational angular momenta are adjusted to zero. The initial distance of the reactants is 25 bohr ($OH^- + CH_3F$) and 40 bohr ($OH^- + CH_3I$, $NH_2^- + CH_3I$) with a given b. With a step size of 0.5 bohr, at each E_{coll}, b is scanned from 0 to b_{max} (where the reaction probability becomes 0). At each b, 5000 trajectories are run with a 0.0726 fs time step and terminated

when the largest interatomic distance becomes larger than the largest initial one by 1 bohr. Commonly, in the matter of proton abstraction and S_N2, (1) soft and (2) hard ZPE restrictions are applied: (1) reject those trajectories, where the sum of the product classical vibrational energies is smaller than the sum of their ZPEs on the PES, (2) discard trajectories, where the vibrational energy of either product is less than the corresponding ZPE on the PES.

4.2.2 The failure of the CCSD(T) method

For $OH^- + CH_3I$, the initial dataset contains 13308 structures, and at the end of the PES development, the final dataset comprises of 36539 geometries. To achieve more accurate PES, the energy points are recomputed at CCSD(T)-F12b/aug-cc-pVTZ. However, running QCT simulations on the constructed CCSD(T)-F12b PES, surprisingly, appreciable fraction (~10 %) of unphysical trajectories occurs. Comparing the MP2/aug-cc-pVDZ and CCSD(T)-F12b/aug-cc-pVTZ values of the dataset, even though the the root-mean-square (RMS) fitting error is 4.5 kcal mol^{-1}, it is unveiled that, in case of 17 geometries, the CSSD(T)-F12b/aug-cc-pVTZ energies are below the corresponding MP2 results by more than 50 kcal mol^{-1}. [6, 7] In light of this, the potential energies of the geometries are recalculated utilizing several methods of DF-MP2-F12, BCCD,[107,146,147] CCSD-F12b, BCCD(T)[148,149] with aug-cc-pVDZ or aug-cc-pVTZ basis sets. The distributions of the differences between the recomputed *ab initio* energies and the MP2/aug-cc-pVDZ data are depicted in Figure 4.18. In cases of BCCD/aug-cc-pVDZ, CCSD-F12b/aug-cc-pVTZ, BCCD(T)/aug-cc-pVDZ and CCSD(T)-F12b/aug-cc-pVTZ, the most occupied energy interval of the deviations is that between −5 and −3 kcal mol^{-1}. For DF-MP2-F12/aug-cc-pVTZ, the energy range between 0 and 1 kcal mol^{-1} is the most populated. At the 17 problematic structures, the largest energy differences induced by CCSD(T)-F12b/aug-cc-pVTZ are diminished in case of the other levels of theory. However, the CCSD-F12b method also provides significant energy deviations for some geometries in the ranges of 10–20 and 20–50 kcal mol^{-1}.

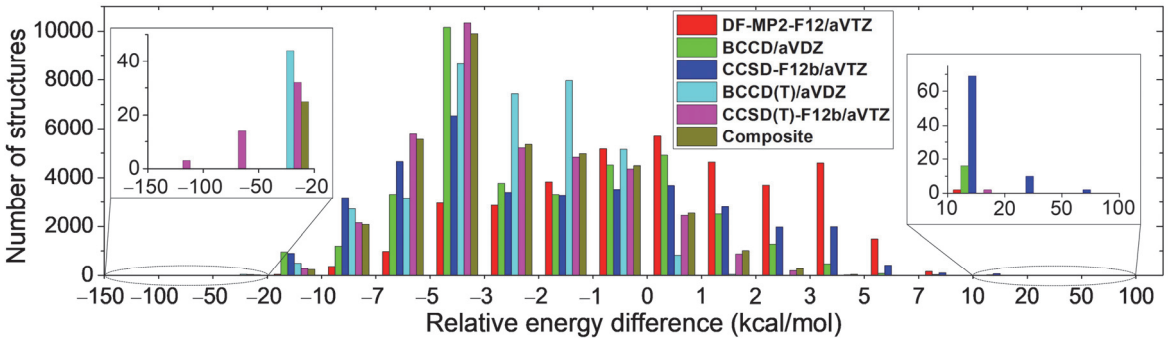

Figure 4.18 The numerical distributions of the structures as a function of the differences between the energies obtained at several *ab initio* levels of theory and the corresponding MP2/aug-cc-pVDZ values for the final dataset of the $OH^- + CH_3I$ potential energy surface. The composite energies refer to CCSD-F12b/aug-cc-pVTZ + BCCD(T)/aug-cc-pVDZ – BCCD/aug-cc-pVDZ. (Taken from ref. [7].)

In order to solve the above-mentioned issues, a composite method is defined as:

$$\text{CCSD-F12b/aug-cc-pVTZ} + \text{BCCD(T)/aug-cc-pVDZ} - \text{BCCD/aug-cc-pVDZ}, \tag{4.9}$$

in which the pleasant basis-set convergence is provided by the first addend (CCSD-F12b/aug-cc-pVTZ), and the (T) effect is determined by the Brueckner coupled cluster method. As it is seen in Figure 4.18, the proposed composite method does not fail at the crucial structures avoiding the occurrent false minima and maxima on the PES of $OH^- + CH_3I$. From the final dataset, respecting on the 17 critical geometries, a few are selected and the relative energies are obtained employing several *ab initio* methods with the aug-cc-pV*n*Z (n = 2,3) basis sets. In Figure 4.19, two representative examples are shown, and seven additional cases are presented in Appendix (Figure S3). The energies of the sample geometries are calculated at 18 levels of theory, taking into account the methods of HF, MP2, CCSD, CCSD(T), BCCD, BCCD(T), CCSDT, as well as, the optimized-orbital quasi-variational coupled cluster doubles (OQVCCD), and OQVCCD with perturbative triples (OQVCCD(T)).[150] The left side of Figure 4.19 represents a common configuration, where the *ab initio* energies agree with each other within ~4 kcal mol^{-1}, and the difference between BCCD(T)/aug-cc-pVDZ and BCCD/aug-cc-pVDZ is less than 0.8 kcal mol^{-1}. Similar deviation (0.86 kcal mol^{-1}) takes place for CCSD(T)-F12b/aug-cc-pVTZ and CCSD-F12b/aug-cc-pVTZ, furthermore, the CCSDT/aug-cc-pVDZ energy agrees well with these values. In contrast, the other case

(the right side of Figure 4.19) shows the outcome of the substantial correlation effects. The MP2, CCSD and OQVCCD methods give compatible results, in the range of ~50–60 kcal mol^{-1} depending on the basis set, whereas considering the (T) effect for the BCCD and OQVCCD methods, the energy drops by ~32 and ~36 kcal mol^{-1}. The failure of (T) of the CCSD method is obvious: The energy difference between CCSD(T)-F12b/aug-cc-pVTZ and CCSD-F12b/aug-cc-pVTZ is more than 120 kcal mol^{-1}. Meanwhile, CCSDT/aug-cc-pVDZ provide an energy of 29.74 kcal mol^{-1}, which is above CCSD(T)-F12b/aug-cc-pVTZ by 87.09 kcal mol^{-1}. On the other hand, the composite method performs the best as its deviation from CCSDT/aug-cc-pVDZ is only 1.37 kcal mol^{-1}. Regarding the additional geometries in Figure S3, similar findings can be stated.

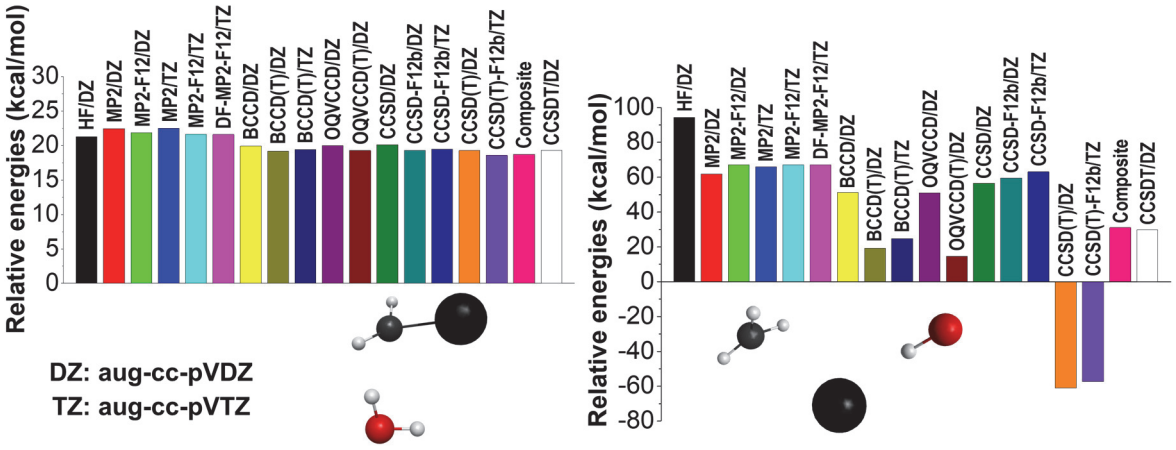

Figure 4.19 Relative energies of two representative structures of the final dataset obtained by numerous *ab initio* levels of theory in the course of the $OH^- + CH_3I$ potential energy surface. (Taken from ref. [7].)

In Table 7, the (T) corrections obtained by the traditional coupled cluster and the Brueckner methods, as well as, the full-T corrections and the T_1-diagnostic values[108] are presented for the representative structures shown in Figures 4.19 and S4. T_1 diagnostic can evaluate that the utilized single-reference-based electron correlation method is reliable or not, a value greater than 0.02 signifies multi-reference character of the system. As it is seen, where the CCSD(T) method fails providing too negative corrections for (T), the Brueckner method performs well compared to the full-T corrections.

Table 7. The (T) and full-T corrections (kcal mol^{-1}) and the T_1 values of the representative structures of the final dataset of the OH^- + CH_3I potential energy surface. [7]

Geometries		(T)[a]	Brueckner (T)[b]	full-T[c]	T_1[d]
Figure 4.19	left	−0.86	−0.73	−0.86	0.014
	right	−120.50	−32.04	−26.73	0.157
Figure S3	A	−11.30	−8.43	−9.39	0.085
	B	−74.52	−43.73	−28.68	0.109
	C	−1.99	−2.27	−1.91	0.027
	D	−98.02	−34.96	−27.27	0.133
	E	−1.58	−1.63	−1.48	0.019
	F	−134.31	−33.23	−27.13	0.155
	G	−32.34	−12.06	−13.92	0.094

[a] (T) corrections obtained as CCSD(T)-F12b − CCSD-F12b using the aug-cc-pVTZ basis.
[b] Brueckner (T) corrections computed as BCCD(T) − BCCD using the aug-cc-pVDZ basis.
[c] Full-T corrections computed as CCSDT − CCSD using the aug-cc-pVDZ basis.
[d] T_1 diagnostic values computed at the CCSD-F12b/aug-cc-pVTZ level of theory.

At these critical structures, the T_1 values are expressly high (> 0.09), while at those cases, where the relative energies of the CCSDT and CCSD(T) methods are in accord with each other, the T_1 is smaller. The breakdown of CCSD(T) is related to the problematic electronic structure of these geometries by having a significant multi-reference character due to the homolytic breaking of the C–I bond. This downfall is caused by either the quasi-degeneracy of the HF orbitals or the incorrect single HF refence, which induce considerable errors at the (T) corrections of the CCSD method. In contrast to CCSD(T), the Brueckner coupled cluster method utilizes non-HF reference, thus the BCCD(T) method performs better promoting the convenience of the composite method defined in Eq. (4.9). It is noteworthy that this (T) failure is not unique: In cases of the dissociation of several molecules/anions (HF, N_2, S_2, OH^-, C_2, *etc.*), the potential energy curves showed the similar fault of the CCSD(T) method.[151–156]

In order to investigate the effects of the levels of theory on the OH^- + CH_3I dynamics, eight different PESs are constructed by recalculating the final dataset (36539 structures) with several methods, as seen in Table 8. [7] Two types of PESs are constructed at CCSD(T)-F12b/aug-cc-pVTZ, the * denotes the rejection of the 17 problematic geometries. The RMS values of the corresponding energy ranges, relative to

the global minimum, are also presented in Table 8 for each PES. The largest RMS error is obtained for the CCSD(T)-F12b/aug-cc-pVTZ PES, however removing the 17 structures, the RMS value decreases by 0.3 kcal mol^{-1} at the highest energy range. At lower energy ranges, the composite PES provides one of the lowest RMS errors, while at the 188 – 471 kcal mol^{-1} range, the values are similar to the CCSD-F12b/aug-cc-pVTZ and CCSD(T)-F12b/aug-cc-pVTZ* cases.

Table 8. The root-mean-square fitting errors (kcal mol^{-1}) and the size of the dataset of various potential energy surfaces for the $OH^- + CH_3I$ reaction.[a]

Level of theory	Number of structures	Energy ranges (kcal mol^{-1})		
		0 – 94	94 – 188	188 – 471
MP2/aug-cc-pVDZ	36539	1.02	1.76	1.68
DF-MP2-F12/aug-cc-pVTZ	36538	0.99	1.73	1.73
BCCD/aug-cc-pVDZ	36532	1.02	1.76	1.56
CCSD-F12b/aug-cc-pVTZ	36532	0.99	1.72	1.79
BCCD(T)/aug-cc-pVDZ	36532	1.03	1.74	1.51
CCSD(T)-F12b/aug-cc-pVTZ	36531	1.09	1.83	2.06
CCSD(T)-F12b/aug-cc-pVTZ*	36514[b]	1.02	1.72	1.76
Composite[a]	36529	1.00	1.69	1.81

[a] The root-meain-square fitting erros are adopted from ref. [7].
[b] The 17 outliers are removed from the final dataset, which removal is denoted by *.

The classical relative energies of the stationary points of the $OH^- + CH_3I$ S_N2 reaction obtained on the various PESs along with the benchmark data are depicted in Figure 4.20. In the entrance channel, the CCSD(T)-F12b/aug-cc-pVTZ* PES is more reliable than the composite PES; however, the differences between the composite and bechmark classical energies are within the chemical accurancy: 0.62, 0.56 and 0.53 kcal mol^{-1} at FSMIN, HMIN and HTS, respectively. Although, in the product channel and at FSTS and DITS, the two PESs give similar values, the largest deviation (0.13 kcal mol^{-1}) is found for the products. Regarding the other six PESs, in some cases, better agreement can be observed with the benchmark energies compared to the composite or the CCSD(T)-F12b/aug-cc-pVTZ* PESs, albeit, at certain stationary points, the provided energies differ from the benchmark data by more than 2 kcal mol^{-1}. To highlight a few examples: The classical energy of DITS is determined to be −0.93 kcal mol^{-1} on the

MP2/aug-cc-pVDZ PES, while the benchmark data is −3.85 kcal mol^{-1}. In respect of FSTS, the BCCD/aug-cc-pVDZ, the CCSD-F12b/aug-cc-pVTZ and the BCCD(T)/aug-cc-pVDZ PESs give classical relative energies of 19.29, 20.70 and 14.76 kcal mol^{-1}, respectively, above the benchmark value by 2.67, 4.08 and −1.86 kcal mol^{-1}, in order. On the MP2/aug-cc-pVDZ PES, the classical energy of the S_N2 products is −64.79 kcal mol^{-1}, while the benchmark reaction energy is −66.64 kcal mol^{-1}. Therefore, in order to reach the chemical accuracy at each region of the stationary points of the PES, the (T) correction, as well as, the explicit correlation must be considered. Overall, the accuracy of the composite PES is agreeable, not to mention the fact that the composite method solves the failure of the "gold-standard" CCSD(T) method at regions away from the stationary points.

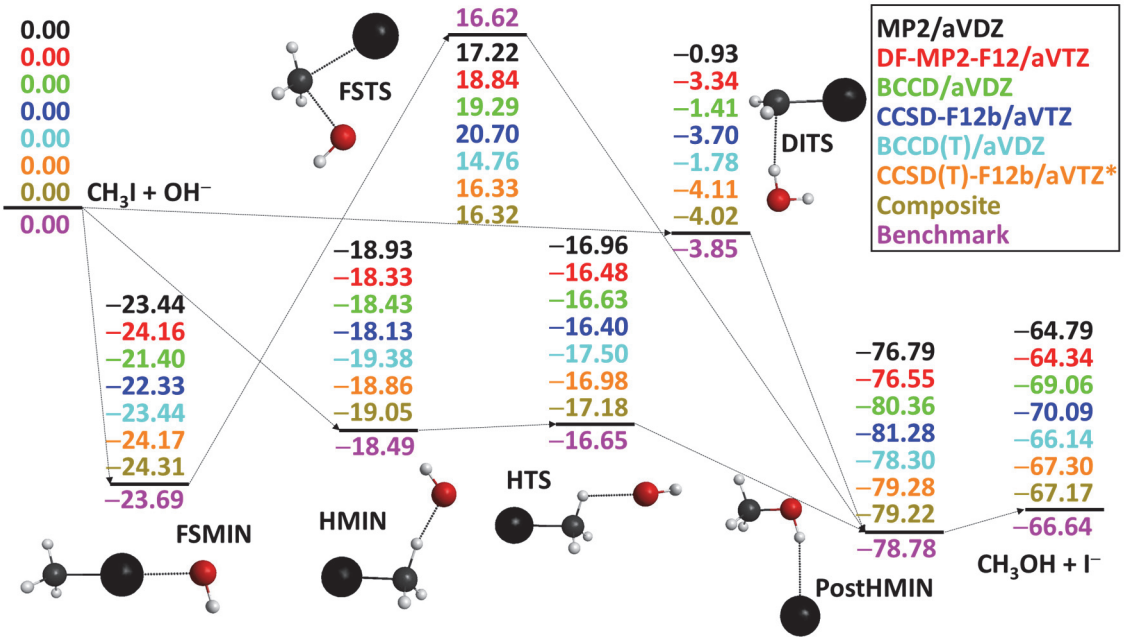

Figure 4.20 The classical relative energies (kcal mol^{-1}) of the stationary points along the OH^- + CH_3I S_N2 pathway obtained on the studied PESs. In case of the composite PES, the energy points are calculated as Eq. (4.9). (Taken from ref. [6, 7].)

Based on the previous study of Győri *et al.*,[157] the impacts of the levels of theory on the dynamics of the OH^- + CH_3I reaction are investigated focusing on the S_N2, proton-abstraction and rejected unphysical routes. QCT calculations are carried out at E_{coll} of 5, 20 and 50 kcal mol^{-1}, and in all, more than 210 000 simulations are computed. The ICSs of the pathways for each PES are illustrated in Figure 4.21. The opacity functions are displayed in Figure S4 in Appendix. The highest proportion of the rejected (unphysical)

trajectories is found for the CCSD(T)-F12b/aug-cc-pVTZ PES with an ICS of 13.0, 7.0 and 4.7 bohr^2 at 5, 20 and 50 kcal mol^{-1} E_{coll}, and when the 17 critical structures are removed, the ICS of the unphysical trajectories decreases to a value of 1.8, 0.5 and 1.3 bohr^2, respectively. In case of the composite PES, the ICS of the discarded trajectories is minimal: 0.3, 0.1 and 0.2 bohr^2 at E_{coll} of 5, 20 and 50 kcal mol^{-1}. However, for the S_N2 and proton-abstraction pathways, the CCSD(T)-F12b/aug-cc-pVTZ, CCSD(T)-F12b/aug-cc-pVTZ* and composite PESs provide comparable ICSs, for example at 20 kcal mol^{-1}, the S_N2 ICSs are 29.6, 29.3 and 28.7 bohr^2, respectively, and the proton-abstraction ICSs are 79.9, 80.5 and 76.2 bohr^2, in order.

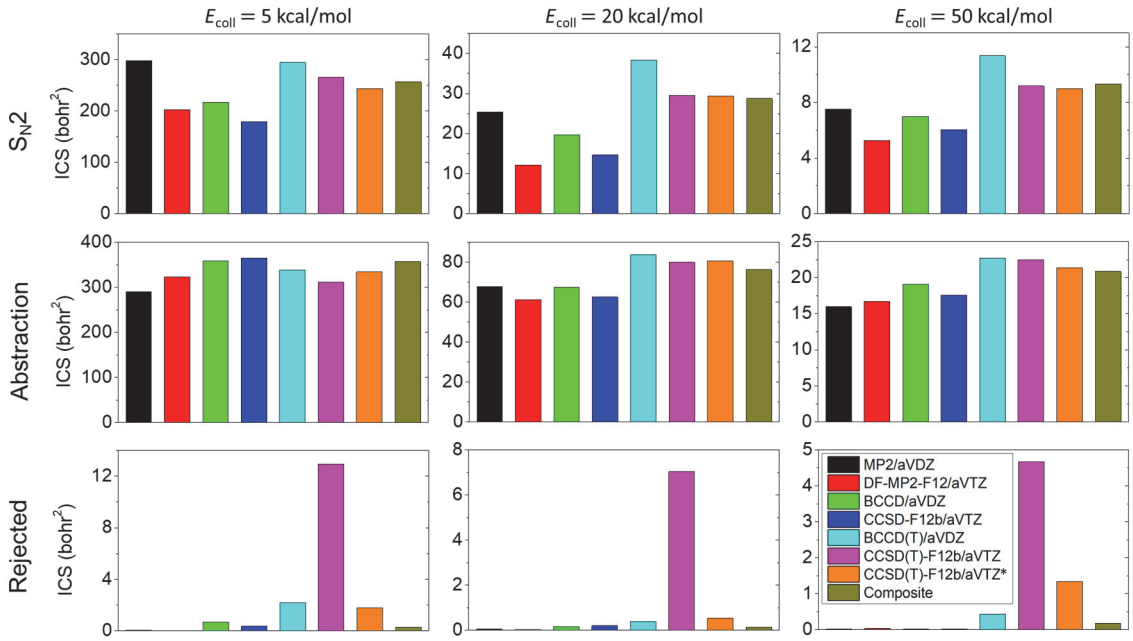

Figure 4.21 Cross sections of the S_N2, proton-abstraction and rejected channels for the $OH^- + CH_3I$ reaction computed on several *ab initio* potential energy surfaces at 5, 20 and 50 kcal mol^{-1} collision energies. (Taken from ref. [7].)

Similar to the $F^- + CH_3I$ case,[157] substantial method- and basis-set dependence can be observed, albeit, in the matter of the $OH^- + CH_3I$ proton-abstraction pathway, these effects are less significant. At each E_{coll}, the DF-MP2-F12 and CCSD-F12b methods underestimate the ICSs of the S_N2 and proton-abstraction pathways. Noteworthy that, in several cases, due to the opposite effects of the (T) correlation and the basis-set quality, the ICSs of the MP2/aug-cc-pVDZ PES are in good agreement with the values provided by the CCSD(T)-F12b/aug-cc-pVTZ and composite PESs. For S_N2, the ICSs of the BCCD/aug-cc-pVDZ PES exceed the values of the MP2/aug-cc-pVDZ and CCSD-

F12b/aug-cc-pVTZ PESs, as well as, for proton abstraction, the same can be seen at 20 and 50 kcal mol^{-1} E_{coll}. In most cases, the largest ICSs are yielded by the BCCD(T)/aug-cc-pVDZ PES, excluding at E_{coll} = 5 kcal mol^{-1}, where the ICSs of S_N2 and proton abstraction peak for the MP2/aug-cc-pVDZ and CCSD-F12b/aug-cc-pVTZ PESs at 298.0 and 364.5 bohr^2, in order.

Regarding the $OH^- + CH_3F$ and $NH_2^- + CH_3I$ PES developments, the same CCSD(T) failure can be unveiled, thuswise, for the recalculation of the MP2/aug-cc-pVDZ energy points, the novel composite method is utilized as defined in Eq. (4.9). It should be also noted that in case of $NH_2^- + CH_3I$, following the MP2 PES development, additional improvement is implemented at the composite level of theory by completing 47, 98 and 50 iterations at E_{coll} of 5, 10 and 20 kcal mol^{-1}, respectively, with the purpose of enhancing the accuracy of the PES. In case of $OH^- + CH_3F$, the RMS errors of the fitting are 0.83, 1.69, and 2.54 kcal mol^{-1}, and in case of $NH_2^- + CH_3I$, the RMS errors are 1.04, 1.68, and 2.37 kcal mol^{-1} for the energy ranges of 0–94 kcal mol^{-1}, 94–188 kcal mol^{-1}, and 188–471 kcal mol^{-1}, in order.

In conclusion, the composite method deals with the breakdown of the CCSD(T) method successfully, hence, for the PES development of the $OH^- + CH_3I/CH_3F$, $NH_2^- + CH_3I$ reactions, this proposed method can be employed.

4.3 Exploring the dynamics of the $OH^- + CH_3I$ reaction: Theory versus experiment

Following the characterization of the $OH^- + CH_3I$ S_N2 path and the confirmation of the reliability of the composite PES at the S_N2 stationary points, the next goal is to analyse the proton-abstraction pathway. [1] The representative PES of the $OH^- + CH_3I$ proton abstraction showing the benchmark classical relative energies of the stationary points derived from Eq. (4.5) with the corresponding PES values is depicted in Figure 4.22. The *ab initio* energies of the stationary points are summarized in Table 9. The proton-abstraction reaction is far less exothermic than S_N2, emerged by a classical (adiabatic) energy of −65.15 (59.85) kcal mol^{-1}. The proton-abstraction mechanism proceeds as HMIN → TS1'/TS1" → MIN1'/MIN1" → TS2 → MIN2, involving the same minimum in the reactant channel (HMIN) as S_N2. It should be highlighted that TS1' and TS1", as well as, MIN1' and MIN1" are conformational isomers, as a result of the rotation of the

OH group. The structures labelled by one comma (TS1' and MIN1') have *trans* arrangement, and the two commas denote (TS1" and MIN1") the *cis* arrangement.

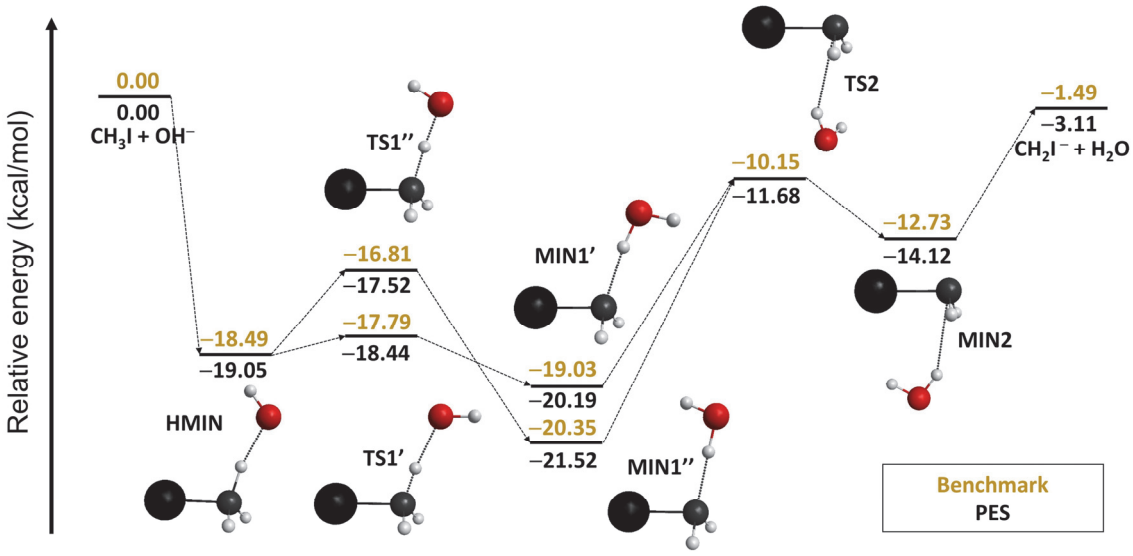

Figure 4.22 The benchmark classical relative energies (kcal mol^{-1}) of the stationary points compared with the PES values along the OH^- + CH_3I proton-abstraction pathway. The benchmark energies are calculated as Eq. (4.5). (Taken from ref. [1].) The structures of the proton-abstraction stationary points are given in the supplementary information of ref. [1].

All structures are below the reactants, and the global minimum of the path is at MIN1" with a classical energy of −20.35 kcal mol^{-1}. Without ZPE corrections, TS1" is above TS1' by 0.98 kcal mol^{-1} and MIN1" is below MIN1' by 1.32 kcal mol^{-1}. However, according to the DFT study by Xie *et al.*,[38] the classical energy of TS1' is higher than that of TS1" by 0.14 kcal mol^{-1}, and the MIN1' is deeper than MIN1" by 1.22 kcal mol^{-1}. The benchmark classical barrier heights of TS1' and TS1"are 0.70 and 1.68 kcal mol^{-1}, while the DFT values are 0.44 and 0.30 kcal mol^{-1}. As seen in Table 9, considering ZPE, the barrier of TS1' decreases to 1.04 kcal mol^{-1}, and in case of TS1", the barrier disappears. The classical energy drops by 2.58 kcal mol^{-1} between TS2 and MIN2, while using the DFT method that depth is 1.86 kcal mol^{-1}. In general, the differences between the benchmark and DFT energies of the stationary points are sometimes noticeable, for TS1" a deviation of 2.96 kcal mol^{-1} is incurred. The energies provided by the PES are in accord with the benchmark results: For HMIN, TS1' and TS2", the errors are below 1 kcal mol^{-1} (0.56 and 0.65 and 0.71 kcal mol^{-1}, respectively), howbeit, for MIN1', MIN1", TS2 and

MIN2, the discrepancies are somewhat larger (1.16, 1.17, 1.53 and 1.39 kcal mol^{-1}, in order), peaking at the CH_2I^- +H_2O products with 1.62 kcal mol^{-1}.

Table 9 The computed benchmark *ab initio* energies along with the post-CCSD(T) and core correlation effects (kcal mol^{-1}) of the stationary points relative to the reactants for the OH^- + CH_3I proton-abstraction reaction. The results are adopted from ref. [1].

ABS	TZ[a]	QZ[b]	δT[c]	δ(Q)[d]	Δcore[e]	Classical[f]	ΔZPE[g]	Adiabatic[h]
HMIN	−18.64	−18.48	−0.02	0.00	0.02	−18.49	0.42	−18.07
TS1'	−17.92	−17.76	−0.04	−0.02	0.02	−17.79	0.33	−17.45
TS1"	−17.11	−16.93	0.01	−0.02	0.14	−16.81	−1.93	−18.74
MIN1'	−19.49	−19.36	−0.02	0.04	0.32	−19.03	0.33	−18.70
MIN1"	−20.80	−20.69	−0.03	0.04	0.32	−20.35	0.53	−19.82
TS2	−10.60	−10.57	−0.06	0.06	0.41	−10.15	−0.08	−10.23
MIN2	−13.13	−13.07	−0.06	0.05	0.35	−12.73	0.56	−12.16
CH_2I^- +H_2O	−1.96	−2.08	−0.07	0.11	0.56	−1.49	−1.33	−2.82

[a] CCSD(T)-F12b/aug-cc-pVTZ. [b] Eq. (4.1). [c] Eq. (4.2). [d] Eq. (4.3). [e] Eq. (4.4). [f] Eq. (4.5) [g] ΔZPE(CCSD(T)-F12b/aug-cc-pVTZ). [h] Eq. (4.5) + ΔZPE.

The post-CCSD(T) corrections are almost negligible reaching a cumulative value of −0.06 kcal mol^{-1} for TS1', while the Δcore values are more impactful in most cases, with a maximum of 0.56 kcal mol^{-1} at the proton-abstraction products. The ZPE effects are usually between ±0.6 kcal mol^{-1}, excluding the products (−1.49 kcal mol^{-1}) and TS1" (−1.93 kcal mol^{-1}). As seen in Table 1, higher post-CCSD(T) corrections are recognized for the S_N2 pathway, notably at FSTS (−0.90 kcal mol^{-1}), whilst the Δcore corrections are compatible for the stationary points of each route.

The structures of the minima and transition states, as well as, the products and reactants of the OH^- + CH_3I S_N2 and proton-abstraction reactions depicting the most important CCSD(T)-F12b/aug-cc-pVTZ bond lengths and angles with the PES values are shown in Figure 4.23. In case of the reactants and products, the PES values are in excellent agreement with the *ab initio* data, slightly larger deviations can be observed at H_2O and CH_2I^- in consonance with the above-mentioned dissimilarity (1.62 kcal mol^{-1}) of the energetics. According to the Hammond postulate,[158] as Walden inversion is a highly exothermic reaction, the mechanism has an early-barrier (reactant-like) transition state (HTS): The C–I bond of HTS is only lengthened by 0.05 Å relative to the corresponding

equilibrium distance in CH_3I. At the S_N2 stationary points, the PES data are reasonably accurate, the differences of the bond lengths are mainly within ± 0.06 Å, but occasionally, the PES gives marginally worse values for the bond angles, for example at HTS, the O–H–I angle differs from the *ab initio* data by ~9°. It is apparent that, even for proton abstraction, the PES provides more or less decent bond lengths and angles. In respect of proton abstraction, TS2 has a C_1 symmetry, while the other stationary points belong to the C_s group. In brief, relying on its performance, the present PES is acceptable for further QCT investigation.

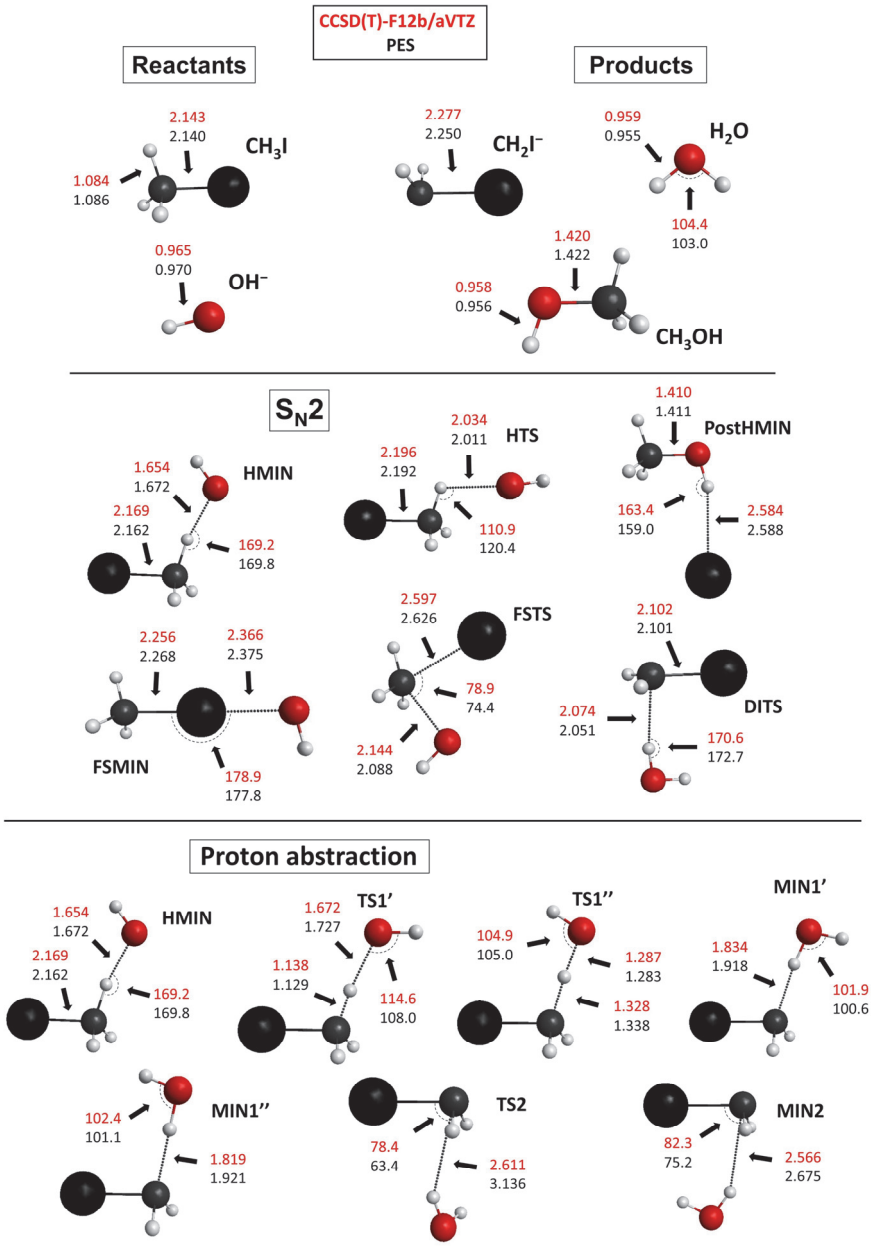

Figure 4.23 The geometries of the reactants, products and the stationary points for the $OH^- + CH_3I$ S_N2 and proton-abstraction pathways featuring the most important CCSD(T)-F12b/aug-cc-pVTZ bond lengths (Å) and angles (°) with the PES values. [1]

To describe the dynamics of the $OH^- + CH_3I$ reaction thoroughly, QCT simulations are carried out at four different E_{coll} of 11.5, 23.1, 34.6 and 46.1 kcal mol^{-1}. [1] For the details of the QCT calculations, see Section 4.2.1. Besides S_N2 and proton abstraction, numerous alternative pathways are exposed:

S_N2	$OH^- + CH_3I \rightarrow I^- + CH_3OH$	R.(2)
Proton abstraction	$OH^- + CH_3I \rightarrow H_2O + CH_2I^-$	R.(3)
S_N2 with proton exchange:	$OH'^- + CH_3I \rightarrow HOH' + CH_2I^- \rightarrow$ $OH^- + CH_2H'I \rightarrow I^- + CH_2H'OH$	R.(4)
Proton abs. with proton exchange	$OH'^- + CH_3I \rightarrow HOH' + CH_2I^- \rightarrow$ $OH^- + CH_2H'I \rightarrow HOH + CHH'I^-$	R.(5)
Proton exchange	$OH'^- + CH_3I \rightarrow HOH' + CH_2I^- \rightarrow$ $OH^- + CH_2H'I$	R.(6)
Iodine abstraction	$OH^- + CH_3I \rightarrow [I\cdots OH]^- + CH_3,$	R.(7)

as well as, in some cases, succeeding or coinciding proton abstraction, the C–I bond of CH_2I^- breaks (proton abstraction with dissociation) opening the door for the following four channels:

$$OH^- + CH_3I \rightarrow CH_2 + I^- + H_2O \quad \text{R.(8)}$$

$$OH^- + CH_3I \rightarrow H_2O + [I\cdots CH_2]^- \quad \text{R.(9)}$$

$$OH^- + CH_3I \rightarrow CH_2 + [I\cdots H_2O]^- \quad \text{R.(10)}$$

$$OH^- + CH_3I \rightarrow I^- + [CH_2\cdots H_2O]. \quad \text{R.(11)}$$

The ICSs of the possible pathways [R.(2)–R.(11)] as a function of E_{coll} are shown in Figures 4.24 and 4.25 and in Table S3. The opacity functions of the S_N2 and proton-abstraction channels are displayed in Appendix (Figure S5). Labelling the protons of the system enables us to distinguish those routes, which involve proton exchange between OH^- and CH_3I [R.(4), R.(5) and R.(6)]. Since the S_N2 and proton-abstraction paths of the $OH^- + CH_3I$ reaction are barrierless, their ICSs are decreasing with increasing E_{coll}: At 11.5, 23.1, 34.6 and 46.1 kcal mol^{-1} E_{coll}, the S_N2 ICSs are 79.0, 23.3, 13.1 and 10.4 bohr^2, in order, and the proton-abstraction ICSs are 170.0, 59.3, 32.8 and 22.2 bohr^2,

respectively. Soft and hard restrictions are used for the channels of S_N2 and proton abstraction, natheless, in the matter of S_N2, being highly exothermic, these constraints are non-effective. Despite that, considering soft constraints, the ICSs of proton abstraction drop to 100.0, 40.1, 23.7 and 16.5 bohr^2 at E_{coll} = 11.5, 23.1, 34.6 and 46.1 kcal mol^{-1}, while the proton-abstraction ICSs suffer a major decline by the impact of the hard ZPE restriction (23.9, 14.8, 10.5 and 8.0 bohr^2, in the same order).

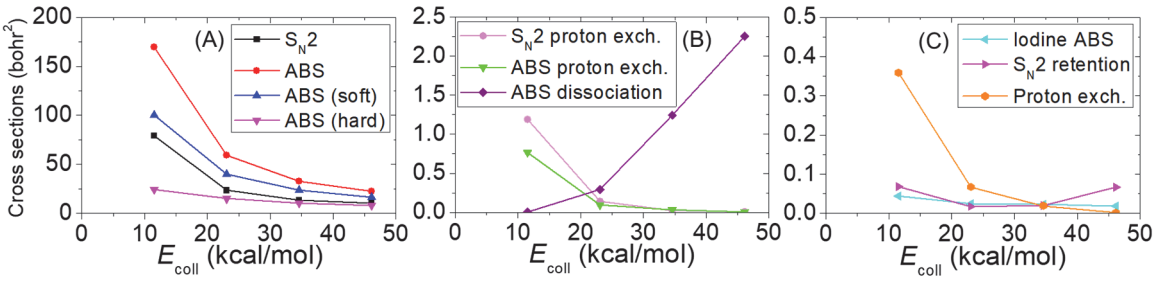

Figure 4.24 Integral cross sections of the possible pathways of the OH^- + CH_3I reaction for collision energies of 11.5, 23.1, 34.6 and 46.1 kcal mol^{-1}: (A) S_N2, proton abstraction with soft and hard restriction; (B) S_N2 with proton exchange, proton abstraction with proton exchange and proton abstraction with dissociation; and (C) iodine abstraction, S_N2 with retention and proton exchange. Note that the ICS of proton abstraction with dissociation is the sum of the ICSs of the four channels introduced in R.(8)–(11). (Taken from ref. [1].)

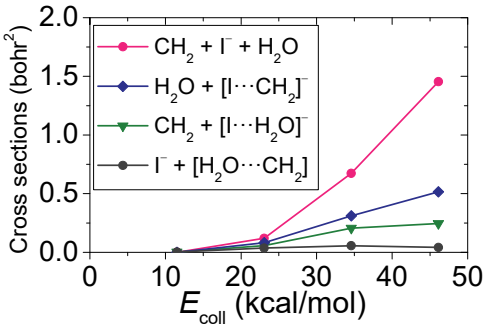

Figure 4.25 Integral cross sections of the four channels [R.(8)–(11)] of the proton abstraction with dissociation pathway as a function of collision energy in case of the OH^- + CH_3I reaction. (Taken from ref. [1].)

The pathways of S_N2 with proton exchange and proton abstraction with proton exchange have similar ICSs at each E_{coll}: Decreasing from ~1 bohr^2 to nearly 0 bohr^2. The same tendency eventuates for proton exchange and iodine abstraction, only with smaller

ICSs, mainly at lower E_{coll}. Besides inversion of the initial CH_3I configuration, retention can also befall by double inversion at smaller E_{coll}, and by front-side attack at higher E_{coll}. The only channel increasing with E_{coll} is proton abstraction with dissociation, which can be divided into four channels [R.(8)–(11)] reaching a cumulate ICS of 2.26 bohr^2 at E_{coll} = 46.1 kcal mol^{-1}. Among the viable products of proton abstraction with dissociation, at each E_{coll}, the most probable is $CH_2 + I^- + H_2O$ [R.(8)], whilst the least possible is $I^- + [CH_2 \cdots H_2O]$ [R.(11)].

As discussed in Introduction, in the direct dynamics simulations performed by Xie *et al.*,[37] four final products ($CH_3OH + I^-$, $CH_2I^- + H_2O$, $CH_2 + I^- + H_2O$ and $IOH^- + CH_3$), and a $[CH_3 \cdots I \cdots OH]^-$ intermediate were observed. Their ICSs of the S_N2 and proton abstraction routes qualitatively agree with our QCT results: ICSs of 58.9, 38.9 and 15.4 bohr^2 for S_N2 and of 135.0, 64.6 and 31.4 bohr^2 for proton abstraction are determined at E_{coll} = 11.5, 23.1 and 46.1 kcal mol^{-1}, respectively.

The $OH^- + CH_3I$ reaction were examined by Wester and co-workers using crossed-beam ion-imaging technique at E_{coll} = 11.5, 23.1, 34.6 and 46.1 kcal mol^{-1}. These experiments introduced by Wester and co-workers enable us to investigate the dynamics of gas-phase ion–molecule reactions.[9,159,160] In the $OH^- + CH_3I$ case,[40] the generation of OH^- was implemented in a pulsed plasma discharge (a mixture of 10% NH_3 in 90% Ar, bubbled through a 30% ammonia solution), then involving a mass selection procedure by time-of-flight, the ions were kept in an octupole radio-frequency trap at ~100 K. Subsequently, the OH^- beam was crossed with a supersonic laser jet of CH_3I seeded in He. A position- and time-sensitive detector system were employed, and the derived information was converted into a product mass and velocity vector in the centre-of-mass frame.[161] The energy and angular distributions were acquired from the three-dimensional velocity distributions by performing numerical integration. In the course of a recent review of the data, a miscalculation was noticed at the determination of the relative translational energy distributions, which has been corrected in ref. [1].

The experimental and theoretical (QCT and direct dynamics) branching ratios of the products ions are given in Table 10. Experimentally, the ions of I^-, CH_2I^- and $[I \cdots H_2O]^-/[I \cdots OH]^-$ can be detected. The time-of-flight apexes of $[I \cdots H_2O]^-$ and $[I \cdots OH]^-$ overlie, due to the nearly equivalent masses, ergo these product ions cannot be precisely distinguished from each other. Thus, for the QCT branching ratio, the $[I \cdots H_2O]^-$ and $[I \cdots OH]^-$ ions are considered, which are produced in R.(10) and R.(7). Note that the $[I \cdots CH_2]^-$ ion is not taken into account for the QCT branching ratios, because it is not

clear whether the product is detected as I^- or CH_2I^- by the crossed-beam technique. Moreover, the QCT ratio of CH_2I^- is calculated based on the ICS of the soft-restricted proton abstraction.

Table 10. The experimental and theoretical (QCT and direct dynamics computations) branching ratios (%) of the I^-, CH_2I^- and $[I\cdots H_2O]^-/[I\cdots OH]^-$ product ions for the $OH^- + CH_3I$ reaction at different collision energies. Note that, for the QCT branching ratios, the soft ZPE-constrained proton abstraction is considered.[a]

E_{coll} (kcal mol^{-1})	I^-			CH_2I^-			$[I\cdots H_2O]^-/[I\cdots OH]^-$		
	exp.	direct dyn.	QCT[b]	exp.	direct dyn.	QCT[c]	exp.[d]	direct dyn.[e]	QCT[f]
11.5	45.4	30.3	44.0	53.8	69.5	55.8	0.8	0	>0.0
23.1	32.5	37.8	36.8	66.7	61.9	62.8	0.8	>0.0	0.1
34.6	36.5	–	36.3	62.0	–	62.2	1.5	–	0.6
46.1	40.5	36.4	40.7	56.9	62.8	56.6	2.6	>0.0	0.9

[a] For the QCT branching ratios, the total reactive cross sections (100%) = ICS_{SN2} + $ICS_{ABS\ soft}$ + $ICS_{ABS\ dissociation}$ + $ICS_{Iodine\ ABS}$ + $ICS_{Proton\ exch.}$, and the results are adopted from ref. [1]. For direct dynamics calculations 100% = ICS_{SN2} + ICS_{ABS} + $ICS_{ABS\ dissociation}$ + $ICS_{Iodine\ ABS}$ + $ICS_{[CH_3\cdots I\cdots OH]^-}$, and the data are taken from ref. 37.

[b] I^- originates from S_N2 [R.(2)], and from two channels of the proton abstraction with dissociation leading to $CH_2 + I^- + H_2O$ [R.(8)] or $I^- + [CH_2\cdots H_2O]$ [R.(11)].

[c] CH_2I^- corresponds to the soft-restricted proton abstraction.

[d] The $[I\cdots H_2O]^-$ and $[I\cdots OH]^-$ ions cannot be separated from each other experimentally.

[e] Direct dynamics simulations revealed only the $[I\cdots OH]^-$ product ions.

[f] The sum of the branching ratios of the $[I\cdots H_2O]^-$ and $[I\cdots OH]^-$ product ions. $[I\cdots H_2O]^-$ is generated in R.(10), while $[I\cdots OH]^-$ is produced in R.(7).

The I^- and CH_2I^- QCT branching ratios are in excellent agreement with the experimental data at higher E_{coll} with deviations below ~0.3 %. On the other hand, the differences for the $[I\cdots H_2O]^-/[I\cdots OH]^-$ products are slightly notable at E_{coll} of 34.6 and 46.1 kcal mol^{-1} (0.9 and 1.7 %, in order). At E_{coll} = 11.5 kcal mol^{-1}, the QCT ratio of I^- underestimates the experimental value by 1.4 %, while at E_{coll} = 23.1 kcal mol^{-1}, the measured I^- ratio is below that of QCT by 4.3 %. Regarding CH_2I^-, at E_{coll} = 11.5 kcal mol^{-1}, the QCT data is above the crossed-beam ratio by 2.0 %, however at E_{coll} = 23.1 kcal, QCT underestimates the proportion of the CH_2I^- ions by 3.9 %. The inaccurateness of the direct dynamics simulation is clear, at E_{coll} of 11.5 kcal mol^{-1}, the estimated I^- and CH_2I^- ratios are lower than the corresponding measured values by an enormous percentage of 15.1 and 13.7, respectively. On the contrary, for higher E_{coll} of 23.1 and

46.1 kcal mol^{-1} relatively smaller discrepancies can be discerned: 5.3 and 4.1 % (I^-); 5.8 and 5.9 % (CH_2I^-). It should also be pointed out that, at each E_{coll}, the direct dynamics probability of the $[I\cdots OH]^-$ generation is almost zero, while QCT predicts a more reliable ratio with reference to experiment.

For the $OH^- + CH_3I$ reaction, the experimental and QCT internal energy distributions of the S_N2 and proton-abstraction products at each E_{coll} are illustrated in Figure 4.26.

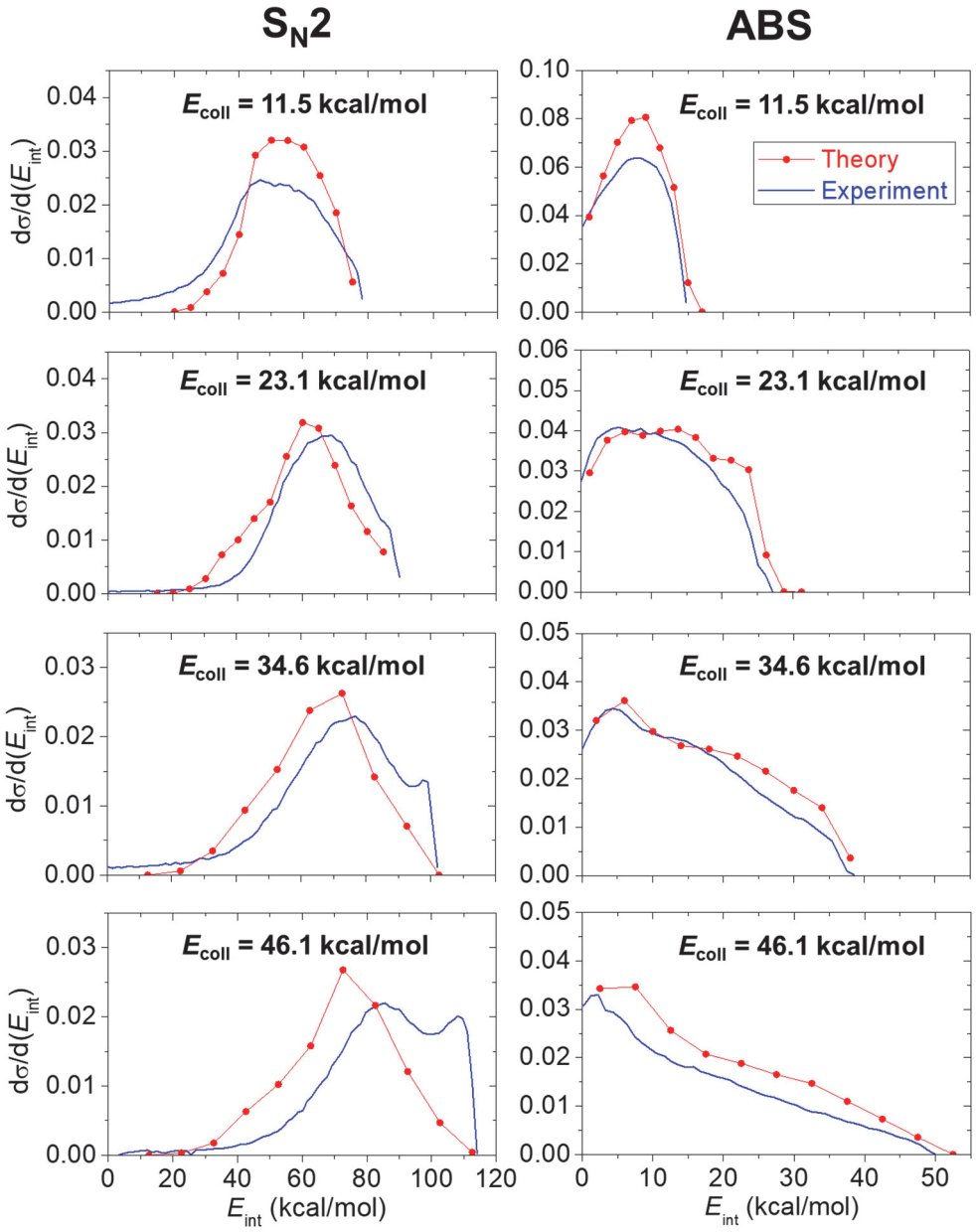

Figure 4.26 Experimental internal energy distributions of the products of the S_N2 (CH_3OH) and proton-abstraction ($CH_2I^- + H_2O$) channels for the $OH^- + CH_3I$ reaction compared to the theoretical (ZPE-corrected) distributions obtained by quasi-classical trajectory simulations at the studied collision energies. (Taken from ref. [1].)

The experimental and QCT normalized scattering angle distributions of the products of the $OH^- + CH_3I$ S_N2 and proton-abstraction reactions are given in Figure 4.27.

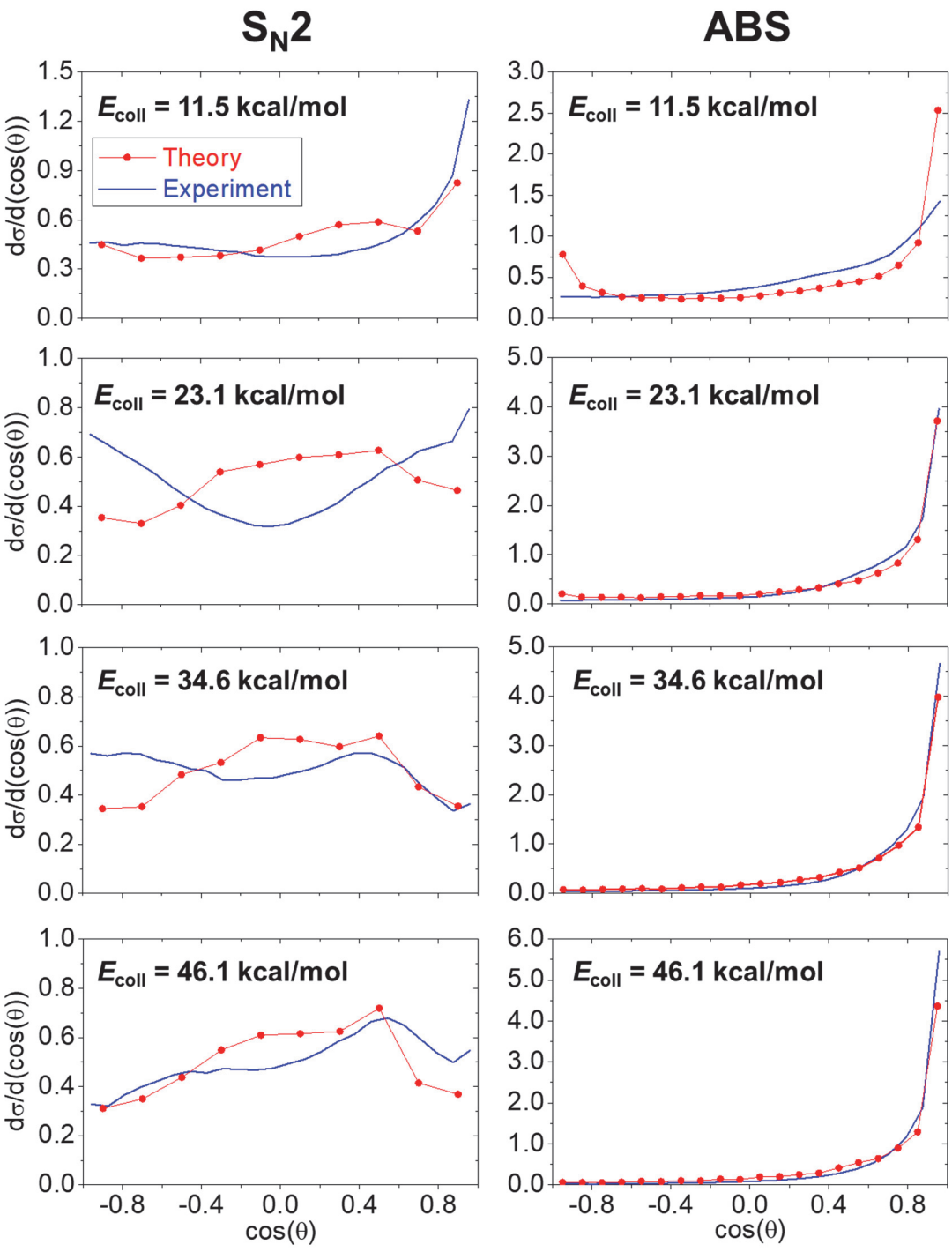

Figure 4.27 Experimental normalized scattering angle distributions of the products of the S_N2 (I^- + CH_3OH) and proton-abstraction (CH_2I^- + H_2O) channels for the OH^- + CH_3I reaction compared to the theoretical (ZPE-corrected) distributions obtained by quasi-classical trajectory simulations at the studied collision energies. (Taken from ref. [1].)

For the proton-abstraction products of $OH^- + CH_3I$, the QCT internal energy distributions are presented in Figure 4.28, and the QCT product relative translational energy distributions of S_N2 and proton abstraction are demonstrated in Figure 4.29.

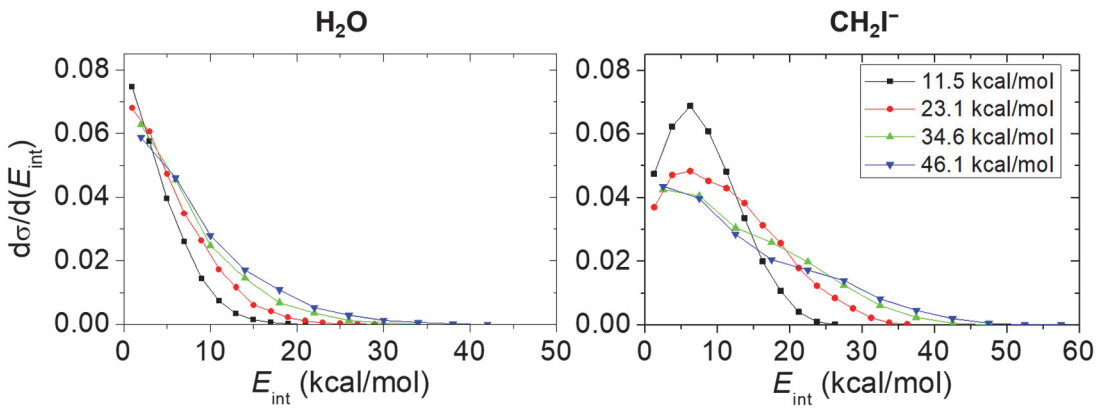

Figure 4.28 The ZPE-corrected internal energy distributions determined by quasi-classical trajectory calculations of the products of the proton-abstraction channel (H_2O and CH_2I^-) for the $OH^- + CH_3I$ reaction at different collision energies. (Taken from ref. [1].)

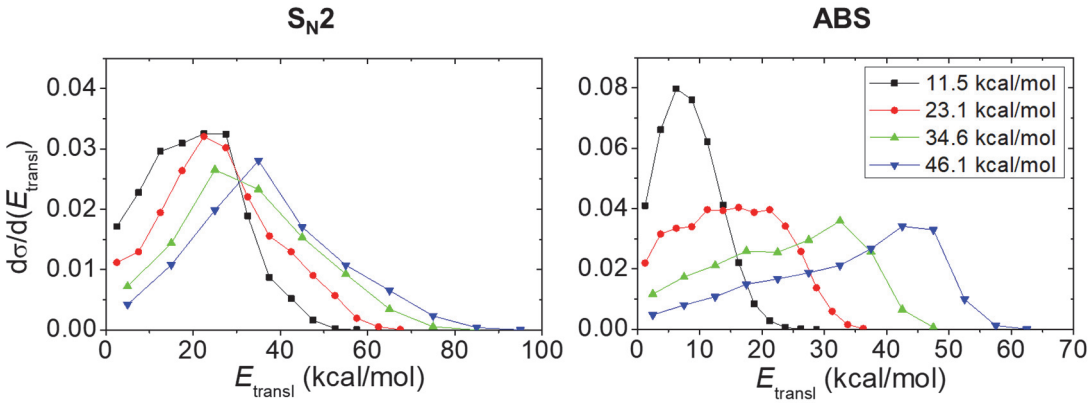

Figure 4.29 Theoretical relative translational energy distributions of the products of the S_N2 ($CH_3OH + I^-$) and proton-abstraction ($CH_2I^- + H_2O$) channels of the $OH^- + CH_3I$ reaction at different collision energies. (Taken from ref. [1].)

In case of S_N2, a comparably good agreement can be observed between experiment and theory, however, at 34.6 and 46.1 kcal mol^{-1} E_{coll}, simulations do not show a double-peaked profile as experiment does, and at 23.1 kcal mol^{-1}, the theoretical scattering angle distributions of CH_3OH have an isotropic character, while the measured distributions display a twofold forward-backward preference. Based on the product internal and relative translational energy, as well as the scattering angle distributions, the

$OH^- + CH_3I$ S_N2 may proceed *via* a variety of mechanisms: As E_{coll} increases, the internal energy is more effected than translational energy, signifying an indirect feature, while at lower E_{coll}, the forward and backward scattering of the products suggest the presence of direct stripping and rebound mechanisms, furthermore, at higher E_{coll}, the isotropic scattering implies indirect pathways involving complex formations (ion-dipole, hydrogen-bonded and front-side). Concerning the internal and scattering energy distributions of the $CH_2I^- + H_2O$ proton-abstraction products, a pleasant agreement can be recognized between experiment and theory. Upon increasing E_{coll}, the translation energy of the products is more impacted than internal energy, and as the prevalence of forward scattering is increasing steeply, the distributions of the scattering angle show an unambiguous dominance of the direct stripping mechanism in the examined range of E_{coll}. The direct dynamics study reported by Xie and co-workers did not give a similar picture for the tendencies of the corresponding product energy distributions, moreover, they revealed forward-scattered products for proton abstraction and S_N2 as well, predicting a domination of the direct pathways erroneously for all E_{coll}.[37]

4.4 Dynamical investigation of the $OH^- + CH_3F$ reaction: Introducing the oxide ion substitution

The benchmark relative classical energies of the S_N2 stationary points of $OH^- + CH_3F$ derived from Eq. (4.5) together with the PES values are shown in Figure 4.30. [4] The details of the PES development are presented in Section 4.2.1. The $OH^- + CH_3F$ S_N2 channel is less exothermic (−19.97 kcal mol^{-1}) than that of $OH^- + CH_3I$ (−66.64 kcal mol^{-1}), and withal, the proton-abstraction path is endothermic (21.62 kcal mol^{-1}). Additional structures are discovered for the transition state of front-side attack (FSTS2) and for the minimum in the exit channel (PostHMIN1'). FSTS2 is more stable than FSTS1, by ~8 kcal mol^{-1}, and PostHMIN1 remains the global minimum of the reaction. The accuracy of the PES is pleasant, the discrepancies are mostly within chemical accuracy, except for FSTS2 (1.11 kcal mol^{-1}) and the proton-abstraction products (1.61 kcal mol^{-1}). As mentioned in Section 4.1.1, a distinct H-bonded $F^-\cdots HCH_2OH$ minimum (PostHMIN2) is located in the product channel with a classical energy of −29.06 kcal mol^{-1}. In respect of proton abstraction, two minima are found at MP2/aug-cc-pVDZ (see Figure S6 in Appendix).

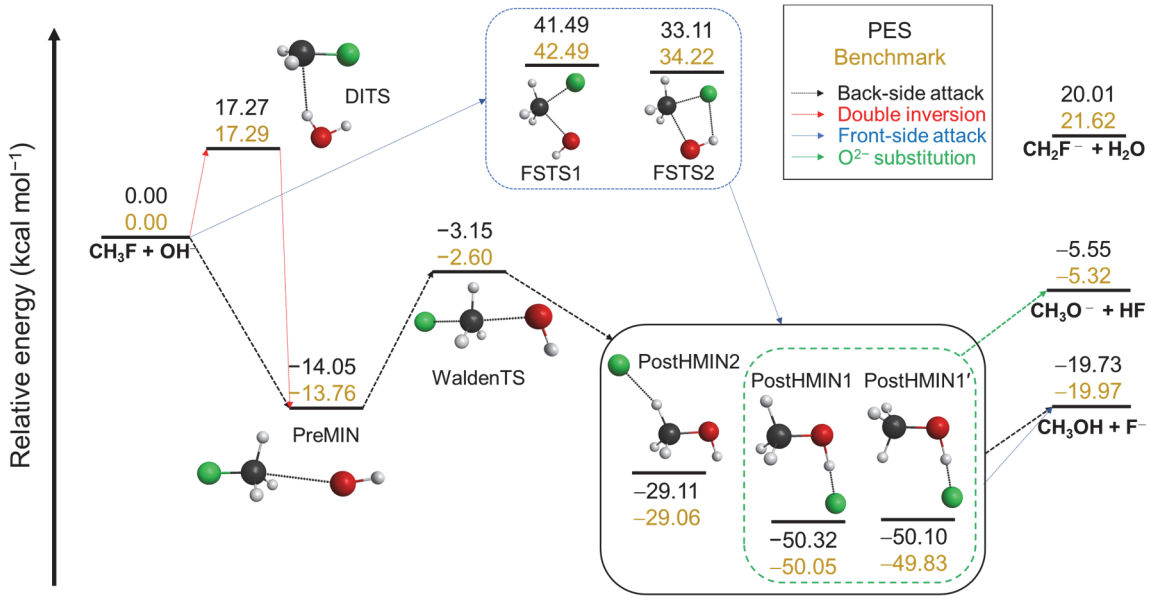

Figure 4.30 The schematic potential energy surface of the $OH^- + CH_3F$ S_N2 reaction showing the benchmark relative classical energies of the stationary points (kcal mol^{-1}) obtained from Eq. (4.5) along with the corresponding PES values for the possible mechanisms. (Taken from ref. [4].)

In the course of the PES development, besides S_N2 and proton abstraction ($F^- + CH_3OH$ and $H_2O + CH_2F^-$), the products of HF and CH_3O^- are found uncovering a novel pathway. The key steps of a representative trajectory of that unexpected reaction are depicted in Figure 4.31 showing the *ab initio* energies and the PES values of the relevant region. Firstly, the traditional Walden inversion takes place *via* WaldenTS, then the system gets trapped in the region of the H-bonded PostHMIN1 global minimum for more than 2 ps. Afterwards, abruptly at ~3 ps, the fluoride ion removes the proton from the hydroxyl group of CH_3OH leading to HF and CH_3O^-. Since in the reaction ($OH^- + CH_3F \rightarrow HF$ and CH_3O^-), the F^- of CH_3F is substituted with an O^{2-}, we name this process as oxide ion substitution. Moreover, this novel reaction path, turns out to be exothermic with a reaction energy of −5.32 kcal mol^{-1} (Figure 4.30). As seen in Figure 4.31, the *ab initio* energies computed as Eq. (4.9) are in good agreement with the PES values validating the reliability of our PES and confirming the existence of this novel mechanism. For the complete reaction path, the comparison of the corresponding potential energies is illustrated in Figure S7.

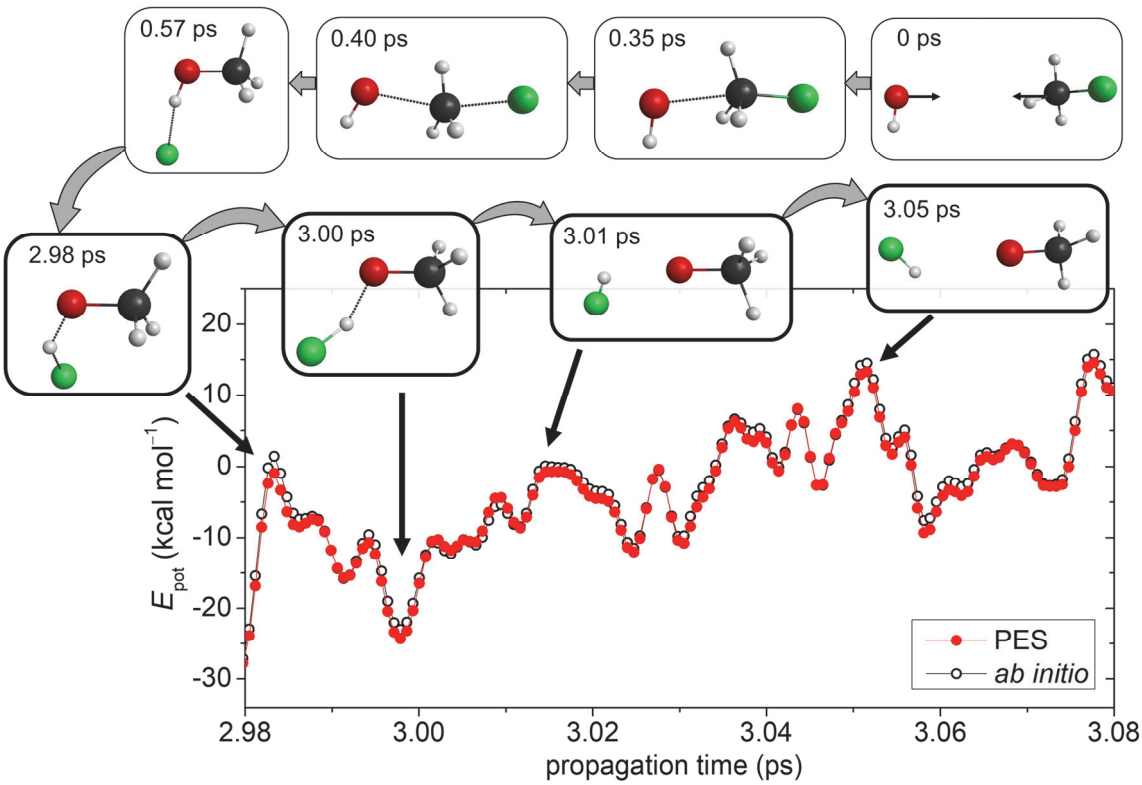

Figure 4.31 A sample trajectory of the oxide ion substitution for the OH^- + CH_3F reaction at collision energy of 10 kcal mol^{-1}. With regard to the proton abstraction by the F^-, the direct *ab initio* energies obtained from Eq. (4.9) and the PES values are shown as a function of time. (Taken from ref. [4].)

At the range of E_{coll} = 5 – 80 kcal mol^{-1}, dynamics simulations are carried out for the OH^- + CH_3F reaction using the QCT method. [4] For details see Section 4.2.1. The ICSs of the possible channels as a function of E_{coll} are displayed in Figure 4.32. Performing direct dynamics simulations for the OH^- + CH_3F reaction, Hase and co-workers unveiled that the ~90% of the trajectories avoid the deep $CH_3OH\cdots F^-$ minimum in the product channel.[24] Motivated by that study, within S_N2, we distinguish trajectories occurring through that deep well (S_N2 *via* PostHMIN) based on the methodology developed to separate the double-inversion and front-side attack retention pathways.[129] By tracking the relevant atomic distances backwards from the end of the S_N2 trajectories, those are selected for S_N2 *via* PostHMIN, where the corresponding distances of hydroxyl-H−F and hydroxyl-H−O are less than 1.8 Å and 2.5 Å, respectively, as well as, the C−F distance is longer than the C−O distance. Analogously to OH^- + CH_3I, proton exchange reaction can also be found resulting products apparently identical to the reactants. The most prevalent channel is S_N2, its ICS has a maximum of 5.2 bohr^2 at E_{coll} = 10 kcal mol^{-1},

shrinking to ~4 bohr^2 at higher E_{coll}. Proton abstraction is endothermic, regardless, below E_{coll} of 20 kcal mol^{-1}, proton abstraction is feasible owing to the ZPE violations of the products. It is important to note that ZPE restrictions are not applied for $OH^- + CH_3F$ proton abstraction, and no ZPE-leakage error can be observed for S_N2. At E_{coll} = 5 kcal mol^{-1}, the ICS of proton exchange is nearly as large as that of S_N2, baring a difference of 0.9 bohr^2, and as E_{coll} increases, the proton-exchange ICS decreases. The same holds for the S_N2 *via* postHMIN1 and oxide ion substitution pathways peaking with ICSs of 0.9 and 0.1 bohr^2 at E_{coll} = 5 kcal mol^{-1}.

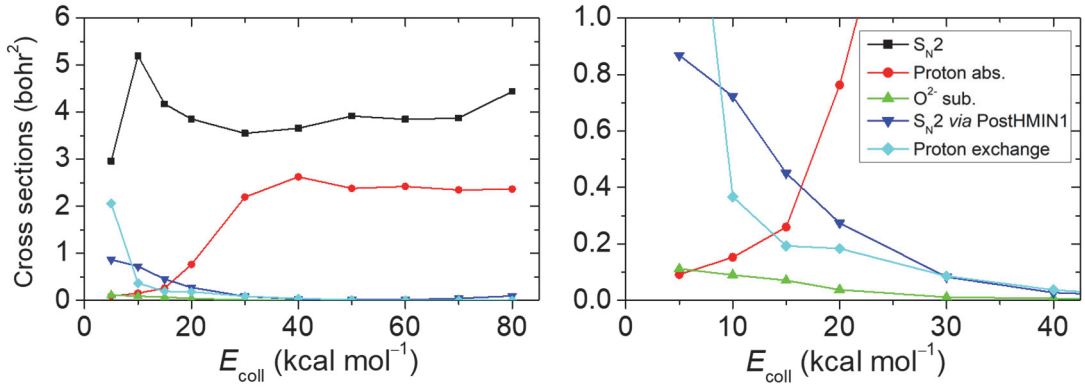

Figure 4.32 Integral cross sections of the channels of S_N2, proton abstraction, oxide ion substitution, S_N2 *via* postHMIN1 and proton exchange as a function of collision energy for the $OH^- + CH_3F$ reaction. (Taken from ref. [4].)

For the products of S_N2, proton abstraction and oxide ion substitution, the internal and relative translational energy distributions at selected E_{coll} are shown in Figures 4.33–4.35.

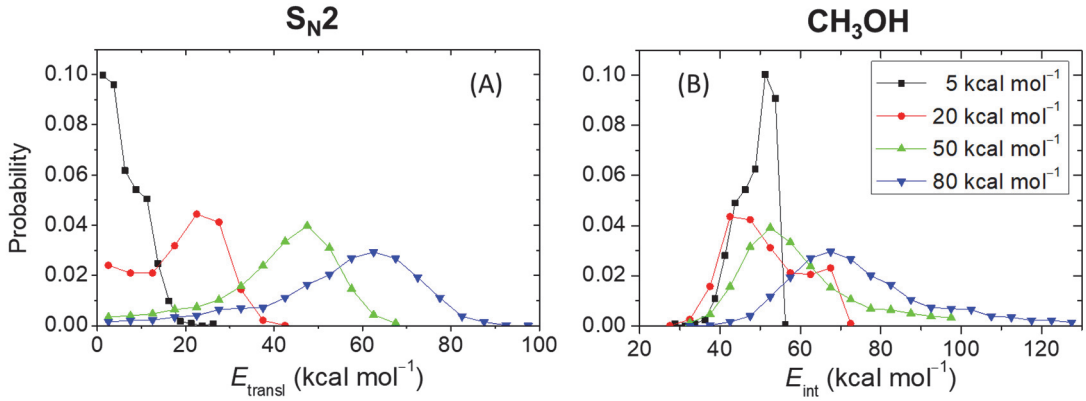

Figure 4.33 (A) Relative translational and (B) internal energy distributions of the S_N2 products for the $OH^- + CH_3F$ reaction at various collision energies of 5, 20, 50 and 80 kcal mol^{-1}. (Taken from ref. [4].)

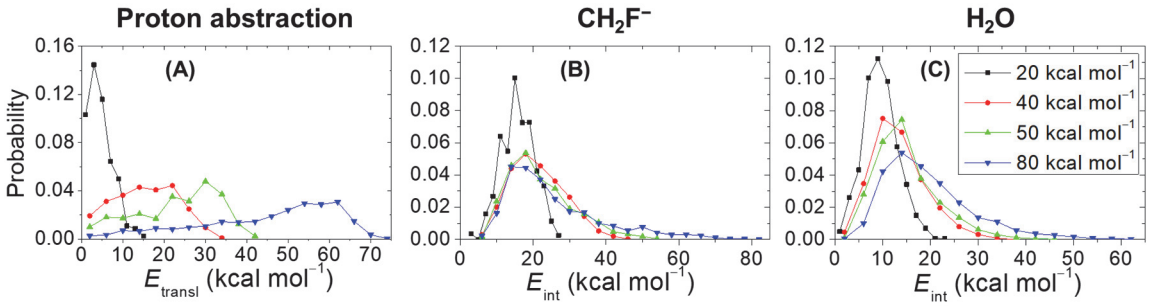

Figure 4.34 (A) Relative translational energy distributions of the products and the internal energy distributions of (B) CH_2F^- and (C) H_2O in case of OH^- + CH_3F proton-abstraction reaction at collision energies of 20, 40, 50 and 80 kcal mol^{-1}. (Taken from ref. [4].)

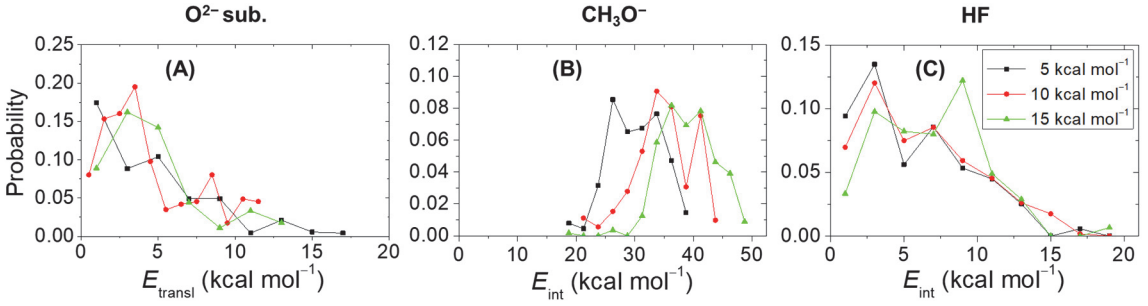

Figure 4.35 (A) Relative translational energy distributions of the products, and the internal energy distributions of the (B) CH_3O^- and (C) HF products for the novel oxide ion substitution of OH^- + CH_3F at collision energies of 5, 10 and 15 kcal mol^{-1}. (Taken from ref. [4].)

For S_N2 and proton abstraction, with increasing E_{coll}, the product translational energy is more impacted than internal energy signifying a dominance of the direct reaction mechanisms at higher E_{coll}. This finding is in consonance with the decrease of the ICS value of S_N2 *via* PostHMIN1: The more pronounced the direct character of S_N2, the more likely that the trajectory avoids PostHMIN1 in the product channel. As it can also be seen in Figure 4.35, at higher E_{coll}, the product internal energy of oxide ion substitution is more influenced than the translational energy identifying an indirect preference. In most cases, the system is entrapped in the region of the PostHMIN1, howbeit, occasionally ion-dipole (PreMIN) complex formation, as well as, short-term entrapment in the PostHMIN1 well can be observed. The lifetime of the PostHMIN1 global minimum for the OH^- + CH_3F oxide ion substitution in the ranges of E_{coll} = 5–15 kcal mol^{-1} and b = 0–3 bohr is given in Table 11.

Table 11. The average time (ps) that the trajectories trap into the postHMIN1 complex well at impact parameters of 0 – 3 bohr and collision energies of 5, 10 and 15 kcal mol^{-1} for the $OH^- + CH_3F \rightarrow CH_3O^- + HF$ reaction. [4]

***b* (bohr)**	E_{coll} **(kcal mol^{-1})**		
	5	**10**	**15**
0.0	2.78	3.36	1.87
0.5	2.23	2.02	0.76
1.0	5.11	3.38	2.38
1.5	5.28	1.44	1.63
2.0	1.33	2.78	1.30
2.5	5.29	3.10	1.24
3.0	3.53	1.56	0.91

The determination of the lifetime of the PostHMIN1 complex for the $OH^- + CH_3F$ oxide ion substitution path is performed as follows: Tracking the atomic distances in each trajectory from the beginning to end, the PostHMIN1 complex is designated at each time step of 0.726 fs when the appropriate conditions hold (the distances of hydroxyl-H−F and hydroxyl-H−O are less than 2.5 and 2.25 Å, the C−F distance is longer than the C−O distance, the hydroxyl-H−F distance is not the longest H−F distance and the hydroxyl-H−F distance is not greater by 0.3 Å than the shortest H−F distance). At E_{coll} = 5, 10 and 15 kcal mol^{-1}, the average lifetime of the product-channel well is 3.65, 2.52 and 1.44 ps, in order, thus, the lifetime of the PostHMIN1 deep well decreases rapidly with increasing E_{coll} confirming the gaining dominance of the direct pathways at higher E_{coll}.

For $OH^- + CH_3F$, the scattering angle distributions of the products of S_N2, proton abstraction and oxide ion substitution at several E_{coll} are depicted in Figure 4.36. According to this, similar conclusions that were earlier deduced can be reached. At all E_{coll}, S_N2 products show backward-scattering preference as a consequence of the WaldenTS penta-covalent structure, while proton abstraction results in forward scattered products, affirming the prevalence of the direct mechanisms of rebound (S_N2) and stripping (proton abstraction). It should be also noted, at E_{coll} below reaction enthalpy, the ZPE-violated proton abstraction yields more backward scattered products. Additionally, at E_{coll} = 10 kcal mol^{-1}, the isotropic profile of oxide ion substitution verifies the promotion of the indirect reaction pathway caused by trapping in the exit-channel well.

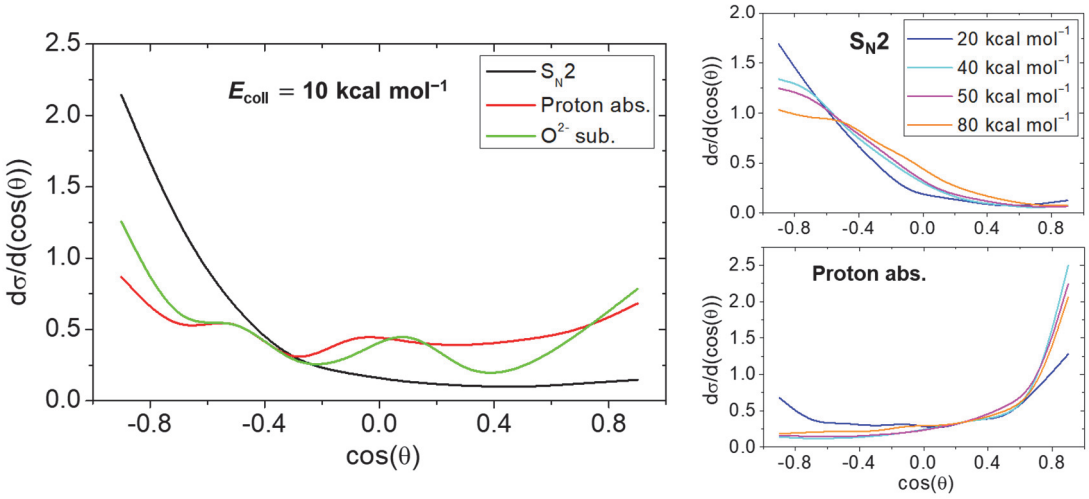

Figure 4.36 Product scattering angle distributions of the pathways of S_N2 ($F^- + CH_3OH$), proton abstraction ($H_2O + CH_2I^-$) and oxide ion substitution ($CH_3O^- + HF$) at various collision energies for the $OH^- + CH_3F$ reaction. (Taken from ref. [4].)

In 2022, based on our study of the $OH^- + CH_3F$ reaction, Li and co-workers developed a novel PES for the reaction by the PIPl neural network method and implemented a detailed dynamical characterization at E_{coll} of 1, 5, 10, 15, 20 and 30 kcal mol^{-1}, as well.[162] The *ab initio* energy points were computed at the CCSD(T)-F12a/aug-cc-pVTZ level of theory, hence, the failure of the CCSD(T) method has not been taken into consideration. Likewise, their QCT simulations of the $OH^- + CH_3F$ reaction uncovered the novel oxide ion substitution, as well. For proton exchange and proton abstraction, a novel transition state and a H-bonded complex were found, respectively, however, it was unveiled that the trajectories also avoid these regions of the PES.

The ICSs provided by Li *et al*. (denoted by *) in comparison with our results at E_{coll} = 5, 10, 15, 20 and 30 kcal mol^{-1} are presented in Table 12.[162] The ICS values are in a good agreement, although, notable deviations (2.04 and 0.45 bohr^2) can be found for S_N2 and S_N2 *via* PostHMIN1 at E_{coll} = 5 kcal mol^{-1}. Despite that, the probability of that S_N2 which avoids the PostHMIN1 well is approximately equivalent in both cases. Noteworthy that taking into account the ZPE constraints, oxide ion substitution is still attainable with smaller ICSs. Li and co-workers reported ICSs of 0.05, 0.10, 0.11, 0.08 and 0.04 bohr^2 for the soft-restricted oxide ion substitution at E_{coll} = 5, 10, 15, 20 and 30 kcal mol^{-1}, respectively, conforming to our values of 0.08, 0.08, 0.07, 0.03 and 0.01 bohr^2, in the same order.

Table 12. The comparison of the ICSs (bohr^2) of the possible channels (S_N2, proton abstraction, S_N2 *via* PostHMIN1, oxide ion substitution and proton exchange) for the $OH^- + CH_3F$ reaction at collision energies of 5, 10, 15, 20 and 30 kcal mol^{-1}.

Reaction channels	E_{coll} (kcal mol^{-1})				
	5	**10**	**15**	**20**	**30**
S_N2[a]	2.96	5.20	4.17	3.85	3.55
S_N2*[b]	0.92	4.88	5.26	4.83	4.99
Proton abs.[a]	0.09	0.15	0.26	0.76	2.19
Proton abs.*[b]	0.02	0.11	0.21	0.57	1.87
S_N2 via PostHMIN1[a]	0.87	0.72	0.45	0.27	0.08
S_N2 via PostHMIN1*[b]	0.42	0.72	0.45	0.29	0.11
Oxide ion subs.[a]	0.11	0.09	0.07	0.04	0.01
Oxide ion subs.*[b]	0.06	0.15	0.12	0.09	0.04
Proton exchange[a]	2.06	0.37	0.19	0.18	0.09
Proton exchange*[b]	1.92	0.29	0.18	0.16	0.09
Total[a,c]	5.22	5.81	4.69	4.83	5.84
Total*[b,c]	2.92	5.33	5.77	5.65	6.99

[a] The ICS values are taken from ref. [4].
[b] The ICSs are derived from ref. 162.
[c] Total reactive cross sections = ICS_{S_N2} + $ICS_{\text{proton abs.}}$ + $ICS_{\text{oxide ion subs.}}$ + $ICS_{\text{proton exchange}}$

4.5 Alternative indirect S_N2 retention pathways for the $NH_2^- + CH_3I$ reaction

Proceeding from the previous examinations of the reactions between the OH^- diatomic nucleophile and CH_3I/CH_3F, we move towards more complex systems, and shift our focus to the $NH_2^- + CH_3I$ polyatomic reaction. [2] The details of $NH_2^- + CH_3I$ PES development are given in Section 4.2.1. As usual, firstly, the characterization of the proton-abstraction pathway must be carried out. Then, secondly, an assessment of the PES reliability must be fulfilled by comparing the benchmark relative energies of the S_N2 and proton-abstraction stationary points with the values obtained by geometry optimizations on the PES (see Figure 4.37).

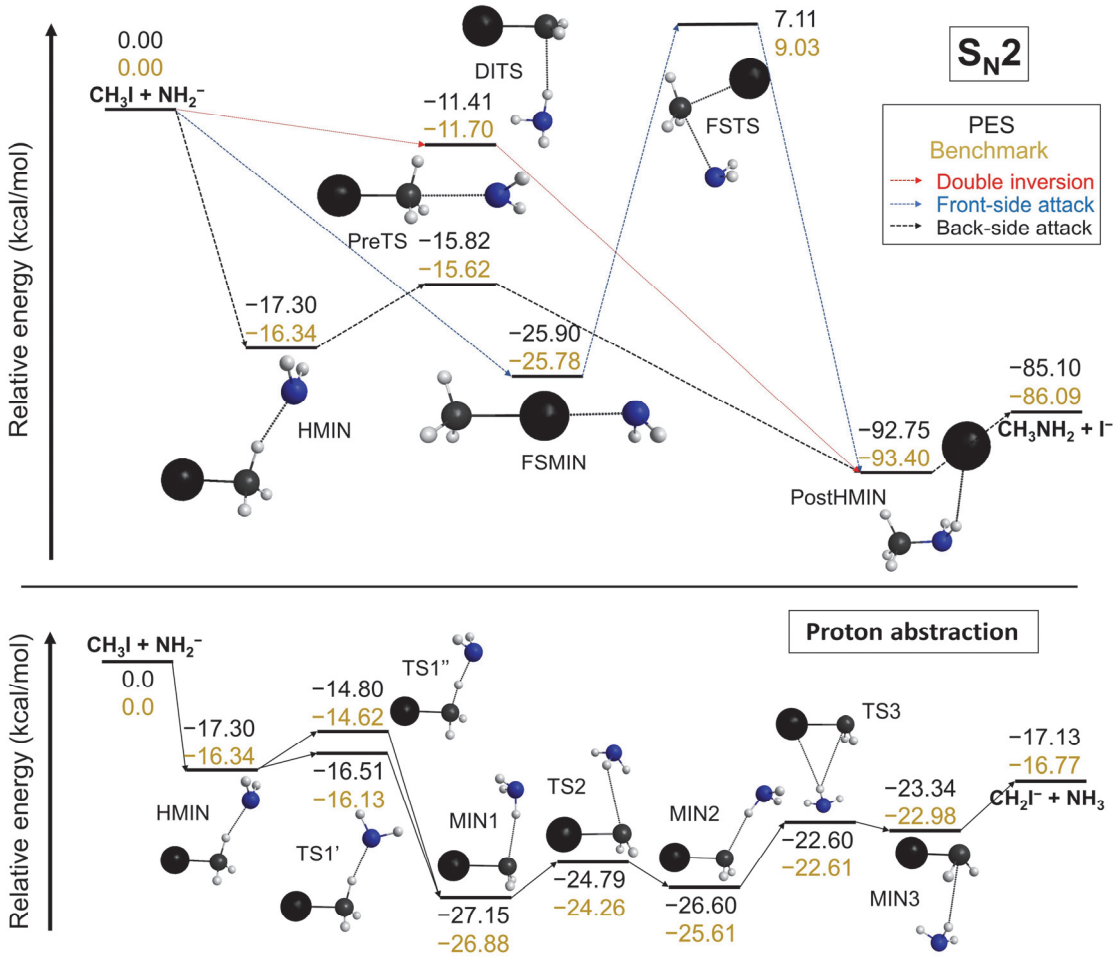

Figure 4.37 The schematic representations of the potential energy surfaces of the $NH_2^- + CH_3I$ S_N2 and proton-abstraction channels showing the benchmark classical relative energies obtained from Eq. (4.1) with the corresponding PES values along the possible pathways. (Taken from ref. [2].)

In the matter of proton abstraction, building upon the $OH^- + CH_3I$ case (see Figure 4.22), three additional minima and four transition states can be identified. S_N2 is remarkably more exothermic than proton abstraction, submerged by a classical energy of 69.32 kcal mol^{-1}. Among the four transition states of proton abstraction, the smallest barrier height belongs to TS1' (less than ~0.22 kcal mol^{-1}). The global minimum of the S_N2 channel is shallow: the dissociation energy of PostHMIN is only 7.31 kcal mol^{-1}, as opposed to this, for $OH^- + CH_3F$, this value is 30.08 kcal mol^{-1}. FSMIN is below HMIN by 9.44 kcal mol^{-1} indicating a prominent role of the front-side attachment. The energies provided by the PES are in accord with the benchmark data, except at FSTS, where a larger disparity of 1.92 kcal mol^{-1} becomes apparent.

In case of $NH_2^- + CH_3I$, we run QCT simulations at E_{coll} = 5, 10, 20 and 30 kcal mol^{-1}. [2] The conditions of the QCT calculations are described in Section 4.2.1. The ICSs of the possible pathways at the studied E_{coll} are given in Figure 4.38. ZPE constraints are also applied for proton abstraction and S_N2, whereas, the restrictions have no effect on the latter path.

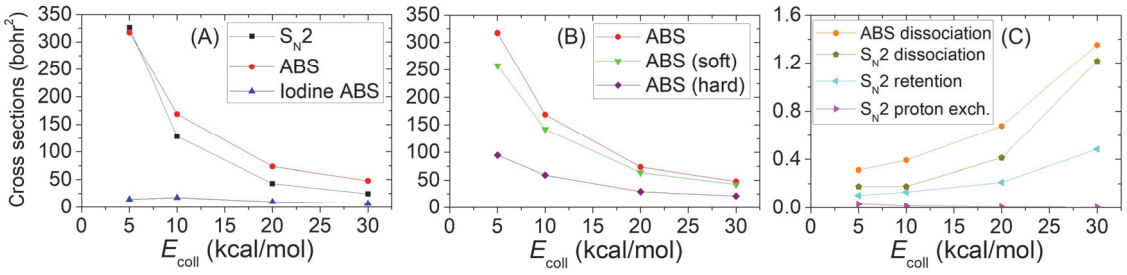

Figure 4.38 The integral cross sections of the possible channels [(A) S_N2, proton abstraction, iodine abstraction; (B) proton abstraction with soft and hard ZPE restrictions; (C) proton abstraction with dissociation, S_N2 with dissociation, S_N2 retention and S_N2 with proton exchange] as a function of collision energy for the $NH_2^- + CH_3I$ reaction. (Taken from ref. [2].)

The same pathways as those observed for the $OH^- + CH_3I$ reaction [R.(2)–(11)] can be found in the present case of $NH_2^- + CH_3I$, and the dependence of their ICS values on the E_{coll} is also comparable. At E_{coll} =5 kcal mol^{-1}, S_N2 has the largest ICS (326.3 bohr^2), while at higher E_{coll} of 10, 20 and 30 kcal mol^{-1}, proton abstraction is the most significant channel with ICSs of 168.9., 73.5 and 47.8 bohr^2, respectively. Considering ZPE violation, the ICS of the hard-constrained proton abstraction notably drops to 94.7, 59.0, 29.3 and 21.2 bohr^2, at E_{coll} = 5, 10, 20 and 30 kcal mol^{-1}, in order, while the soft ZPE restriction has a less pronounced impact as its ICSs are 257.4, 142.2, 63.8 and 42.3 bohr^2, respectively. Substantial iodine abstraction is revealed, and with raising E_{coll}, the relative dominance of this pathway shows an increasing trend. Regarding the low-probability channels, their ICSs are in the rage of 0.03–1.36 bohr^2, displaying an increasing shape with E_{coll}, as well as, a novel pathway, a so-called S_N2 with dissociation is exposed: Following S_N2, a dissociation of the C–N bond may take place. Evaluating the S_N2 retention channels step by step, double-inversion cannot be found, despite the fact that DITS is submerged with a classical (adiabatic) energy of −11.7 (−10.3) kcal mol^{-1}. The reason is simple: When NH_2^- removes a proton (H'^+) from CH_3I, another proton transfers back from NH_2H' to CH_2I^-, and followed by a Walden inversion, the

process results in S_N2 with proton exchange ($I^- + CH_3NHH'$) instead of double inversion. Although, two novel mechanisms (complex formation and Walden inversion with complex formation) can be identified, which generate S_N2 product of CH_3NH_2 with retention of the initial CH_3I configuration, as shown in Figure 4.39.

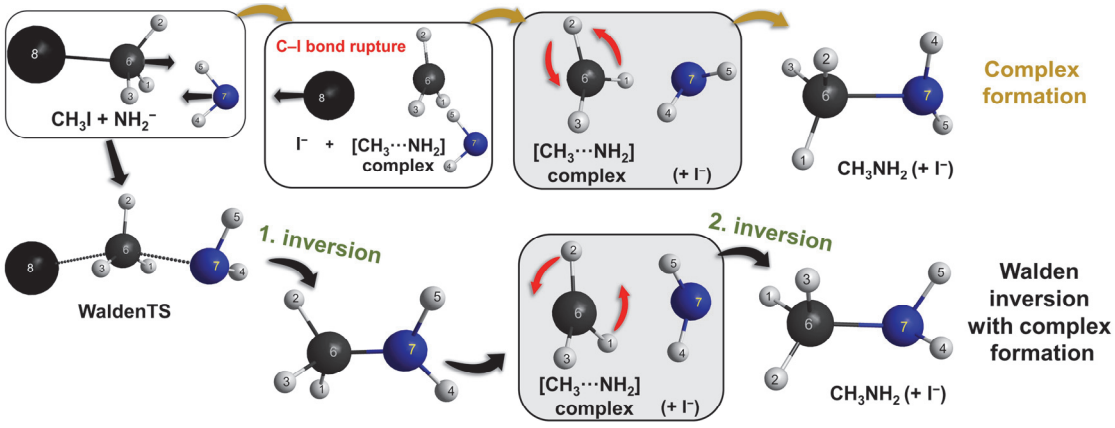

Figure 4.39. The key steps of the novel retention pathways of complex formation and Walden inversion with complex formation for the $NH_2^- + CH_3I$ reaction. Note that Walden inversion with complex formation was also revealed for the $F^- + CH_3Br$ case, however, the $[CH_3\cdots F]$ complex formation process was found to be significantly accelerated. (Taken from ref. [2].)

The key element of the unprecedented retention paths is the formation of the $[CH_3\cdots NH_2]$ complex induced by the strong long-range ion-dipole interactions of the reactants. The ICSs of the S_N2 retention pathways at $E_{coll} = 20$ and 30 kcal mol^{-1} are presented in Figure 4.40. With increasing E_{coll}, the reactants are more and more excited vibrationally prompting the formation of the $[CH_3\cdots NH_2]$ complexes, thus these unconventional pathways become more and more prevalent. In case of complex formation, as NH_2^- and CH_3I approach each other, the C–I bond breaks in CH_3I and the $[CH_3\cdots NH_2]$ complex is formed. As the translational energy converts into internal energy, these complexes are highly excited vibrationally and rotationally. A favourable relative arrangement of the fragments is needed to form the S_N2 product of CH_3NH_2, and in certain instances, retention can also take place as an outcome of the rotation of the CH_3 group. In contrast, during the alternate mechanism (Walden inversion with complex formation), two consecutive inversions lead to retention: Walden inversion generates a highly excited CH_3NH_2 product, which forms a $[CH_3\cdots NH_2]$ complex, and the second inversion resulting from the rotation of CH_3 ultimately proceeds to the final CH_3NH_2

retention products. As it can be seen in Figure 4.40, more than 90% of the S_N2 retention trajectories occur *via* the novel mechanisms of complex formation and Walden inversion with complex formation: the ICSs of complex formation is 0.13 and 0.30 bohr^2 at E_{coll} = 20 and 30 kcal mol^{-1}, while the front-side attack ICSs are only 0.01 and 0.03 bohr^2. It should be highlighted that other complexes of [$NH_2\cdots I^-$] and [$CH_2\cdots I^-$] can also be formed, in certain cases, promoting the channels of iodine abstraction and proton abstraction with rupture, in order.

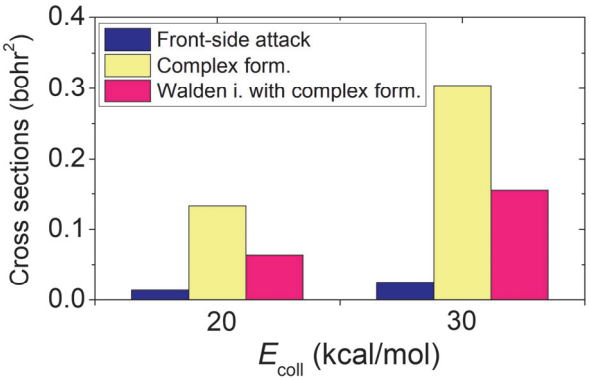

Figure 4.40 The integral cross sections of the $NH_2^- + CH_3I$ S_N2 retention pathways at collision energies of 20 and 30 kcal mol^{-1}. (Taken from ref. [2].)

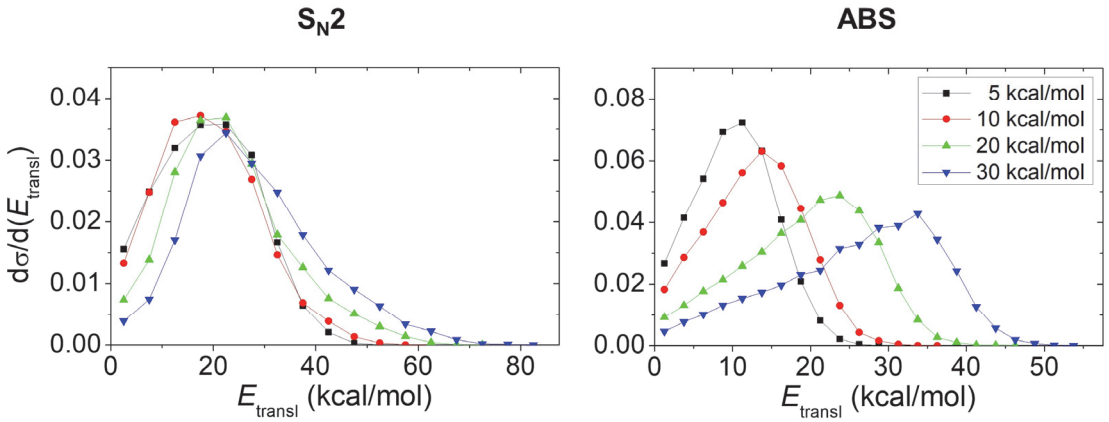

Figure 4.41 Relative translational energy distributions of the S_N2 ($I^- + CH_3NH_2$) and proton-abstraction products ($CH_2I^- + NH_3$) channels of the $NH_2^- + CH_3I$ reaction at collision energies of 5, 10, 20 and 30 kcal mol^{-1}. (Taken from ref. [2].)

To corroborate these findings, in case of the S_N2 and proton-abstraction products, the relative translational and internal energy distributions, as well as the scattering angle distributions are presented in Figures 4.41–4.43. For S_N2, as E_{coll} increases, the maxima

of the internal energy distributions shift toward higher energies, while the shape of the translational energy distributions is less affected denoting the advancement of the indirect pathways. A reversed trend is manifested by proton abstraction: The increase of E_{coll} has a more pronounced effect on the product translational energy than on the internal energy.

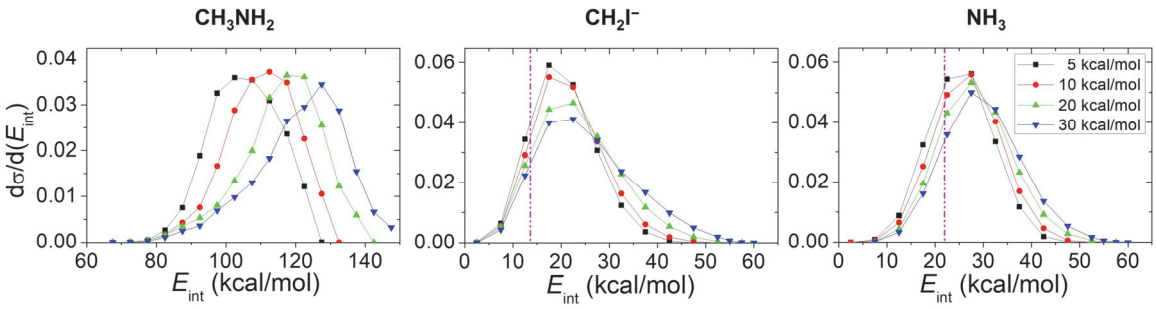

Figure 4.42 Internal energy distributions of the S_N2 ($I^- + CH_3NH_2$) and proton-abstraction products ($CH_2I^- + NH_3$) channels of the $NH_2^- + CH_3I$ reaction at collision eneriges of 5, 10, 20 and 30 kcal mol^{-1}. The purple dashed line denotes the ZPE of the corresponding product, note that the CH_3NH_2 ZPE is below 60 kcal mol^{-1} (40.6 kcal mol^{-1}). (Taken from ref. [2].)

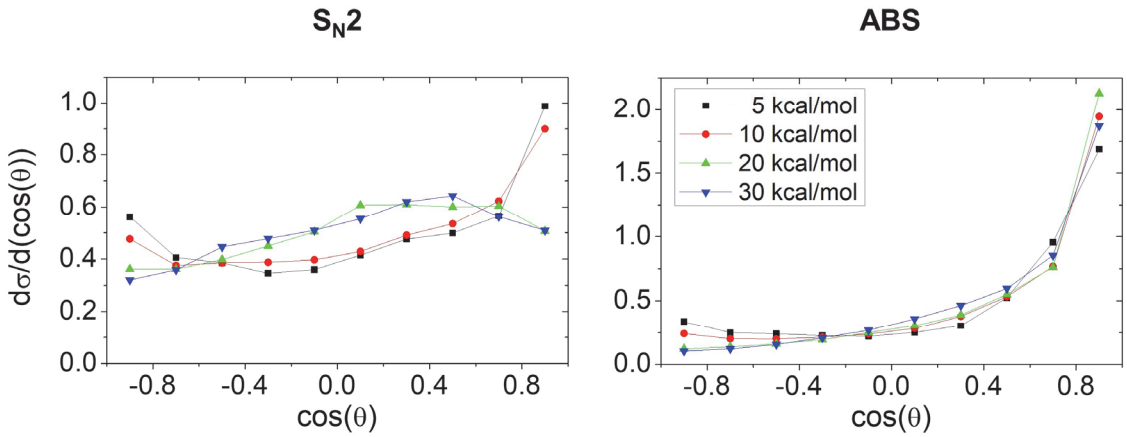

Figure 4.43 Normalized product scattering angle distributions of the pathways of S_N2 ($I^- + CH_3NH_2$), proton abstraction ($CH_2I^- + NH_3$) at various collision energies for the $NH_2^- + CH_3I$ reaction. (Taken from ref. [2].)

Similar to the $OH^- + CH_3I/CH_3F$ cases, proton abstraction results in forward-scattered products identifying the direct stripping mechanism, whilst in case of S_N2, a disparate product distribution can be observed. At low E_{coll}, the S_N2 product scattering angle distributions show a dual backward-forward preference, and as E_{coll} raises, the

profile evolves into an isotropic form bolstering the conclusion that the NH_2^- + CH_3I S_N2 route primarily takes place through indirect pathways.

In the vein of the OH^- + CH_3F oxide ion substitution, in order to substantiate the existence of these uncommon S_N2 retention mechanisms, the direct *ab initio* energies are compared with the PES values along the representative trajectories of complex formation and Walden inversion with complex formation (see Figures S8 and S9 in Appendix). The identification of these novel mechanisms is a significant step forward in understanding the complexity of S_N2 reactions and opens the door for further investigations.

5 Summary

Since the 1970s, the gas-phase S_N2 reactions have been the focus of attention and a vast amount of theoretical studies have dealt with the investigation of the possible reaction mechanisms. In the beginning, the primary objective was to investigate the traditional Walden-inversion pathway, and as theoretical methods evolved, a more intricate picture regarding the reaction mechanism has been disclosed. The application of the QCT method is among the most practical approaches for studying reaction dynamics, which requires the knowledge of the chemically relevant regions of the reaction's PES. Apart from the high-cost direct dynamics simulations, which calculate the necessary potential energies and gradients "on-the-fly" at each nuclear configuration, the PES can be represented by an analytical function, considerably increasing computational efficiency. The construction of these highly accurate PESs poses a major challenge, therefore Győri and Czakó developed the ROBOSURFER program to automate the process of the PES development. By using the in-house ROBOSURFER program, the PES development has become significantly simplified, facilitating the more efficient investigations of complex chemical systems.

The theoretical study of the $OH^-/SH^-/CN^-/NH_2^-/PH_2^- + CH_3Y$, where Y is a halogen, S_N2 reactions was the primary subject of my thesis. Utilizing the high-level explicitly-correlated CCSD(T)-F12b method with the aug-cc-pV*n*Z (*n* = 2–4) basis sets, the structures, energies and the harmonic vibrational frequencies of the stationary points of the S_N2 PESs were characterized with particular regard to the double-inversion and front-side attack mechanisms. For $OH^- + CH_3Y$, core- and post-CCSD(T) effects were also considered, and for the reactions between CN^- and CH_3F/CH_3Cl, scalar relativistic effects were determined, as well. In addition to $OH^- + CH_3Y$, the reaction of $OH^- + CH_3CH_2Y$ was also taken into account, enabling the occurrence of the competitive E2 channel. It was revealed that the S_N2 pathway of $OH^- + CH_3CH_2Y$ is thermodynamically more favoured than E2, while anti-E2 is kinetically more preferred due to the substantial ZPE effects. The energy profiles of the $OH^- + CH_3Y$ and $OH^- + CH_3CH_2Y$ S_N2 reactions are highly comparable: Submerged Walden-inversion pathway, stable front-side complex formation for Y = I, H-bonded global minimum in the exit channel, lower energy retention pathway possessed by double inversion, *etc.* Owing to the ambident nucleophilic nature of CN^-, two types of S_N2 reaction routes leading to

the $CH_3CN + Y^-$ and $CH_3NC + Y^-$ products were explored verifying that the C–C bond formation is thermodynamically, as well as, kinetically more feasible than the corresponding C−N formation. For $OH^- + CH_3CH_2Y$ and $NC^-/CN^- + CH_3Y$, numerous reaction enthalpies of other higher-level paths were also obtained. In most cases, including both the S_N2 and E2 pathways, our benchmark reaction enthalpies are in satisfactory agreement (< 1 kcal mol^{-1}) with the "experimental" data from ATcT. Among the 24 S_N2 reactions the most exothermic is $NH_2^- + CH_3I$, and the only endothermic is $SH^- + CH_3F$. The typical Walden-inversion transition states of the $NH_2^- + CH_3Br$ and $OH^-/NH_2^-/PH_2^- + CH_3I$ reactions cannot be found, although reactant-like transition states are situated in the entrance channels of the pathways. It should be also noted that generally the transition state of double inversion is below than that of front-side attack, and for $OH^- + CH_3I$ and $NH_2^- + CH_3Y$ [Y = Cl, Br and I], the barrier of double inversion disappears. In total, the thesis encompasses the benchmark characterization of more than 200 stationary points.

Global analytical PESs have been constructed for the $OH^- + CH_3I/CH_3F$ and $NH_2^- + CH_3I$ reactions using the ROBOSURFER program. In the course of the $OH^- + CH_3I$ PES development, the application of the CCSD(T)-F12b method has been found to be infeasible as it provides excessively negative energies for certain structures. To tackle this issue, the implementation of a novel composite method based on the Brueckner coupled cluster approach was proposed. The PESs are fitted by using the PIP approach with Morse-like variables. In order to obtain a more complete picture of the reactions, the stationary points of the proton abstraction channel were also explored by the corresponding high-level *ab initio* methods. QCT simulations were performed at several E_{coll} to accomplish a detailed dynamical description of the reactions.

The combination of the crossed-beam and velocity imaging techniques utilized by the Wester group, allows us to examine the ion-molecule reactions. Different S_N2 (E2) reactions, that include various nucleophiles were investigated experimentally: $F^- + CH_3Cl/CH_3I$, $Cl^- + CH_3I$, $F^- + CH_3CH_2Cl/CH_3CH_2I$, $Cl^- + CH_3CH_2I$, as well as, $OH^- + CH_3I$. With the crossed-beam results at hand, we have presented a comprehensive theoretical–experimental study on the dynamics of the $OH^- + CH_3I$ reaction. The product ions of I^-, CH_2I^- and $[I\cdots H_2O]^-/[I\cdots OH]^-$ can be detected by the crossed-beam imaging technique, and 11 various reaction channels were identified by our simulations. The measured branching ion ratios, product scattering angle and internal energy distributions are in accord with the QCT results. The direct dynamics ICSs obtained by Xie and co-

workers are in qualitative agreement with our data, however, our QCT calculations reflects the experimental data markedly better than direct dynamics.

Previously, for the $OH^- + CH_3F$ reaction, the Hase group reported a direct dynamics study focusing on the influence of the product-like deep $CH_3OH\cdots F^-$ global minimum. It was found that in the ~90% of cases, the reaction avoids the minimum in the exit channel, but in the remaining ~10%, the system can easily become ensnared in that post-reaction well. Motivated by this, we carried out QCT simulations on the recently developed PES at numerous E_{coll} to analyse the dynamic character of the $OH^- + CH_3F$ reaction in detail. Our trajectories confirmed the avoidance of the H-bonded global minimum, and unveiled a novel indirect reaction pathway as well. This so-called oxide ion substitution is facilitated by a proton abstraction from the hydroxyl group at the $CH_3OH\cdots F^-$ region leading to the unexpected products of $HF + CH_3O^-$. Recently, Li and co-workers also provided a QCT study of the $OH^- + CH_3F$ reaction validating the existence of the novel oxide ion substitution.

Within the scope of the thesis, a detailed study of the dynamics of a polyatom-polyatom reaction, namely $NH_2^- + CH_3I$, has been carried out for the first time. In contrast to the $OH^- + CH_3F/CH_3I$ cases, at higher E_{coll}, the notable indirect nature of the S_N2 pathway promotes the formation of the vibrationally excited $[CH_3\cdots NH_2]$ complexes. The rotation of the CH_3 fragments may proceed in these $[CH_3\cdots NH_2]$ complexes enabling two non-traditional S_N2 retention pathways. In addition, considerable iodine abstraction can be recognized as well, with the generation of the $CH_3 + [NH_2\cdots I]^-$ products.

These findings presented in the thesis incontrovertibly demonstrate that basic gas-phase S_N2 reactions can still reveal previously unseen phenomena calling for further investigations. It should be noted that alternative pathways of the unusual oxide ion substitution may occur in other reactions: The most promising nominee is the $SH^- + CH_3F$ reaction, where the corresponding sulfide ion substitution is exothermic with a reaction enthalpy of approx. −3 kcal mol^{-1}, while the S_N2 pathway is endothermic (~11 kcal mol^{-1}). In the cases of complex formation and Walden inversion with complex formation, the key element is the indirect character of the S_N2 path, which may take place in additional polyatomic S_N2 reactions of $PH_2^-/CH_3^-/HOO^- + CH_3Y$, as well.

6 Összefoglalás

Az 1970-es évek óta a gázfázisú S_N2 reakciók vizsgálatát célzó kutatások a figyelem középpontjában helyezkednek el és számos elméleti tanulmány foglalkozik a lehetséges reakciómechanizmusok elemzésével. Eleinte a fő cél a hagyományos Walden-inverziós útvonal felderítése volt, és ahogy fejlődtek az elméleti módszerek, egyre összetettebb kép rajzolódott ki a reakció folyamatáról. A kvázi-klasszikus trajektória (*quasi-classical trajectory*, QCT) módszer a gázfázisú reakciódinamika tanulmányozásának egyik leggyakoribb eszköze, amelyhez elengedhetetlen a reakció potenciálisenergia-felület (*potential energy surface*, PES) kémiai szempontból releváns régióinak az ismerete. A PES leírható egy analitikus függvénnyel, ami nagymértékben növeli a számítási hatékonyságot azokkal a nagyobb számítási igényű direkt dinamikai szimulációkkal szemben, amelyek minden magkonfigurációnál menet közben számolják ki a szükséges potenciális energiákat és gradienseket. A nagy pontosságú PES-ek felépítése komoly kihívást jelent, így Győri és Czakó elkészítették a ROBOSURFER számítógépes programcsomagot, amely automatizálja a PES fejlesztésének folyamatát. Ezen ROBOSURFER program használata jelentősen egyszerűsítette a PES-ek fejlesztését, így hatékonyabbá téve a bonyolultabb kémiai rendszerek vizsgálatát.

Doktori munkám elsődleges célja a OH^-, SH^-, CN^-, NH_2^-, PH_2^- nukleofilek metil-halogenidekkel történő S_N2 reakcióinak vizsgálata volt. Kiemelt figyelmet szántunk a dupla-inverziós és elölről-támadásos mechanizmusok jellemzésére: a stacionárius pontok szerkezeteit, energiáit és harmonikus rezgési frekvenciáit az újszerű explicit-korrelált CCSD(T)-F12b módszerrel határoztuk meg az aug-cc-pV*n*Z (*n* = 2–4) báziskészletek segítségével. A $OH^- + CH_3Y$ [Y = F, Cl, Br és I] reakciók esetében figyelembe vettük a törzselektronok korrelációit, illetve a poszt-CCSD(T) hatásokat is, míg a $CN^- + CH_3F/CH_3Cl$ reakcióknál a skaláris relativisztikus effektusokat ugyancsak meghatároztuk. A $OH^- + CH_3Y$ mellett a $OH^- + CH_3CH_2Y$ reakciókat is górcső alá vettük, amely esetében az S_N2 csatornákkal versenyezve már E2 is lejátszódhat. A $OH^- + CH_3CH_2Y$ S_N2 csatornái termodinamikailag előnyösebbnek bizonyultak, mint az E2, míg a jelentős zérusponti energiák hatása miatt, az anti-E2 útvonalak mutatkoztak a kinetikailag kedvezőbbnek. A $OH^- + CH_3Y$ és $OH^- + CH_3CH_2Y$ S_N2 reakciók energiadiagramjai több szempontból is nagyon hasonlóak, mint például: a reaktánsokhoz képest energetikailag mélyebben elhelyezkedő Walden-inverziós útvonal, stabil elölről-

támadásos komplexképződés metil-jodid esetében, hidrogénkötéses globális minimum a kimeneti csatornában, kedvezőbb dupla-inverziós retenciós mechanizmusok stb. A CN^- ambidens nukleofil jellegének köszönhetően két különböző típusú S_N2 reakcióútvonalat is vizsgáltunk, melyek a $CH_3CN + Y^-$ és a $CH_3NC + Y^-$ termékekhez vezetnek. Kimutattuk, hogy a C–C kötés képződése termodinamikailag és kinetikailag is kedvezőbb, mint a kérdéses C–N kialakulásáé. A $OH^- + CH_3CH_2Y$ és a $CN^-/NC^- + CH_3Y$ esetében további különböző reakciók entalpiáját ugyancsak kiszámítottuk. Az általunk meghatározott reakcióentalpiák jó egyezést mutatnak (< 1 kcal mol^{-1}) a „kísérleti", ATcT (*Active Thermochemical Tables*) adatbázisból nyert értékekkel a legtöbb esetben. A 24 darab S_N2 reakció közül, a legexotermebb az $NH_2^- + CH_3I$, míg a $SH^- + CH_3F$ az egyedüli endoterm útvonal. A hagyományos Walden-inverziós átmeneti állapotok nem léteznek a $OH^-/NH_2^-/PH_2^- + CH_3I$ reakciók esetében, habár másfajta, reagensszerű átmenetei állapotokat sikerült azonosítani a bemeneti csatornákban. Továbbá, az elölről-támadásos mechanizmusokhoz képest a dupla-inverziós gátmagasságok általában alacsonyabbak, sőt, a $OH^- + CH_3I$ és az $NH_2^- + CH_3Y$ [Y = Cl, Br és I] reakcióknál gát nélkül is lejátszódhat a dupla inverzió. Összességében, a disszertáció több mint 200 stacionárius pont feltérképezését foglalja magában.

A $OH^- + CH_3I/CH_3F$ és az $NH_2^- + CH_3I$ reakciók esetében, globális, analitikus PES-eket fejlesztettünk a ROBOSURFER programcsomag segítségével. A $OH^- + CH_3I$ reakció vizsgálata során fény derült a CCSD(T)-F12b pontatlanságára, ugyanis bizonyos szerkezetek esetén a módszer túlságosan negatív energiákat szolgáltatott. Ezt a problémát a Brueckner csatolt klaszter módszeren alapuló úgynevezett kompozit energiák számításával sikerült kezelni. Az analitikus PES illesztése a permutációra invariáns polinom módszerrel történt Morse-típusú koordináták alkalmazásával. Annak érdekében, hogy teljesebb képet kapjunk a reakciókról, a protonabsztrakciós csatornák stacionárius pontjait is vizsgáltuk nagy pontosságú *ab initio* módszerekkel. A részletes dinamikai leíráshoz QCT szimulációkat végeztünk különböző ütközési energiákon.

Roland Wester és munkatársai által alkalmazott keresztezett molekulasugár, illetve az azzal kombinált sebességtérkép képfeldolgozásának módszerei lehetővé teszik számunkra ionok molekulákkal való reakcióinak kísérleti tanulmányozását. Számos nukleofil S_N2 (E2) reakcióját vizsgálták ezen kombinált módszer segítségével: $F^- + CH_3Cl/CH_3I$, $Cl^- + CH_3I$, $F^- + CH_3CH_2Cl/CH_3CH_2I$, $Cl^- + CH_3CH_2I$, valamint $OH^- + CH_3I$. A mérési eredményeiket felhasználva, a $OH^- + CH_3I$ reakció dinamikáját

egy átfogó elméleti-kísérleti munka keretein belül sikerült felderítenünk. I^-, CH_2I^- és $[I\cdots H_2O]^-/[I\cdots OH]^-$ termékeket sikerült detektálni a mérések során, és a QCT szimulációink révén 11 reakciócsatornát tudtunk megkülönböztetni. Ami a termékek képződéseinek arányát, a szórási szögeinek, illetve a belső energiáinak eloszlását illeti, kielégítő egyezés állapítható meg a számított és a mért eredmények között. Ugyan a Xie és munkatársai által korábban végzett direkt dinamikai szimulációk többé-kevésbé összhangban vannak a QCT eredményeinkkel, a mi számításaink pontosabb egyezést mutatnak a kísérletekkel.

A $OH^- + CH_3F$ reakció esetében, Hase és munkatársai a kimeneti csatornában található mély $CH_3OH\cdots F^-$ globális minimum természetét vizsgálták. Megállapították, hogy az esetek kb. 90%-ában a reakció elkerüli a minimumot, de a maradék kb. 10%-ban a reakció könnyen „elakad” ebben a mély völgyben. Ezen felfedezés ösztönzött minket, hogy számos ütközési energián QCT számításokat hajtsunk végre a nemrégiben fejlesztett PES-en, részletesen elemezve a $OH^- + CH_3F$ reakció dinamikáját. A szimulációink megerősítették, hogy a reakció nagyrészt elkerüli a hidrogénkötéses globális minimumot, azonban egy új, indirekt reakcióutat is feltártak. Az úgynevezett oxidion-szubsztitúció során a reakció megreked a $CH_3OH\cdots F^-$ globális minimumban, ahol egy idő után a F^- leszakítja a protont a hidroxilcsoportról a szokatlan $HF + CH_3O^-$ termékek képződését eredményezve. A közelmúltban Li és munkatársai is vizsgálták a $OH^- + CH_3F$ reakciót QCT módszer segítségével és igazolták az általunk leírt oxidion-szubsztitúció létezését.

A munkánk során az $NH_2^- + CH_3I$ reakciót is tanulmányoztuk, amely során első alkalommal fejlesztettünk egy poliatom + poliatom típusú reakcióra egy globális, analitikus PES-t. A $OH^- + CH_3F/CH_3I$ reakciókkal ellentétben, magasabb ütközési energiákon az S_N2 indirekt mechanizmusainak aránya egyre jelentősebb, elősegítve ezzel a rezgésileg gerjesztett $[CH_3\cdots NH_2]$ komplexek kialakulását a trajektória közben. Mivel ezen $[CH_3\cdots NH_2]$ komplexeken belül a CH_3 csoport forgása megengedett, így lehetséges, hogy a termékek konfigurációja, a reaktánsokhoz képest, nem változik a reakció során. Kutatásaink során, két ilyen új komplexképződéssel járó retenciós mechanizmust is sikerült azonosítanunk. Továbbá, szimulációink a jódabsztrakció során keletkező termékek ($CH_3 + [NH_2\cdots I]^-$) nagyobb arányát is felfedték.

A disszertációban bemutatott eredmények ismeretében kétségtelen, hogy az egyszerűbb gázfázisú S_N2 reakciók dinamikája még mindig meglepetéseket tartogathat számunkra. Oxidion-szubsztitúció alternatívái más reakciók esetében is előfordulhatnak, például a $SH^- + CH_3F$ esetében, ahol a lehetséges szulfidion-szubsztitúció exotermnek

bizonyul (reakció entalpiája kb. −3 kcal mol^{-1}), míg az S_N2 csatorna endoterm (~11 kcal mol^{-1}). A komplexképződéssel járó retenciós útvonalak meghatározó eleme az S_N2 csatorna indirekt jellege, mely számos más reakciónál ($PH_2^-/CH_3^-/HOO^-$ + CH_3Y) is lehetséges.

7 References

[1] D. A. Tasi, T. Michaelsen, R. Wester and G. Czakó, *Phys. Chem. Chem. Phys.*, 2023, **25**, 4005.

[2] D. A. Tasi and G. Czakó, *J. Chem. Phys.*, 2022, **156**, 184306.

[3] Z. Kerekes, D. A. Tasi and G. Czakó, *J. Phys. Chem. A*, 2022, **126**, 889.

[4] D. A. Tasi and G. Czakó, *Chem. Sci.*, 2021, **12**, 14369.

[5] D. A. Tasi, C. Tokaji and G. Czakó, *Phys. Chem. Chem. Phys.*, 2021, **23**, 13526.

[6] G. Czakó**,** T. Győri, D. Papp, V. Tajti and D. A. Tasi, *J. Phys. Chem. A*, 2021, **125**, 2385.

[7] D. A. Tasi, T. Győri and G. Czakó, *Phys. Chem. Chem. Phys.*, 2020, **22**, 3775.

[8] D. A. Tasi, Z. Fábián and G. Czakó, *Phys. Chem. Chem. Phys.*, 2019, **21**, 7921.

[9] D. A. Tasi, Z. Fábián and G. Czakó, *J. Phys. Chem. A*, 2018, **122**, 5773.

[10] G. Czakó**,** T. Győri, B. Olasz, D. Papp, I. Szabó, V. Tajti and D. A. Tasi*, Phys. Chem. Chem. Phys.*, 2020, **22**, 4298.

1 W. A. Cowdrey, E. D. Hughes, C. K. Ingold, S. Masterman and A. D. Scott, *J. Chem. Soc.*, 1937, 1252.

2 C. K. Ingold., *Structure and Mechanism in Organic Chemistry*, Cornell Univ. Press, Ithaca, NY, 1953.

3 R. S. Cahn, C. Ingold and V. Prelog, *Angew. Chemie Int. Ed. English*, 1966, **5**, 385.

4 W. N. Olmstead and J. I. Brauman, *J. Am. Chem. Soc.*, 1977, **99**, 4219.

5 S. S. Shaik, H. B. Schlegel and S. Wolfe, *Theoretical Aspects of Physical Organic Chemistry: The S_N2 Mechanism*, Wiley, New York, 1992.

6 W. L. Hase, *Science*, 1994, **266**, 998.

7 T. A. Hamlin, M. Swart and F. M. Bickelhaupt, *ChemPhysChem*, 2018, **19**, 1315.

8 R. Wester, *Mass Spectrom. Rev.*, 2022, **41**, 627.

9 J. Mikosch, S. Trippel, C. Eichhorn, R. Otto, U. Lourderaj, J. X. Zhang, W. L. Hase, M. Weidemüller and R. Wester, *Science*, 2008, **319**, 183.

10 P. Manikandan, J. Zhang and W. L. Hase, *J. Phys. Chem. A*, 2012, **116**, 3061.

11 M. Stei, E. Carrascosa, M. A. Kainz, A. H. Kelkar, J. Meyer, I. Szabó, G. Czakó and R. Wester, *Nat. Chem.*, 2016, **8**, 151.

12 J. Xie and W. L. Hase, *Science*, 2016, **352**, 32.

13 I. Szabó and G. Czakó, *Nat. Commun.*, 2015, **6**, 5972.

14 Y.-T. Ma, X. Ma, A. Li, H. Guo, L. Yang, J. Zhang and W. L. Hase, *Phys. Chem. Chem. Phys.*, 2017, **19**, 20127.

15 J. D. Evanseck, J. F. Blake and W. L. Jorgensen, *J. Am. Chem. Soc.*, 1987, **109**, 2349.

16 H. Tachikawa, M. Igarashi and T. Ishibashi, *J. Phys. Chem. A*, 2002, **106**, 10977.

17 H. Tachikawa and M. Igarashi, *Chem. Phys.*, 2006, **324**, 639.

18 J. M. Gonzales, R. S. Cox, S. T. Brown, W. D. Allen and H. F. Schaefer, *J. Phys. Chem. A*, 2001, **105**, 11327.

19 J. M. Gonzales, C. Pak, R. Sidney Cox, W. D. Allen, H. F. Schaefer, A. G. Császár and G. Tarczay, *Chem. - A Eur. J.*, 2003, **9**, 2173.

20 Y. Ren and H. Yamataka, *Chem. – A Eur. J.*, 2007, **13**, 677.

21 S. M. Villano, N. Eyet, W. C. Lineberger and V. M. Bierbaum, *J. Am. Chem. Soc.*, 2009, **131**, 8227.

22 J. M. Garver, S. Gronert and V. M. Bierbaum, *J. Am. Chem. Soc.*, 2011, **133**, 13894.

23 D. L. Thomsen, J. N. Reece, C. M. Nichols, S. Hammerum and V. M. Bierbaum, *J. Am. Chem. Soc.*, 2013, **135**, 15508.

24 L. Sun, K. Song and W. L. Hase, *Science*, 2002, **296**, 875.

25 T. Tsutsumi, Y. Ono, Z. Arai and T. Taketsugu, *J. Chem. Theory Comput.*, 2018, **14**, 4263.

26 T. Tsutsumi, Y. Ono, Z. Arai and T. Taketsugu, *J. Chem. Theory Comput.*, 2020, **16**, 4029.

27 S. R. Hare, L. A. Bratholm, D. R. Glowacki and B. K. Carpenter, *Chem. Sci.*, 2019, **10**, 9954.

28 L. Sun, K. Song, W. L. Hase, M. Sena and J. M. Riveros, *Int. J. Mass Spectrom.*, 2003, **227**, 315.

29 S. Zhao, G. Fu, W. Zhen, L. Yang, J. Sun and J. Zhang, *Phys. Chem. Chem. Phys.*, 2022, **24**, 24146.

30 H. Yin, D. Wang and M. Valiev, *J. Phys. Chem. A*, 2011, **115**, 12047.

31 Y. Xu, T. Wang and D. Wang, *J. Chem. Phys.*, 2012, **137**, 184501.

32 J. Chen, Y. Xu and D. Wang, *J. Comput. Chem.*, 2014, **35**, 445.

33 C. Li, X. Xin and D. Wang, *Phys. Chem. Chem. Phys.*, 2021, **23**, 23267.

34 R. Otto, J. Brox, S. Trippel, M. Stei, T. Best and R. Wester, *Nat. Chem.*, 2012, **4**,

534.

35 J. Xie, R. Otto, J. Mikosch, J. Zhang, R. Wester and W. L. Hase, *Acc. Chem. Res.*, 2014, **47**, 2960.

36 E. Carrascosa, J. Meyer and R. Wester, *Chem. Soc. Rev.*, 2017, **46**, 7498.

37 J. Xie, R. Sun, M. R. Siebert, R. Otto, R. Wester and W. L. Hase, *J. Phys. Chem. A*, 2013, **117**, 7162.

38 J. Xie, S. C. Kohale, W. L. Hase, S. G. Ard, J. J. Melko, N. S. Shuman and A. A. Viggiano, *J. Phys. Chem. A*, 2013, **117**, 14019.

39 J. Xie, J. Zhang and W. L. Hase, *Int. J. Mass Spectrom.*, 2015, **378**, 14.

40 R. Otto, J. Xie, J. Brox, S. Trippel, M. Stei, T. Best, M. R. Siebert, W. L. Hase and R. Wester, *Faraday Discuss.*, 2012, **157**, 41.

41 J. Xie, J. Zhang, R. Sun, R. Wester and W. L. Hase, *Int. J. Mass Spectrom.*, 2019, **438**, 115.

42 J. Xie, R. Otto, R. Wester and W. L. Hase, *J. Chem. Phys.*, 2015, **142**, 244308.

43 J. Xie, X. Ma, J. Zhang, P. M. Hierl, A. A. Viggiano and W. L. Hase, *Int. J. Mass Spectrom.*, 2017, **418**, 122.

44 X. Ji, C. Zhao and J. Xie, *Phys. Chem. Chem. Phys.*, 2021, **23**, 6349.

45 R. F. W. Bader, A. J. Duke and R. R. Messer, *J. Am. Chem. Soc.*, 1973, **95**, 7715.

46 D. K. Bohme, G. I. Mackay and J. D. Payzant, *J. Am. Chem. Soc.*, 1974, **96**, 4027.

47 B. D. Wladkowski and J. I. Brauman, *J. Am. Chem. Soc.*, 1992, **114**, 10643.

48 C. Li, P. Ross, J. E. Szulejko and T. B. McMahon, *J. Am. Chem. Soc.*, 1996, **118**, 9360.

49 J. M. Garver, Y. R. Fang, N. Eyet, S. M. Villano, V. M. Bierbaum and K. C. Westaway, *J. Am. Chem. Soc.*, 2010, **132**, 3808.

50 J. M. Garver, N. Eyet, S. M. Villano, Z. Yang and V. M. Bierbaum, *Int. J. Mass Spectrom.*, 2011, **301**, 151.

51 Y. Xu, J. Zhang and D. Wang, *Phys. Chem. Chem. Phys.*, 2014, **16**, 19993.

52 Y. Xu, J. Zhang and D. Wang, *J. Chem. Phys.*, 2015, **142**, 244505.

53 E. Carrascosa, M. Bawart, M. Stei, F. Linden, F. Carelli, J. Meyer, W. D. Geppert, F. A. Gianturco and R. Wester, *J. Chem. Phys.*, 2015, **143**, 184309.

54 J. F. Bunnett, *Angew. Chemie Int. Ed. English*, 1962, **1**, 225.

55 T. Minato and S. Yamabe, *J. Am. Chem. Soc.*, 1985, **107**, 4621.

56 T. Minato and S. Yamabe, *J. Am. Chem. Soc.*, 1988, **110**, 4586.

57 C. H. DePuy, S. Gronert, A. Mullin and V. M. Bierbaum, *J. Am. Chem. Soc.*, 1990, **112**, 8650.

58 S. Gronert, C. H. DePuy and V. M. Bierbaum, *J. Am. Chem. Soc.*, 1991, **113**, 4009.

59 S. Gronert, *J. Am. Chem. Soc.*, 1991, **113**, 6041.

60 F. M. Bickelhaupt, N. M. M. Nibbering, E. J. Baerends and T. Ziegler, *J. Am. Chem. Soc.*, 1993, **115**, 9160.

61 W. P. Hu and D. G. Truhlar, *J. Am. Chem. Soc.*, 1996, **118**, 860.

62 D. S. Chung, C. K. Kim, B. S. Lee and I. Lee, *J. Phys. Chem. A*, 1997, **101**, 9097.

63 S. Gronert, *Acc. Chem. Res.*, 2003, **36**, 848.

64 S. M. Villano, S. Kato and V. M. Bierbaum, *J. Am. Chem. Soc.*, 2006, **128**, 736.

65 F. M. Bickelhaupt, *J. Comput. Chem.*, 1999, **20**, 114.

66 A. P. Bento, M. Sola and F. M. Bickelhaupt, *J. Chem. Theory Comput.*, 2008, **4**, 929.

67 M. Swart, M. Solà and F. M. Bickelhaupt, *J. Chem. Theory Comput.*, 2010, **6**, 3145.

68 G. N. Merrill, S. Gronert and S. R. Kass, *J. Phys. Chem. A*, 1997, **101**, 208.

69 B. Ensing and M. L. Klein, *Proc. Natl. Acad. Sci.*, 2005, **102**, 6755.

70 Y. Zhao and D. G. Truhlar, *J. Chem. Theory Comput.*, 2010, **6**, 1104.

71 M. Mugnai, G. Cardini and V. Schettino, *J. Phys. Chem. A*, 2003, **107**, 2540.

72 X.-P. Wu, X.-M. Sun, X.-G. Wei, Y. Ren, N.-B. Wong and W.-K. Li, *J. Chem. Theory Comput.*, 2009, **5**, 1597.

73 L. Yang, J. Zhang, J. Xie, X. Ma, L. Zhang, C. Zhao and W. L. Hase, *J. Phys. Chem. A*, 2017, **121**, 1078.

74 P. Vermeeren, T. Hansen, P. Jansen, M. Swart, T. A. Hamlin and F. M. Bickelhaupt, *Chem. – A Eur. J.*, 2020, **26**, 15538.

75 V. Tajti and G. Czakó, *J. Phys. Chem. A*, 2017, **121**, 2847.

76 J. Meyer, V. Tajti, E. Carrascosa, T. Győri, M. Stei, T. Michaelsen, B. Bastian, G. Czakó and R. Wester, *Nat. Chem.*, 2021, **13**, 977.

77 P. Vermeeren, T. Hansen, M. Grasser, D. R. Silva, T. A. Hamlin and F. M. Bickelhaupt, *J. Org. Chem.*, 2020, **85**, 14087.

78 M. Gallegos, A. Costales and Á. Martín Pendás, *J. Phys. Chem. A*, 2022, **126**, 1871.

79 S. Gronert, A. E. Fagin, K. Okamoto, S. Mogali and L. M. Pratt, *J. Am. Chem.*

Soc., 2004, **126**, 12977.

80 K. M. Conner and S. Gronert, *J. Org. Chem.*, 2013, **78**, 8606.

81 P. R. Rablen, B. D. McLarney, B. J. Karlow and J. E. Schneider, *J. Org. Chem.*, 2014, **79**, 867.

82 E. Carrascosa, J. Meyer, J. Zhang, M. Stei, T. Michaelsen, W. L. Hase, L. Yang and R. Wester, *Nat. Commun.*, 2017, **8**, 25.

83 E. Carrascosa, J. Meyer, T. Michaelsen, M. Stei and R. Wester, *Chem. Sci.*, 2018, **9**, 693.

84 J. Meyer, E. Carrascosa, T. Michaelsen, B. Bastian, A. Li, H. Guo and R. Wester, *J. Am. Chem. Soc.*, 2019, **141**, 20300.

85 F. M. Bickelhaupt, E. J. Baerends and N. M. M. Nibbering, *Chem. – A Eur. J.*, 1996, **2**, 196.

86 N. Eyet, J. J. Melko, S. G. Ard and A. A. Viggiano, *Int. J. Mass Spectrom.*, 2015, **378**, 54.

87 L. Satpathy, P. K. Sahu, P. K. Behera and B. K. Mishra, *J. Phys. Chem. A*, 2018, **122**, 5861.

88 X. Liu, J. Zhang, L. Yang and W. L. Hase, *J. Am. Chem. Soc.*, 2018, **140**, 10995.

89 T. Hansen, J. C. Roozee, F. M. Bickelhaupt and T. A. Hamlin, *J. Org. Chem.*, 2022, **87**, 1805.

90 X. Wu, S. Zhang and J. Xie, *Phys. Chem. Chem. Phys.*, 2022, **24**, 12993.

91 A. Szabo and N. S. Ostlund, *Modern quantum chemistry: Introduction to advanced electronic structure theory*, Mineola N.Y.: Dover Publications, 1996.

92 M. Born and R. Oppenheimer, *Ann. Phys.*, 1927, **84**, 457.

93 H. B. Schlegel, in *Modern Electronic Structure Theory: Part I.*, 1995, pp. 459–500.

94 H. B. Schlegel, *J. Comput. Chem.*, 2003, **24**, 1514.

95 H. P. Hratchian and H. B. Schlegel, in *Theory and Applications of Computational Chemistry: The First Forty Years*, Elsevier, 2005, pp. 195–249.

96 C. Møller and M. S. Plesset, *Phys. Rev.*, 1934, **46**, 618.

97 J. A. Pople, J. S. Binkley and R. Seeger, *Int. J. Quantum Chem.*, 1976, **10**, 1.

98 J. Čížek, *J. Chem. Phys.*, 1966, **45**, 4256.

99 K. Raghavachari, G. W. Trucks, J. A. Pople and M. Head-Gordon, *Chem. Phys. Lett.*, 1989, **157**, 479.

100 R. J. Bartlett, *J. Phys. Chem.*, 1989, **93**, 1697.

101 G. D. Purvis and R. J. Bartlett, *J. Chem. Phys.*, 1982, **76**, 1910.

102 P. Piecuch and J. Paldus, *Int. J. Quantum Chem.*, 1989, **36**, 429.

103 G. E. Scuseria and T. J. Lee, *J. Chem. Phys.*, 1998, **93**, 5851.

104 J. Noga and R. J. Bartlett, *J. Chem. Phys.*, 1986, **86**, 7041.

105 Y. J. Bomble, J. F. Stanton, M. Kállay and J. Gauss, *J. Chem. Phys.*, 2005, **123**, 054101.

106 J. B. Robinson and P. J. Knowles, *J. Chem. Theory Comput.*, 2012, **8**, 2653.

107 N. C. Handy, J. A. Pople, M. Head-Gordon, K. Raghavachari and G. W. Trucks, *Chem. Phys. Lett.*, 1989, **164**, 185.

108 T. J. Lee and P. R. Taylor, *Int. J. Quantum Chem.*, 1989, **36**, 199.

109 T. B. Adler, G. Knizia and H. J. Werner, *J. Chem. Phys.*, 2007, **127**, 221106.

110 G. Knizia, T. B. Adler and H. J. Werner, *J. Chem. Phys.*, 2009, **130**, 054104.

111 S. F. Boys, *Proc. R. Soc. London. Ser. A. Math. Phys. Sci.*, 1950, **200**, 542.

112 R. Ditchfield, W. J. Hehre and J. A. Pople, *J. Chem. Phys.*, 1971, **54**, 724.

113 W. J. Hehre, K. Ditchfield and J. A. Pople, *J. Chem. Phys.*, 1972, **56**, 2257.

114 T. H. Dunning, *J. Chem. Phys.*, 1989, **90**, 1007.

115 D. E. Woon and T. H. Dunning, *J. Chem. Phys.*, 1993, **98**, 1358.

116 D. E. Woon and T. H. Dunning, *J. Chem. Phys.*, 1995, **103**, 4572.

117 J. G. Hill, S. Mazumder and K. A. Peterson, *J. Chem. Phys.*, 2010, **132**, 054108.

118 G. Frenking, I. Antes, M. Böhme, S. Dapprich, A. W. Ehlers, V. Jonas, A. Neuhaus, M. Otto, R. Stegmann, A. Veldkamp and S. F. Vyboishchikov, *Rev. Comput. Chem.*, 1996, **8**, 63.

119 T. R. Cundari, M. T. Benson, M. L. Lutz and S. O. Sommerer, *Rev. Comput. Chem.*, 1996, **8**, 145.

120 W. L. Hase, *Encyclopedia of Computational Chemistry*, Wiley, New York, 1998, pp. 399–407.

121 L. Sun and W. L. Hase, *Rev. Comput. Chem.*, 2003, **19**, 79.

122 B. J. Braams and J. M. Bowman, *Int. Rev. Phys. Chem.*, 2009, **28**, 577.

123 Z. Xie and J. M. Bowman, *J. Chem. Theory Comput.*, 2010, **6**, 26.

124 T. Győri and G. Czakó, *J. Chem. Theory Comput.*, 2020, **16**, 51.

125 L. Verlet, *Phys. Rev.*, 1967, **159**, 98.

126 L. Verlet, *Phys. Rev.*, 1968, **165**, 201.

127 A. Y. Dymarsky and K. N. Kudin, *J. Chem. Phys.*, 2005, **122**, 124103.

128 G. Czakó, *J. Phys. Chem. A*, 2012, **116**, 7467.

129 P. Papp, V. Tajti and G. Czakó, *Chem. Phys. Lett.*, 2020, **755**, 137780.

130 D. G. Truhlar, R. Steckler and M. S. Gordon, *Chem. Rev.*, 1987, **87**, 217.

131 R. A. Kendall, T. H. Dunning and R. J. Harrison, *J. Chem. Phys.*, 1992, **96**, 6796.

132 R. D. Amos, J. S. Andrews, N. C. Handy and P. J. Knowles, *Chem. Phys. Lett.*, 1991, **185**, 256.

133 K. A. Peterson, D. Figgen, E. Goll, H. Stoll and M. Dolg, *J. Chem. Phys.*, 2003, **119**, 11113.

134 M. Kállay and J. Gauss, *J. Chem. Phys.*, 2005, **123**, 214105.

135 K. A. Peterson and T. H. Dunning, *J. Chem. Phys.*, 2002, **117**, 10548.

136 M. Douglas and N. M. Kroll, *Ann. Phys.*, 1974, **82**, 89.

137 W. A. de Jong, R. J. Harrison and D. A. Dixon, *J. Chem. Phys.*, 2001, **114**, 48.

138 H.-J. Werner, P. J. Knowles, G. Knizia, F. R. Manby and M. Schütz, *et al.*, MOLPRO, version 2015.1, a package of ab initio programs, see http://www.molpro.net.

139 M. Kállay, P. R. Nagy, D. Mester, Z. Rolik, G. Samu, J. Csontos, J. Csóka, P. B. Szabó, L. Gyevi-Nagy, B. Hégely, I. Ladjánszki, L. Szegedy, B. Ladóczki, K. Petrov, M. Farkas, P. D. Mezei and Á. Ganyecz, *J. Chem. Phys.*, 2020, **152**, 074107.

140 MRCC, a quantum chemical program suite written by M. Kállay, P. R. Nagy, D. Mester, Z. Rolik, G. Samu, J. Csontos, J. Csóka, P. B. Szabó, L. Gyevi-Nagy, B. Hégely, I. Ladjánszki, L. Szegedy, B. Ladóczki, K. Petrov, M. Farkas, P. D. Mezei and Á. Ganyecz. See www.mrcc.hu.

141 B. Ruscic and D. H. Bross, Active Thermochemical Tables (ATcT) values based on ver. 1.122p of the Thermochemical Network (2020), available at ATcT.anl.gov.

142 B. Ruscic, R. E. Pinzon, M. L. Morton, G. Von Laszevski, S. J. Bittner, S. G. Nijsure, K. A. Amin, M. Minkoff and A. F. Wagner, *J. Phys. Chem. A*, 2004, **108**, 9979.

143 I. Szabó and G. Czakó, *J. Phys. Chem. A*, 2017, **121**, 9005.

144 J. M. Bowman, G. Czakó and B. Fu, *Phys. Chem. Chem. Phys.*, 2011, **13**, 8094.

145 C. Qu, Q. Yu and J. M. Bowman, *Annu. Rev. Phys. Chem.*, 2018, **69**, 151.

146 K. A. Brueckner, *Phys. Rev.*, 1954, **96**, 508.

147 J. F. Stanton, J. Gauss and R. J. Bartlett, *J. Chem. Phys.*, 1992, **97**, 5554.

148 J. D. Watts, J. Gauss and R. J. Bartlett, *J. Chem. Phys.*, 1993, **98**, 8718.

149 D. P. Tew, *J. Chem. Phys.*, 2016, **145**, 074103.

150 J. B. Robinson and P. J. Knowles, *J. Chem. Phys.*, 2012, **136**, 054114.

151 D. A. Mazziotti, *Phys. Rev. Lett.*, 2008, **101**, 253002.

152 J. B. Robinson and P. J. Knowles, *J. Chem. Phys.*, 2013, **138**, 074104.

153 D. Kats and F. R. Manby, *J. Chem. Phys.*, 2013, **139**, 021102.

154 D. Kats, *J. Chem. Phys.*, 2014, **141**, 061101.

155 D. Kats, D. Kreplin, H. J. Werner and F. R. Manby, *J. Chem. Phys.*, 2015, **142**, 064111.

156 J. A. Black and P. J. Knowles, *J. Chem. Phys.*, 2018, **148**, 194102.

157 T. Győri, B. Olasz, G. Paragi and G. Czakó, *J. Phys. Chem. A*, 2018, **122**, 3353.

158 G. S. Hammond, *J. Am. Chem. Soc.*, 1955, **77**, 334.

159 J. Mikosch, J. Zhang, S. Trippel, C. Eichhorn, R. Otto, R. Sun, W. A. De Jong, M. Weidemüller, W. L. Hase and R. Wester, *J. Am. Chem. Soc.*, 2013, **135**, 4250.

160 R. Wester, *Phys. Chem. Chem. Phys.*, 2013, **16**, 396.

161 J. J. Lin, J. Zhou, W. Shiu and K. Liu, *Rev. Sci. Instrum.*, 2003, **74**, 2495.

162 J. Qin, Y. Liu and J. Li, *J. Chem. Phys.*, 2022, **157**, 124301.

Appendix

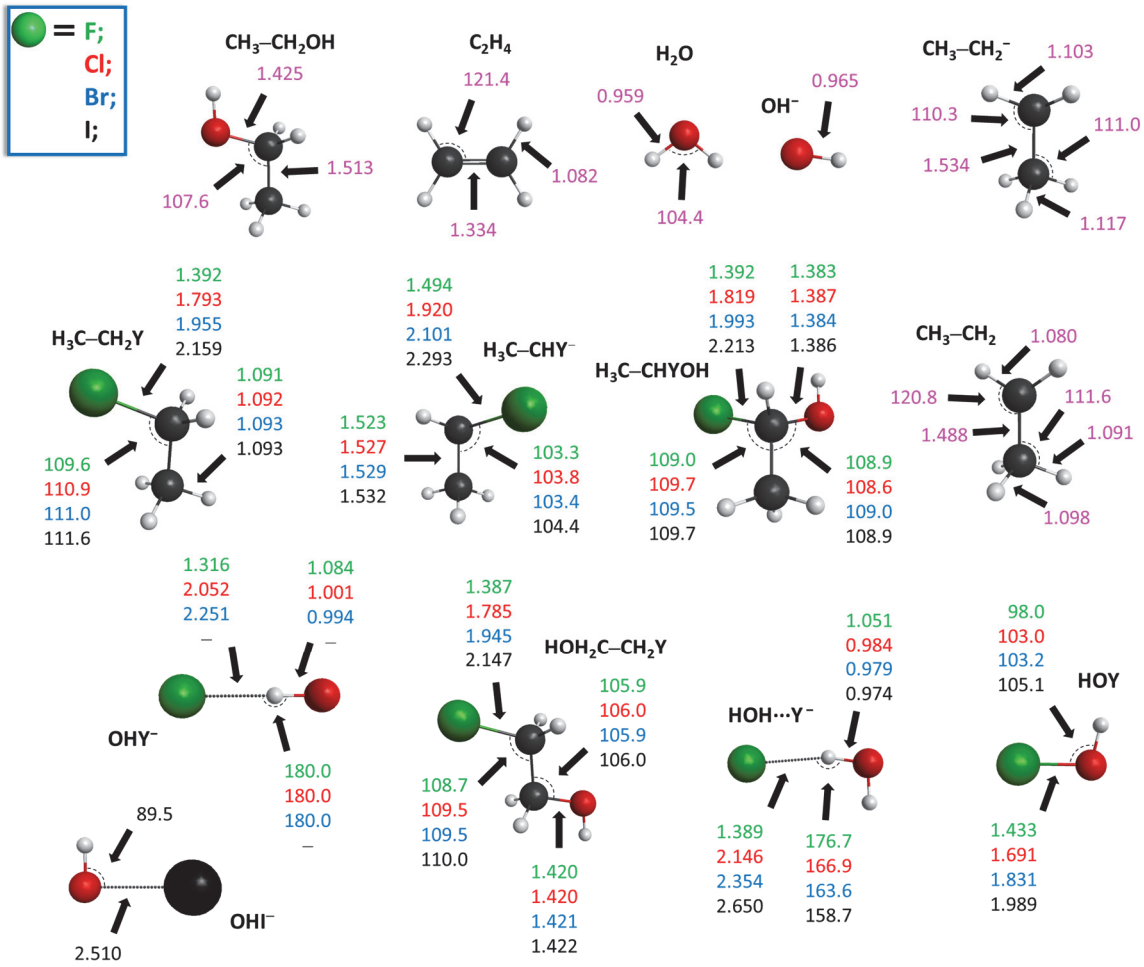

Figure S1 The CCSD(T)-F12b/aug-cc-pVTZ structures of the reactants and products of the OH^- +CH_3CH_2Y [Y = F, Cl, Br, I] reactions. Bond lengths are in Å and angles are in degrees. (Taken from ref. [5].)

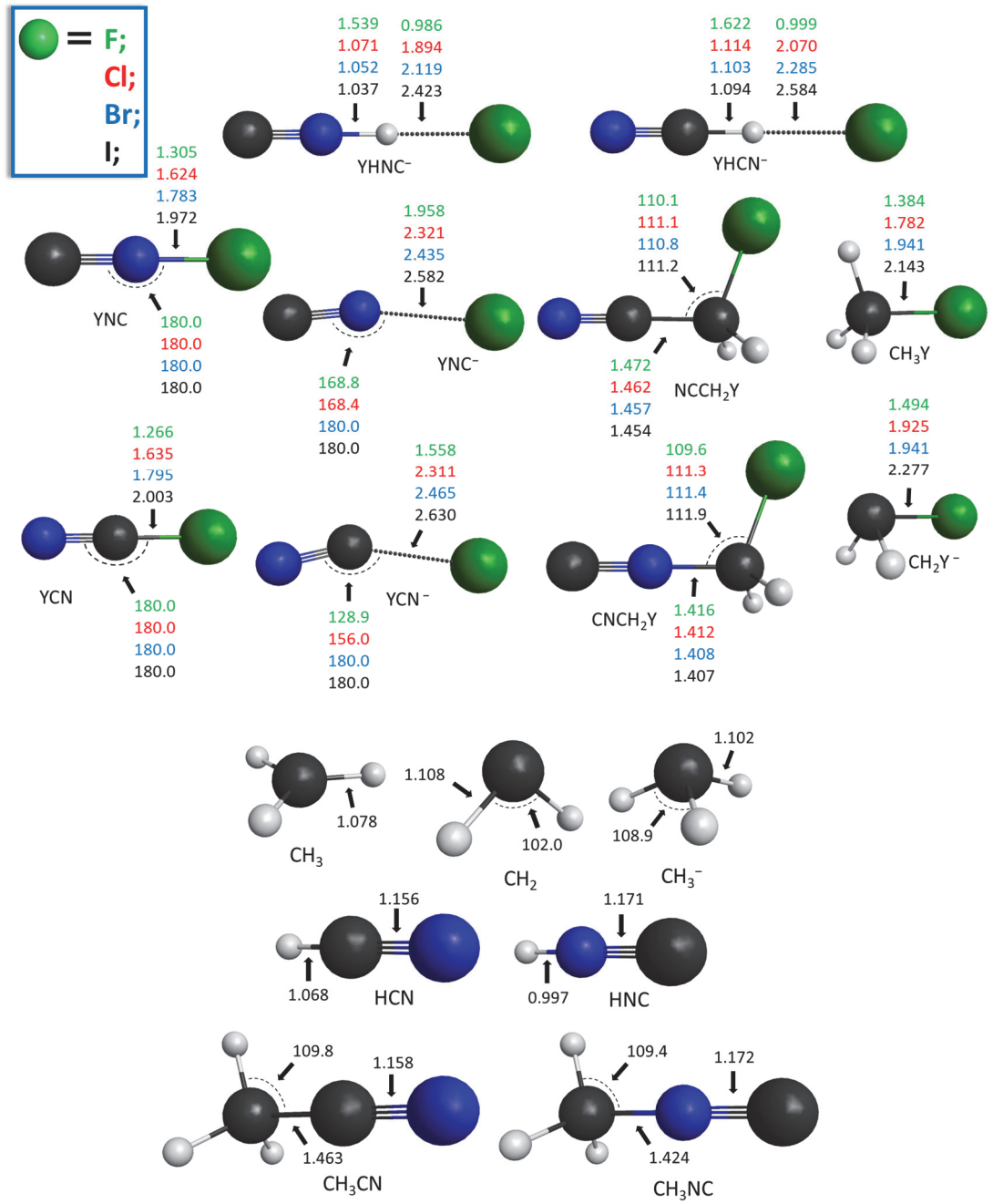

Figure S2 The CCSD(T)-F12b/aug-cc-pVTZ structures of the reactants and products of the NC^-/CN^- +CH_3Y [Y = F, Cl, Br, I] reactions. Bond lengths are in Å and angles are in degrees. (Taken from ref. [3].)

Table S1 The obtained relative *ab initio* energies (kcal mol^{-1}) of the S_N2 stationary points and several products for the C–C bond forming $NC^- + CH_3Y$ [Y = F, Cl, Br, I] reactions. The results are taken from ref. [3].

	CCSD(T)-F12b								
$NC^- + CH_3F$	**TZ**[a]	**QZ**[b]	**δT**[c]	**δ(Q)**[d]	**Δcore**[e]	**Δrel**[f]	**Classical**[g]	**ΔZPE**[h]	**Adiabatic**[i]
HMIN2	−9.45	−9.39	0.00	−0.03	0.01	0.00	−9.42	0.45	−8.97
PreMIN	−8.97	−8.88	−0.02	−0.03	0.00	0.00	−8.93	0.43	−8.51
WaldenTS	12.20	12.18	−0.12	−0.27	0.19	−0.04	11.94	0.17	12.11
PostHMIN2	−25.66	−25.72	0.00	−0.13	−0.54	0.05	−26.34	0.11	−26.24
FSTS	56.08	56.19	−0.15	−0.51	0.20	−0.04	55.69	−0.52	55.18
DITS	52.26	52.38	−0.08	−0.23	−0.25	0.03	51.85	−3.17	48.68
$F^- + CH_3CN$	−1.12	−1.44	0.02	−0.15	−0.54	0.06	−2.06	0.63	−1.43
$HCN + CH_2F^-$	62.53	62.44	−0.14	−0.11	0.00	−0.01	62.18	−3.27	58.91
$H^- + FH_2CCN$	60.96	61.20	0.14	−0.08	−0.37	0.00	60.89	−3.59	57.31
$FCN^- + CH_3$	75.26	75.23	−0.28	−0.25	0.08	−0.05	74.74	−5.19	69.55
$FCN + CH_3^-$	79.47	79.45	0.01	−0.28	−0.22	0.00	78.96	−3.64	75.32
$FHCN^- + CH_2$	72.83	72.99	−0.29	−0.04	0.42	−0.07	73.01	−6.61	66.40
$NC^- + CH_3Cl$	**TZ**[a]	**QZ**[b]	**δT**[c]	**δ(Q)**[d]	**Δcore**[e]	**Δrel**[f]	**Classical**[g]	**ΔZPE**[h]	**Adiabatic**[i]
HMIN2	−10.47	−10.46	0.00	−0.04	0.02	0.02	−10.45	0.34	−10.11
PreMIN	−9.80	−9.75	0.76	−0.05	0.02	0.02	−9.01	0.32	−8.69
WaldenTS	−0.05	−0.18	−0.11	−0.26	0.28	−0.04	−0.31	0.35	0.04
WaldenPostMIN	−47.85	−48.25	0.05	0.01	−0.36	0.11	−48.44	1.67	−46.77
PostHMIN2	−48.09	−48.44	0.05	−0.01	−0.38	0.11	−48.68	1.80	−46.89
FSMIN	0.72	0.80	0.01	−0.05	−0.02	−0.11	0.63	0.28	0.91
FSTS	47.11	47.04	−0.26	−0.65	0.28	−0.09	46.32	−0.56	45.76
DITS	38.47	38.45	0.00	−0.22	−0.26	0.12	38.09	−2.39	35.71
$Cl^- + CH_3CN$	−33.67	−34.15	0.07	0.00	−0.32	0.11	−34.29	1.61	−32.68
$HCN + CH_2Cl^-$	49.11	48.92	−0.12	−0.11	0.11	0.02	48.82	−2.76	46.07
$H^- + ClH_2CCN$	61.79	62.02	0.19	−0.11	−0.40	−0.03	61.68	−3.58	58.10
$ClCN^- + CH_3$	54.02	53.90	−0.52	−0.15	0.17	−0.15	53.25	−4.47	48.78
$ClCN + CH_3^-$	72.96	72.94	0.04	−0.31	−0.20	0.00	72.48	−3.52	68.96
$ClHCN^- + CH_2$	65.47	65.23	−0.33	0.07	0.44	−0.02	65.39	−6.03	59.36
$NC^- + CH_3Br$	**TZ**[a]	**QZ**[b]	**δT**[c]	**δ(Q)**[d]	**Δcore**[e]	**Δrel**[f]	**Classical**[g]	**ΔZPE**[h]	**Adiabatic**[i]
HMIN1	−9.28	−9.22	−0.01	−0.04	−0.01	−0.05	−9.29	0.36	−8.93
HMIN2	−10.79	−10.77	0.00	−0.05	0.02	−0.08	−10.80	0.34	−10.46
PreMIN	−10.14	−10.09	−0.02	−0.06	0.01	−0.07	−10.16	0.32	−9.83
WaldenTS	−4.04	−4.17	−0.11	−0.25	0.25	−0.13	−4.28	0.43	−3.86
WaldenPostMIN	−54.72	−55.22	0.06	0.03	−0.21	0.04	−55.35	2.07	−53.28
PostHMIN2	−54.64	−55.10	0.05	0.02	−0.24	0.00	−55.27	2.15	−53.12
FSMIN	−3.48	−3.39	0.03	−0.13	−0.01	0.03	−3.51	0.34	−3.17
FSTS	41.79	41.67	−0.28	−0.67	0.29	−0.03	41.01	−0.39	40.62
DITS	36.30	36.30	0.01	−0.22	−0.13	−0.05	35.96	−2.30	33.66
$Br^- + CH_3CN$	−41.71	−42.30	0.07	0.03	−0.07	0.15	−42.28	2.02	−40.26
$HCN + CH_2Br^-$	44.46	44.26	−0.14	−0.10	0.27	−0.04	44.29	−2.59	41.70
$H^- + BrH_2CCN$	61.38	61.59	0.21	−0.12	−0.45	0.00	61.23	−3.59	57.64
$BrCN^- + CH_3$	44.39	44.19	−0.45	−0.09	0.33	0.12	43.97	−4.31	39.67
$BrCN + CH_3^-$	73.06	73.00	0.06	−0.32	−0.05	0.05	72.70	−3.46	69.24
$BrHCN^- + CH_2$	60.31	59.99	−0.32	0.09	0.53	−0.18	60.29	−5.36	54.93
$NC^- + CH_3I$	**TZ**[a]	**QZ**[b]	**δT**[c]	**δ(Q)**[d]	**Δcore**[e]	**Δrel**[f]	**Classical**[g]	**ΔZPE**[h]	**Adiabatic**[i]
HMIN1	−9.65	−9.57	−0.01	−0.05	−0.06	−0.03	−9.70	0.51	−9.18
HMIN2	−10.82	−10.80	0.01	−0.05	−0.03	−0.03	−10.88	0.37	−10.52
HTS2	−9.58	−9.54	−0.01	−0.05	−0.05	−0.03	−9.65	0.39	−9.25
PreMIN	−10.13	−10.09	−0.03	−0.07	−0.04	−0.03	−10.23	0.29	−9.94
WaldenTS	−5.91	−6.07	−0.10	−0.26	0.18	−0.06	−6.25	0.46	−5.79
WaldenPostMIN	−59.99	−60.72	0.07	0.05	0.02	−0.04	−60.57	2.47	−58.09
PostHMIN2	−59.65[j]	−60.31[j]	0.08[j]	0.03[j]	−0.06[j]	−0.05[j]	−60.25[j]	2.40[j]	−57.86[j]
FSMIN	−10.15	−10.13	0.06	−0.23	0.12	0.08	−10.19	0.30	−9.88
FSTS	38.55	38.35	−0.30	−0.74	0.35	−0.01	37.67	−0.31	37.35
DITS	31.97	31.92	0.03	−0.22	−0.07	−0.03	31.66	−2.04	29.62
$I^- + CH_3CN$	−48.38	−49.21	0.09	0.06	0.28	−0.06	−48.79	2.42	−46.37
$HCN + CH_2I^-$	39.23	38.95	−0.13	−0.11	0.36	−0.09	39.07	−2.37	36.70
$H^- + IH_2CCN$	60.76	60.99	0.22	−0.13	−0.50	0.04	60.58	−3.49	57.08
$ICN^- + CH_3$	35.45	35.19	−0.32	−0.05	0.63	0.02	35.45	−3.77	31.67
$ICN + CH_3^-$	70.23	70.16	0.08	−0.33	0.19	−0.01	70.09	−3.31	66.78
$IHCN^- + CH_2$	56.80	56.29	−0.31	0.12	0.73	−0.17	56.83	−5.18	51.65

[a] CCSD(T)-F12b/aug-cc-pVTZ. [b] Eq. (4.1). [c] Eq. (4.2). [d] Eq. (4.3). [e] Eq. (4.4). [f] Eq. (4.6), see Section 4.1 for Y = Br and I cases. [g] Eq. (4.7)/(4.8) [h] ΔZPE(CCSD(T)-F12b/aug-cc-pVTZ). [i] Eq. (4.7)/(4.8). [j] MP2/aug-cc-pVDZ geometry and frequencies are utilized.

Tables S2 The obtained relative *ab initio* energies (kcal mol^{-1}) of the S_N2 stationary points and several products for the C–N bond forming $CN^- + CH_3Y$ [Y = F, Cl, Br, I] reactions. The results are taken from ref. [3].

	CCSD(T)-F12b								
$CN^- + CH_3F$	**TZ**[a]	**QZ**[b]	**δT**[c]	**δ(Q)**[d]	**Δcore**[e]	**Δrel**[f]	**Classical**[g]	**ΔZPE**[h]	**Adiabatic**[i]
HMIN2	−9.42	−9.37	0.00	−0.03	0.01	0.00	−9.39	0.40	−8.99
PreMIN	−9.40	−9.33	−0.01	−0.01	0.01	0.00	−9.34	0.39	−8.94
WaldenTS	17.85	17.81	−0.12	−0.21	0.23	−0.02	17.69	0.23	17.92
PostHMIN2	−0.36	−0.40	−0.09	−0.01	−0.31	0.08	−0.73	0.56	−0.18
FSTS	64.39	64.61	−0.20	−0.48	0.26	−0.03	64.16	−0.44	63.72
DITS	59.18	59.35	−0.10	−0.12	−0.08	0.04	59.09	−3.89	55.20
$F^- + CH_3NC$	23.07	22.79	−0.11	0.08	−0.27	0.09	22.58	0.63	23.21
$HNC + CH_2F^-$	77.39	77.88	−0.30	0.18	0.19	0.02	77.98	−3.59	74.39
$H^- + FH_2CNC$	79.17	79.44	0.03	0.21	−0.09	0.03	79.62	−3.66	75.96
$FNC^- + CH_3$	97.59	97.73	−0.59	−0.47	0.17	−0.15	96.70	−5.38	91.31
$FNC + CH_3^-$	150.62	150.62	−0.20	−0.26	0.17	−0.05	150.28	−4.85	145.43
$FHNC^- + CH_2$	73.11	73.21	−0.28	0.01	0.46	−0.06	73.34	−6.32	67.02
$CN^- + CH_3Cl$	**TZ**[a]	**QZ**[b]	**δT**[c]	**δ(Q)**[d]	**Δcore**[e]	**Δrel**[f]	**Classical**[g]	**ΔZPE**[h]	**Adiabatic**[i]
HMIN2	−10.46	−10.45	0.00	−0.04	0.02	0.02	−10.44	0.33	−10.11
PreMIN	−10.18[j]	−10.15[j]	−0.01[j]	−0.02[j]	0.03[j]	0.02[j]	−10.15[j]	1.12[j]	−9.03[j]
WaldenTS	4.04	3.88	−0.11	−0.19	0.35	−0.03	3.90	0.40	4.29
WaldenPostMIN	−24.48	−24.85	−0.04	0.15	−0.11	0.14	−24.72	1.83	−22.89
FSMIN	0.52	0.62	0.00	−0.04	−0.02	−0.10	0.46	0.23	0.69
FSTS	52.75	52.72	−0.27	−0.60	0.37	−0.08	52.14	−0.28	51.87
DITS	46.56[k]	46.60[k]	−0.04[k]	−0.07[k]	−0.08[k]	0.10[k]	46.51[k]	−2.74[k]	43.77[k]
$Cl^- + CH_3NC$	−9.48	−9.91	−0.06	0.23	−0.04	0.15	−9.64	1.61	−8.03
$HNC + CH_2Cl^-$	63.96	64.37	−0.27	0.18	0.30	0.05	64.63	−3.08	61.55
$H^- + ClH_2CNC$	83.22	83.51	0.07	0.17	−0.12	0.00	83.63	−3.70	79.93
$ClNC^- + CH_3$	66.84	66.95	−0.36	−0.17	0.25	−0.21	66.46	−4.51	61.95
$ClNC + CH_3^-$	116.31	116.38	−0.13	−0.12	0.13	−0.03	116.23	−4.16	112.07
$ClHNC^- + CH_2$	73.87	73.67	−0.38	0.19	0.54	0.01	74.03	−6.36	67.67
$CN^- + CH_3Br$	**TZ**[a]	**QZ**[b]	**δT**[c]	**δ(Q)**[d]	**Δcore**[e]	**Δrel**[f]	**Classical**[g]	**ΔZPE**[h]	**Adiabatic**[i]
HMIN2	−10.78	−10.76	0.00	−0.05	0.02	−0.07	−10.78	0.34	−10.45
WaldenTS	−0.15	−0.33	−0.10	−0.19	0.34	−0.12	−0.28	0.41	0.14
WaldenPostMIN	−31.25	−31.72	−0.04	0.18	0.03	0.06	−31.54	2.19	−29.35
FSMIN	−3.18	−3.08	0.01	−0.08	−0.01	0.03	−3.16	0.15	−3.01
FSTS	47.10	47.02	−0.27	−0.63	0.43	−0.04	46.55	−0.21	46.34
DITS	44.39	44.45	−0.02	−0.08	0.02	−0.03	44.36	−2.72	41.65
$Br^- + CH_3NC$	−17.52	−18.07	−0.06	0.25	0.20	0.19	−17.67	2.02	−15.65
$HNC + CH_2Br^-$	59.31	59.71	−0.30	0.19	0.46	−0.01	60.06	−2.91	57.14
$H^- + BrH_2CNC$	83.57	83.86	0.09	0.15	−0.19	0.05	83.91	−3.70	80.20
$BrNC^- + CH_3$	55.31	55.21	−0.28	−0.10	0.46	0.16	55.29	−4.36	50.93
$BrNC + CH_3^-$	109.90	109.90	−0.11	−0.14	0.48	0.09	110.13	−4.03	106.10
$BrHNC^- + CH_2$	69.83	69.57	−0.38	0.23	0.61	−0.16	70.03	−5.87	64.15
$CN^- + CH_3I$	**TZ**[a]	**QZ**[b]	**δT**[c]	**δ(Q)**[d]	**Δcore**[e]	**Δrel**[f]	**Classical**[g]	**ΔZPE**[h]	**Adiabatic**[i]
HMIN2	−10.81	−10.80	0.01	−0.06	−0.04	−0.03	−10.88	0.33	−10.55
WaldenTS	−2.14	−2.35	−0.09	−0.21	0.31	−0.08	−2.33	0.51	−1.82
WaldenPostMIN	−36.40	−37.09	−0.02	0.21	0.26	−0.01	−36.64	2.59	−34.05
FSMIN	−8.79	−8.74	0.02	−0.13	0.05	0.08	−8.79	0.21	−8.58
FSTS	43.24	43.09	−0.24	−0.74	0.54	−0.03	42.65	−0.16	42.48
DITS	40.26	40.28	−0.01	−0.07	0.07	−0.01	40.27	−2.38	37.89
$I^- + CH_3NC$	−24.19	−24.98	−0.04	0.28	0.55	−0.03	−24.18	2.42	−21.76
$HNC + CH_2I^-$	54.08	54.40	−0.29	0.18	0.55	−0.05	54.84	−2.69	52.15
$H^- + IH_2CNC$	84.03	84.33	0.10	0.13	−0.25	0.08	84.32	−3.65	80.67
$INC^- + CH_3$	43.96	43.84	−0.20	−0.02	0.81	0.05	44.43	−3.99	40.44
$INC + CH_3^-$	98.40	98.38	−0.11	−0.11	0.82	0.05	98.99	−3.81	95.17
$IHNC^- + CH_2$	67.37	66.96	−0.38	0.28	0.78	−0.16	67.64	−5.39	62.25

[a] CCSD(T)-F12b/aug-cc-pVTZ. [b] Eq. (4.1). [c] Eq. (4.2). [d] Eq. (4.3). [e] Eq. (4.4). [f] Eq. (4.6), see Section 4.1 for Y = Br and I cases. [g] Eq. (4.7)/(4.8) [h] ΔZPE(CCSD(T)-F12b/aug-cc-pVTZ). [i] Eq. (4.7)/(4.8). [j] CCSD(T)-F12b/aug-cc-pVDZ geometry and frequencies are utilized. [k] MP2/aug-cc-pVDZ geometry and frequencies are utilized.

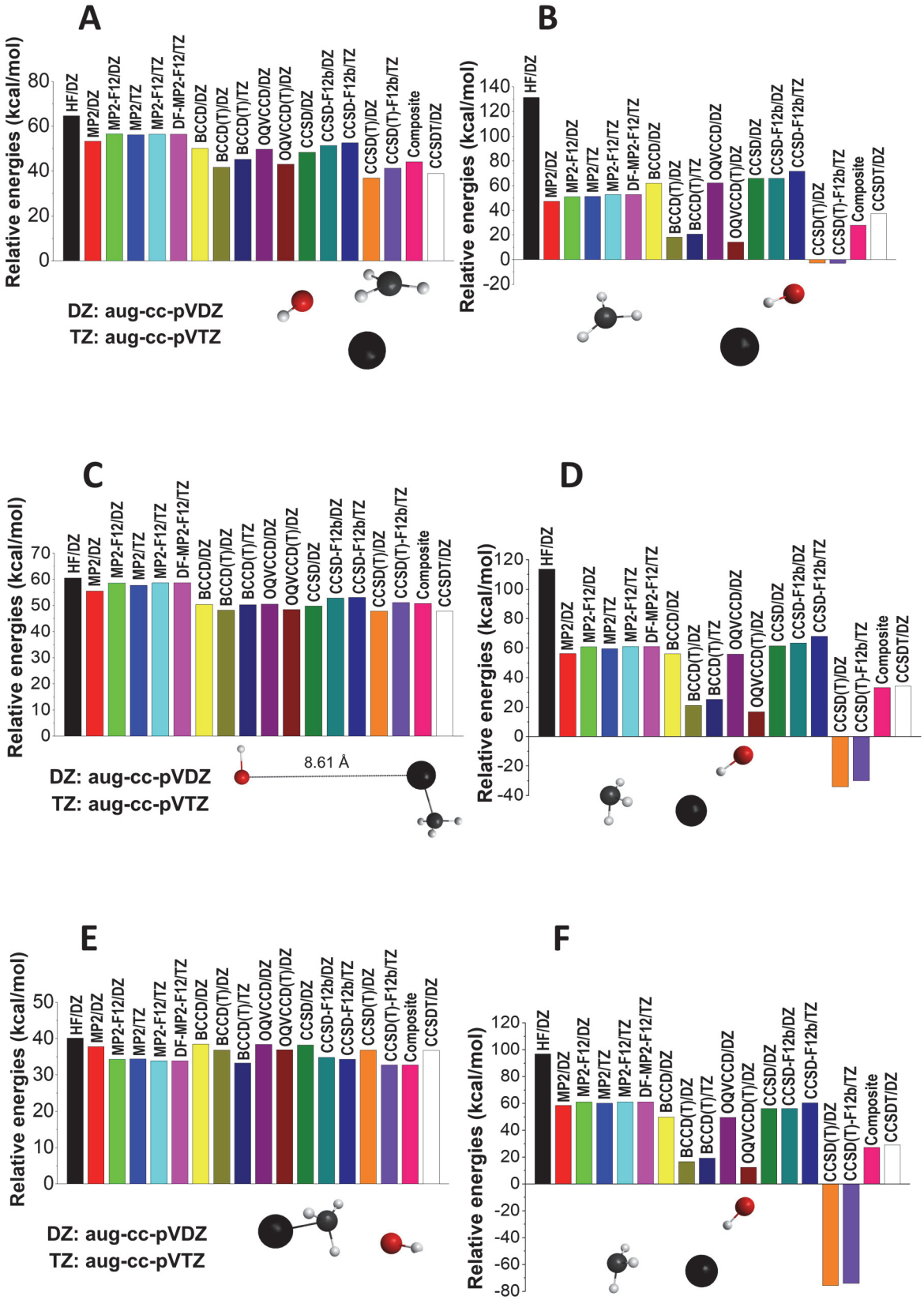

Figure S3 continues on the next page

Figure S3 continues

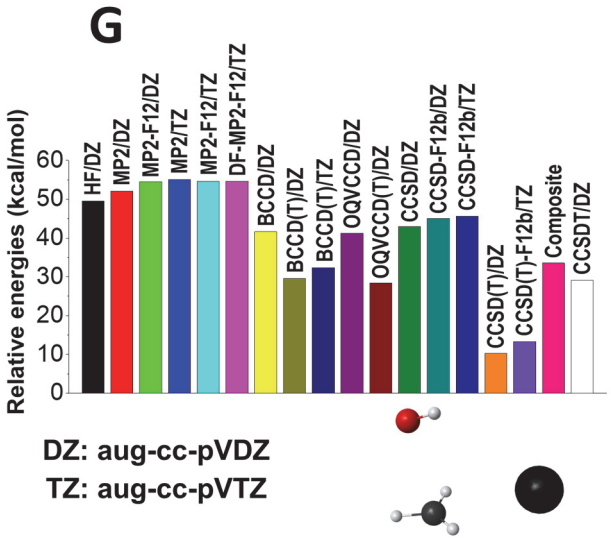

Figure S3 The determined *ab initio* energies of the representative structures of the $OH^- + CH_3I$ reaction representing the failure of the CCSD(T) method at certain cases. (Taken from ref. [7].)

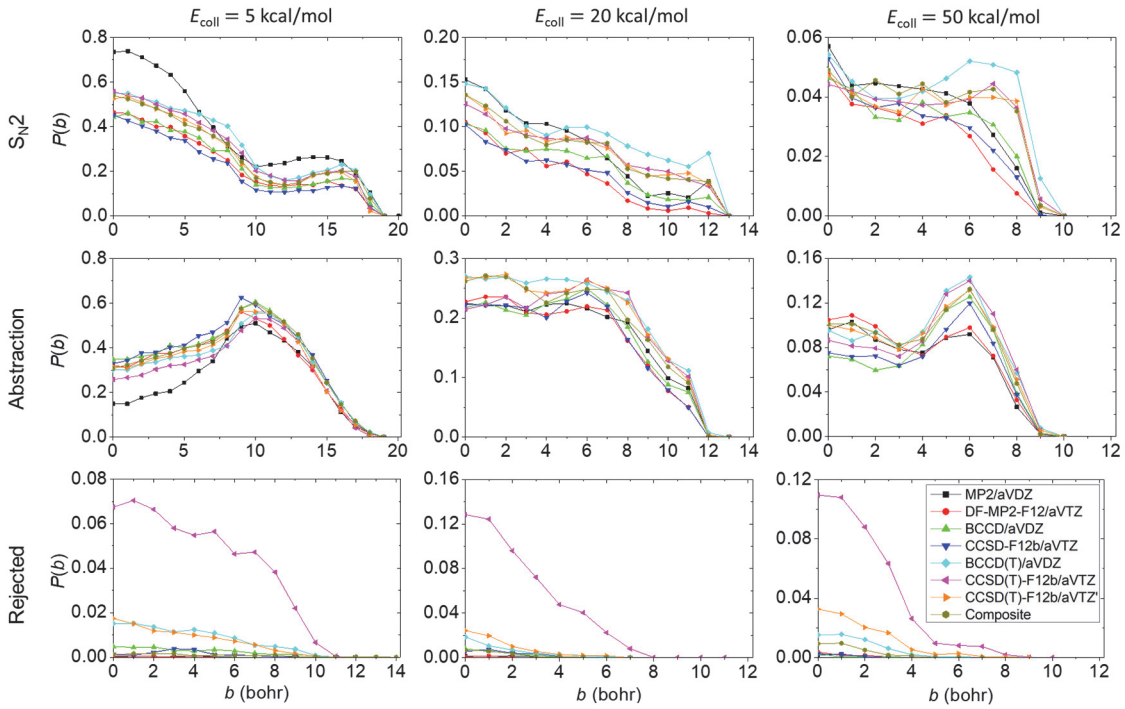

Figure S4 Opacity functions of the $OH^- + CH_3I$ S_N2, proton-abstraction and unphysical (rejected) channels at collision energies of 5, 20, and 50 kcal mol^{-1}. (Taken from ref. [7].)

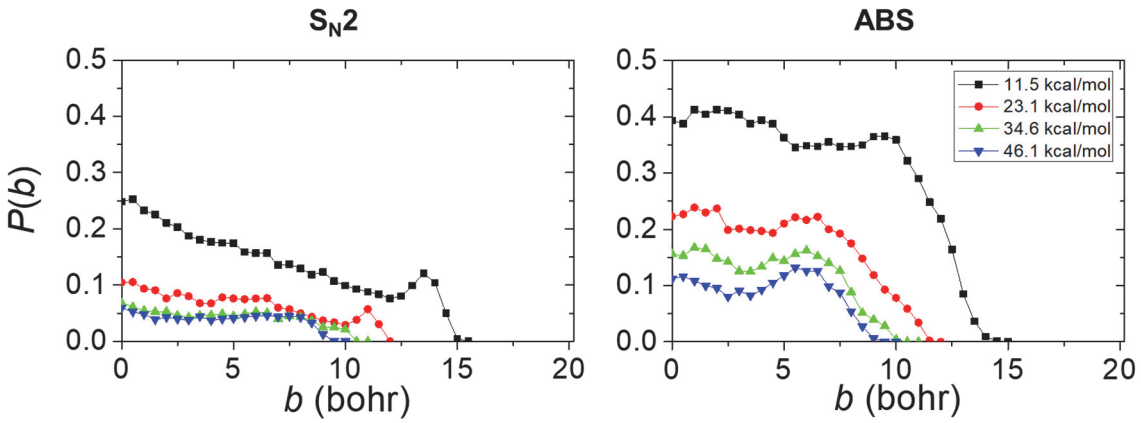

Figure S5 Opacity functions of the $OH^- + CH_3I$ S_N2 and proton-abstraction channels at collision energies of 11.5, 23.1, 34.6 and 46.1 kcal mol^{-1}. (Taken from ref. [1].)

Table S3 Integral cross sections ($bohr^2$) of the observed pathways for the $OH^- + CH_3I$ reaction at collision energies of 11.5, 23.1, 34.6 and 46.1 kcal mol^{-1}. (Taken from ref. [1].)

Reaction channels[a]	E_{coll} **(kcal mol^{-1})**			
	11.5	**23.1**	**34.6**	**46.1**
S_N2	78.97	23.33	13.10	10.36
ABS	169.84	59.31	32.81	22.20
ABS soft	100.04	40.06	23.69	16.46
ABS hard	23.94	14.81	10.45	8.02
Iodine ABS	0.04	0.03	0.02	0.02
S_N2 retention	0.07	0.02	0.02	0.07
ABS proton exch.	0.77	0.10	0.03	0.01
S_N2 proton exch.	1.19	0.14	0.02	0.01
Proton exch.	0.36	0.07	0.02	0.00
ABS dissociation[b]	0.00	0.29	1.25	2.26
$CH_2 + I^- + H_2O$	0.00	0.12	0.67	1.45
$H_2O + [I\cdots CH_2]^-$	0.00	0.08	0.31	0.52
$CH_2 + [I\cdots H_2O]^-$	0.00	0.06	0.21	0.24
$I^- + [CH_2\cdots H_2O]$	0.00	0.04	0.06	0.04

[a] $ICS_{total} = ICS_{S_N2} + ICS_{Proton\ abs.} + ICS_{Iodine\ abs.} + ICS_{Proton\ abs.\ diss.} + ICS_{Proton\ exch.}$

[b] $ICS_{Proton\ abs.\ diss.} = ICS(CH_2 + I^- + H_2O) + ICS(H_2O + [I\cdots CH_2]^-) + ICS(CH_2 + [I\cdots H_2O]^-) + ICS(I^- + [CH_2\cdots H_2O])$

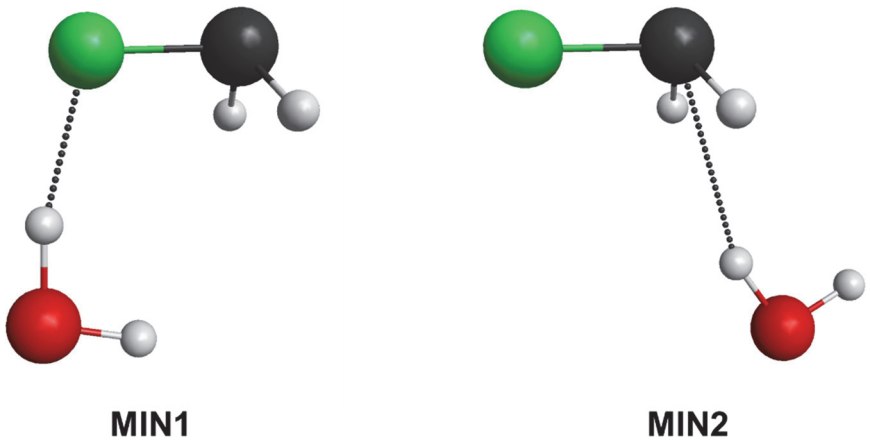

Figure S6 The structures of the two determined proton-abstraction minima of the $OH^- + CH_3F$ reaction. The benchmark relative classical energy of MIN1 is 6.15 kcal mol^{-1}, and the MP2/aug-cc-pVDZ energy of MIN2 is 13.30 kcal mol^{-1}. (Taken from ref. [4].)

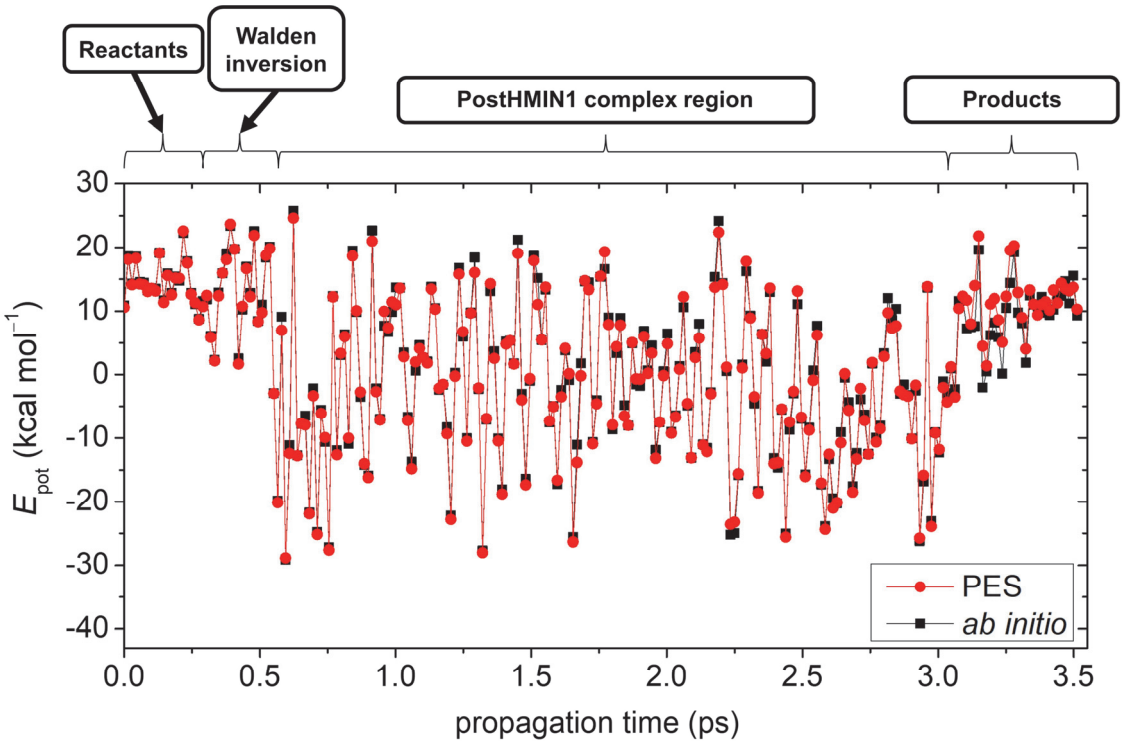

Figure S7 The comparison of the relative *ab initio* energies obtained as Eq. (4.9) with the corresponding PES values for a given QCT simulation of the $OH^- + CH_3F$ oxide ion substitution at collision energy of 10 kcal mol^{-1}. (Taken from ref. [4].)

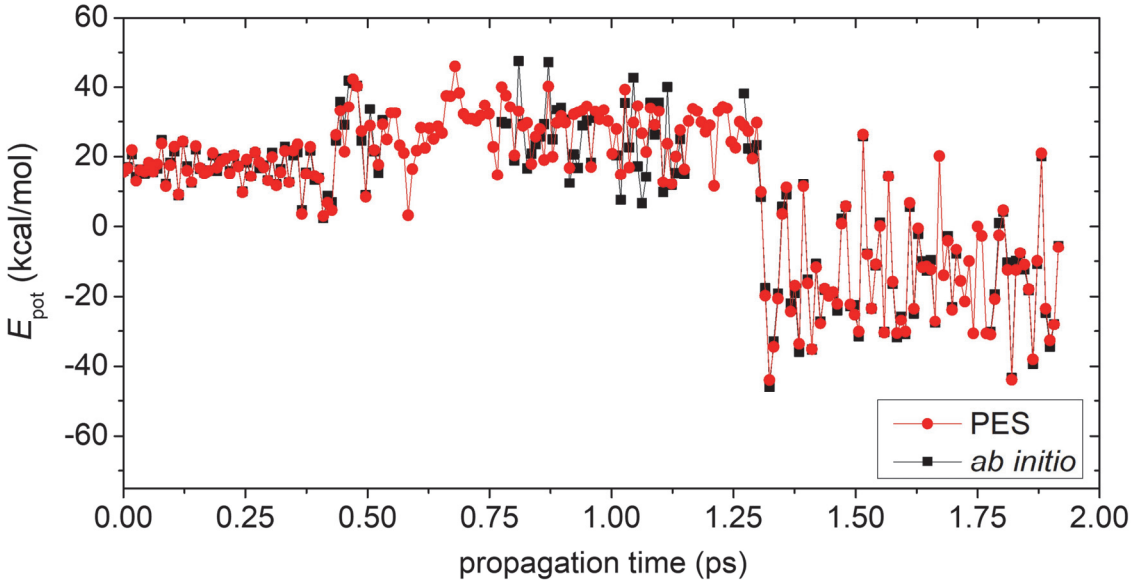

Figure S8 The comparison of the *ab initio* energies obtained as Eq. (4.9) with the corresponding PES values along a representative trajectory of the NH_2^- +CH_3I complex formation. (Taken from ref. [2].)

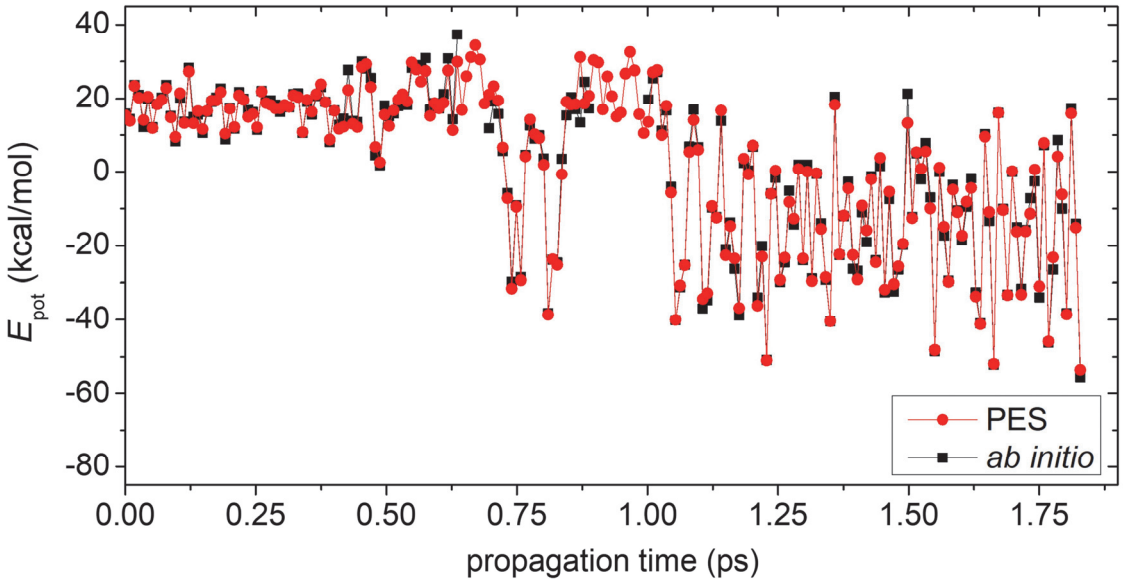

Figure S9 The comparison of the *ab initio* energies obtained as Eq. (4.9) with the corresponding PES values along a representative trajectory of the NH_2^- + CH_3I Walden inversion with complex formation. (Taken from ref. [2].)

Acknowledgements

First of all, I would like to express my deepest gratitude to my supervisor, Dr. Gábor Czakó, for his exceptional guidance, patience and mentorship throughout my doctoral work. His expertise and insight have been invaluable in shaping the direction of my research.

I acknowledge Prof. Dr. Ágota Tóth for enabling me to perform my work at the Doctoral School of Chemistry in the University of Szeged.

I am grateful to my colleagues, especially to Dr. Dóra Papp, Tibor Győri and Viktor Tajti, who have shared helpful feedback, stimulating discussions, and a supportive environment. I would like to thank Roland Wester and Tim Michaelsen from the University of Innsbruck for providing experimental data that contributed to the success of my work.

I am indebted to my wife, Alexandra Nikolett Tasiné Kovács, whose unlimited love and support have sustained me through the challenges of this process. Her enduring belief in me has been my guiding light, and I wholeheartedly appreciate her sacrifices and understanding.

Special thanks to my friends, who provided me with constant support and encouragement throughout my work.

Lastly, but certainly not least, I would like to give thanks to my parents, Dr. Gyula Tasi and Ildikó Dr. Tasiné Csúcs, and to my brothers, Tamás Sámuel Tasi and Dr. Ágost Gyula Tasi for steering me in the right path.